POLITECNICO
MILANO 1863

SCUOLA DI INGEGNERIA INDUSTRIALE
E DELL'INFORMAZIONE

Performance analysis and simulations of a laboratory X-ray Absorption Spectrometer

Tesi di Laurea Magistrale in
Engineering Physics - Ingegneria Fisica

Author: **Piero Florio**

Student ID: 928880
Advisor: Prof. Marco Moretti
Co-advisors: Prof. Giacomo Ghiringhelli
Academic Year: 2021-22

Abstract

X-ray absorption spectroscopy (XAS) is an extremely versatile experimental technique for the study of materials. Among others, it can be used to determine the oxidation state and the local environment of a given element in a material. The Next-Generation Advanced Materials (Next-GAME) project was created with the aim of bringing X-ray instruments back into common research centers that can at least partially support the research that until a few years ago was relegated only to synchrotrons. It is precisely in this context that our project takes place, aimed at the creation of a compact and user-friendly laboratory XAS spectrometer without sacrificing the energy resolution. Precisely for this purpose, an in-depth study on the geometry of monochromators was carried out, combining analytical calculations with the results obtained through ray-tracing simulations. This dual approach allowed us to highlight the effects that geometric parameters have on the resolving properties of the instrument, enabling us to maximize the ratio between performance and cost. In order to reduce the overall dimensions as much as possible without degrading the resolution, we opted for a Johansson-type, cylindrically-bent crystal. This setup drastically reduces chromatic aberrations with respect to commonly used Johann crystals. In addition, exploiting the Ge[220] reflection and subsequent harmonics, a single crystal can be used to fully cover the energy range $5 - 15$ keV of our interest, containing the K-lines of the 3d transition metals and the L-lines of the 5d transition metals.

Keywords: XAS; laboratory spectrometer; Rowland's geometry; Johann and Johansson type crystals; energy resolution; geometric contribution to the energy resolution.

Abstract in lingua italiana

La spettroscopia di assorbimento di raggi X (XAS) è una tecnica sperimentale estremamente flessibile attraverso cui è possibile effettuare analisi su molteplici materiali innovativi. Il progetto Next-Generation Advanced Materials (Next-GAME) nasce con lo scopo di riportare all'interno dei comuni centri di ricerca strumenti a raggi X che possano, almeno in parte, affiancare la ricerca che fino a pochi anni fa era relegata ai soli sincrotroni. E' proprio in questo contesto che si colloca il nostro progetto, finalizzato alla realizzazione di uno spettrometro XAS da laboratorio compatto e facile da utilizzare senza però sacrificare la risoluzione energetica dello strumento. Proprio a tal fine è stato effettuato uno studio approfondito sulla geometria dei cristalli monocromatori, affiancando ad un approccio analitico i risultati ottenuti attraverso simulazioni di ray tracing. Questo duplice approccio ha consentito di mettere in luce gli effetti che i parametri geometrici hanno sulle proprietà risolutive dello strumento, consentendoci di massimizzare il rapporto tra prestazioni e costi. Al fine di ridurre il più possibile gli ingombri senza degradare la risoluzione ci siamo indirizzati verso la scelta di un cristallo cilindrico tipo Johansson. Tale scelta, se comparata con i più comuni cristalli Johann, consente di ridurre le aberrazioni cromatiche e, in aggiunta, permette di utilizzare, sfruttando la riflessione Ge[220] e successive armoniche, un singolo cristallo per coprire interamente l'intervallo energetico $5-15$ keV di nostro interesse contenente le linee-K dei metalli di transizione 3d e le linee-L dei metalli di transizione 5d.

Parole chiave: XAS; spettrometro da laboratorio; geometria di Rowland; cristalli tipo Johann e Johansson; risoluzione energetica; contributo geometrico alla risoluzione energetica.

Contents

1 | Introduction to X-ray Absorption Spectroscopy

X-ray Absorption Spectroscopy (XAS) is a well established non destructive method for determining both the oxidation state and the local environment of a given element in the studied compound. The sensitivity of XAS to the local order makes it useful for the analysis of a huge amount of materials. Also for this reason, XAS can be considered as a technique of multidisciplinary relevance with direct applications spanning from physics, chemistry and biology to material, environmental and geological science [1]. A short and definitely not exhaustive list of important achievements in different fields is reported below [2]:

- *Physics*
  thanks to the strong sensitivity of this technique to the local environment possible applications are the study of the effects induced by dopants or defects in Semiconductor devices, the effect of small structural changes in strongly correlated electron systems and, more in general, studies related to low range interactions;
- *Chemistry and Material science*
  to monitor the oxidation state of batteries and fuel cells, to study the catalysis and in particular the relationship between structure and functionality;
- *Nanoscale science*
  to study the properties of low dimensional systems like organic and inorganic thin films or quantum-dots, obtaining information on their structure and relating their shape and size with their properties. Also covalent systems like macromolecules and polymers can be studied;
- *Environmental and Earth science*
  investigation on short-range ordered phases in minerals, studying on the same time the local variation in oxidation state and composition;
- *Biology*

investigation on metal-based therapeutic agents and metalloproteins, studying the interaction with their natural environment (for example physiological solution);

- *Cultural Heritage*
  to study the efficiency of conservation techniques by observing the changes in oxidation state of objects or pigments but also in order to date archaeological finds or restoration works.

After the advent of synchrotron radiation sources, XAS experiments strongly focused at using synchrotron facilities for the obvious advantages of synchrotron light, most important difference to conventional x-ray sources being the several orders of magnitude higher brightness. However, the limited access to synchrotron beamtime, reduces and nearly excludes a large number of potentially important scientific research to be performed. In addition, the analysis at synchrotrons of radioactive or potentially harmful to human health samples requires dedicated beamlines and specific authorizations besides high costs for the transport. Consequently, the development of alternatives is mandatory to compensate the currently lacking beamtime [3]. It is precisely in this context that laboratory XAS spectrometers are considered.

1.1. Laboratory XAS: working principles

Since their discovery, X-rays are directly related to absorption experiments. It is known, in fact, that the first tangible proof of their existence is the radiography of the hand of Röntgen's wife (Figure 1.1). The ability to take shadow pictures relies on two basic aspects of the absorption process: the first one is the strong dependence of the absorption coefficient on the atomic number Z that makes possible to distinguish different elements; the second is the possibility to properly tune the penetration depth of the radiation by changing the beam energy. The principle of a XAS experiment is extremely simple and it is based on the well known Lambert-Beer law:

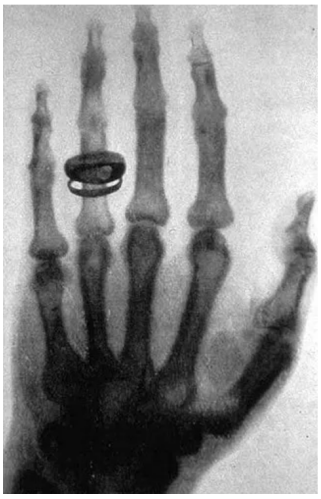

Figure 1.1: The first radiography taken by W. C. Röntgen on his wife's hand in 1896 [4].

$$I(E) = I_0(E)\, e^{-\mu(E)t} \tag{1.1}$$

a polichromatic beam $I_0(E)$ generated by an X-ray source is sent on a sample of thickness t. Given the energy dependence of the absorption coefficient $\mu(E)$, the transmitted radiation

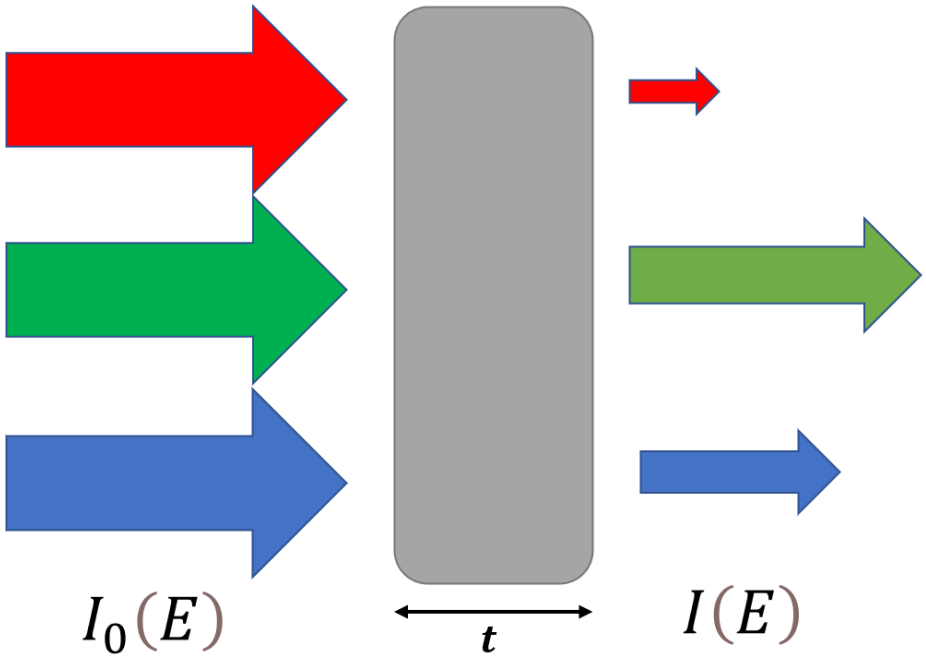

Figure 1.2: The spectral components of the incoming radiation I_0 are differently absorbed by a sample of thickness t due to the energy dependency of the absorption coefficient $\mu(E)$.

$I(E)$ will have a different spectral shape if compared with the spectrum of the source (see Figure 1.2). From this comparison a huge amount of information about the chemical-physical nature of the sample can be deduced. It is clear that, for a spectral analysis, the introduction of an element able to discriminate the different frequencies is needed. The width of the spectral region selected by this element is directly linked to the spectrometer energy resolution. The main aim of this work will be to properly design the instrument in such a way as to minimize this bandwidth. This will allow a spectral analysis with the necessary resolution. A more detailed analysis on the interpretation of XAS spectra will be given later. The following paragraphs will give a general overview of the typical use and working principles of a laboratory XAS spectrometer. In particular we will focus our attention on the *Rowland geometry setup* that offers the great advantage of making possible the choice of detectors with an extremely small surface. Thanks to the focal properties of this setup, this will not imply signal losses ensuring, at the same time, a strong decrease in noise compared to extended detectors. In this first phase we will not go into details as, in the following chapters, the vast majority of the topics here mentioned will be addressed in a more extensive way.

A laboratory XAS spectrometer based on the Rowland setup consists of three basic components:

- *Source*
  It is a polichromatic source of the X-rays. For a laboratory spectrometer Bremsstrahlung sources are used (see Chapter 2);

Figure 1.3: Incoatec microfocus X-ray source [5].

- *Bent Crystal*
  It is the element devoted to the selection of a particular frequency (see section 3.2). Thanks to its curvature, it is able to monochromatize and focus the light on the detector;

Figure 1.4: A Johansson-type bent crystal [6] .

- *Detector*
  Thanks to the detector, it is possible to measure the intensity for each selected energy in order to reconstruct the entire spectrum.

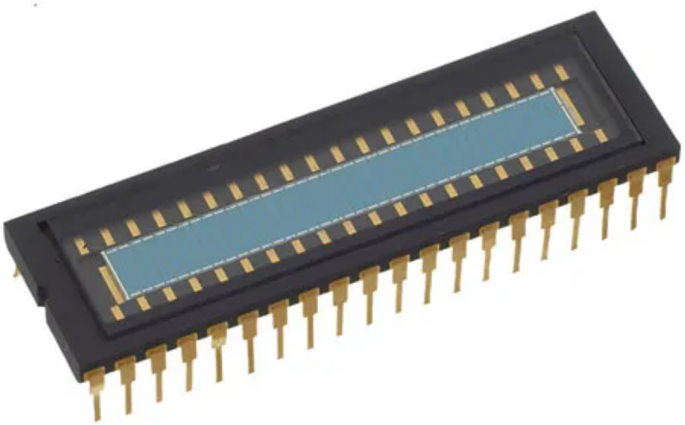

Figure 1.5: A Multi Element Photodiode Array Detector [7]

The three elements must be positioned on a circumference with diameter equal to the curvature radius R of the crystal (see section 3.2.1). The energy selected by the monochromator depends on the incidence angle of the radiation on the crystal. Consequently, in order to make an energy scan, two of the three elements must be moved: the simplest way to visualize the motion is to imagine the crystal fixed and moving the source and the detector specularly to the axis of the crystal (see Figure 1.6). However, keeping the source fixed is preferable due to its weight and dimensions. For this particular choice the motion of the crystal and detector is required as shown in Figure 1.7: it should be noted that if a reference system is fixed on the crystal in Figure 1.7, one would return to the simpler motion represented in Figure 1.6. This is to underline the total equivalence between the two motions.
After this general introduction to the working principle of the instrument, a brief parenthesis must be opened to talk about the properties that the sample must possess: the idea is to put the sample directly in front of the source and to measure, consequently, the transmitted radiation. Transmission is in fact the ideal measurement mode if we want to increase the amount of collected light [2]. Unfortunately, this choice requires high level of care for the preparation of the sample. The optimum thickness t of the sample, in fact, must be comparable with the reciprocal of the absorption coefficient in order to maximize the signal to noise ratio: for a too thin layer, in fact, the absorption is small giving rise to noisy spectra. On the other hand, for a bulk sample the transmission could be too low, increasing the error in the measure of $I(E)$.[2]

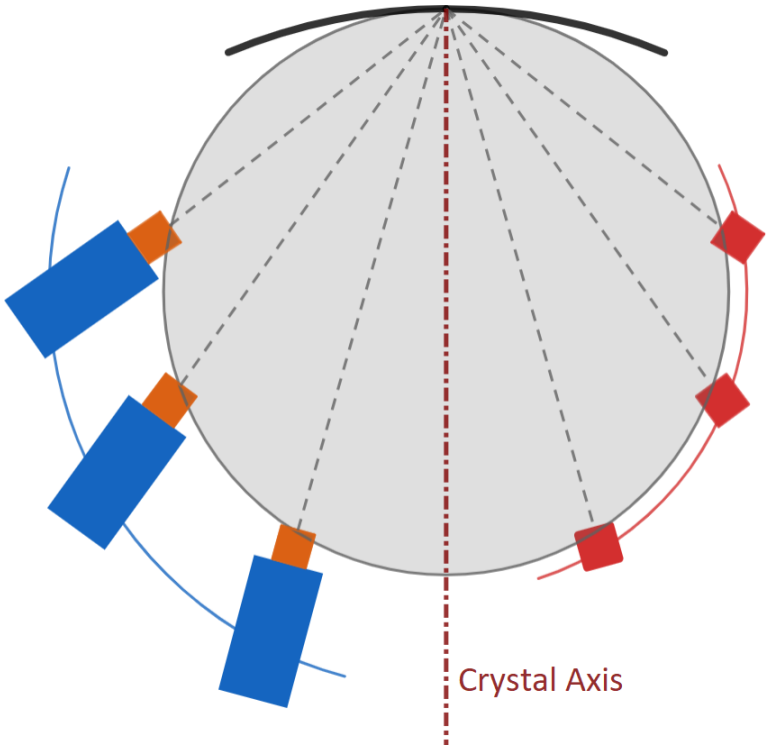

Figure 1.6: Schematic representation of a scan in energy: source (blue) and detector (red) must move specularly with respect to the axis of the crystal.

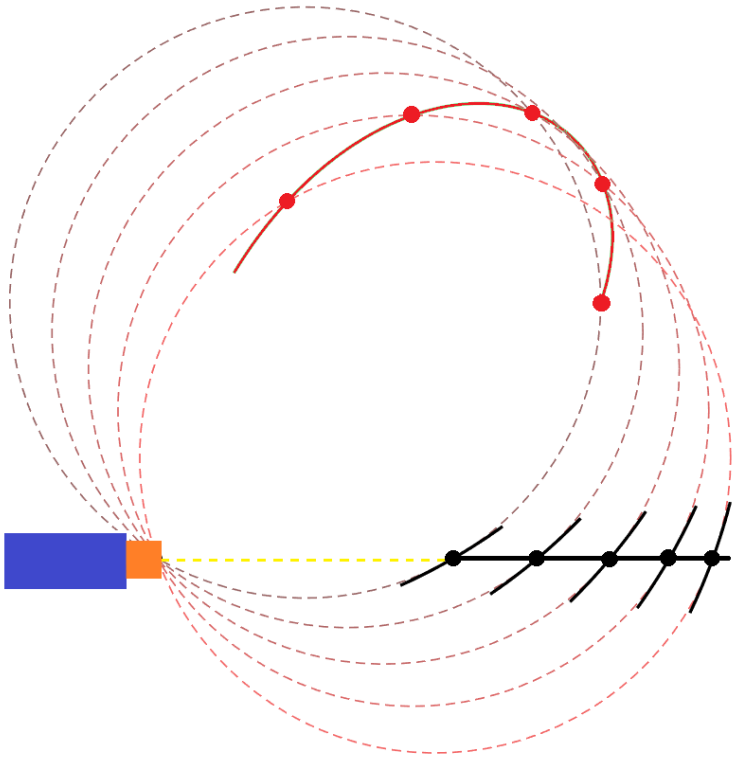

Figure 1.7: Schematic representation of a scan in energy: source (in blue) is fixed while detector (in red) and crystal (in black) moves.

The requirement of an optimum thickness could sound limiting especially if considering strongly absorbing samples. The strategy typically adopted to overcome this problem is to build pellets of transparent (for X-rays) materials into which a variable amount of sample powder is added [8]. The quantity of powder must be suitably chosen so as to have an "effective absorbent thickness" comparable to $1/\mu$. This procedure allows us to study a wide range of samples without being limited by their thickness.

1.2. Interpretation of a XAS spectrum

A typical result of a XAS experiment is reported in Figure 1.8. The absorption coefficient $\mu(E)$ can simply be experimentally obtained measuring $I_0(E)$ and $I(E)$ and inverting equation 1.1:

$$\mu(E) = \frac{1}{t} \ln \frac{I_0(E)}{I(E)}$$

As clearly shown by the graph, the *absorption coefficient* presents a discontinuous jump that is called *absorption edge*.

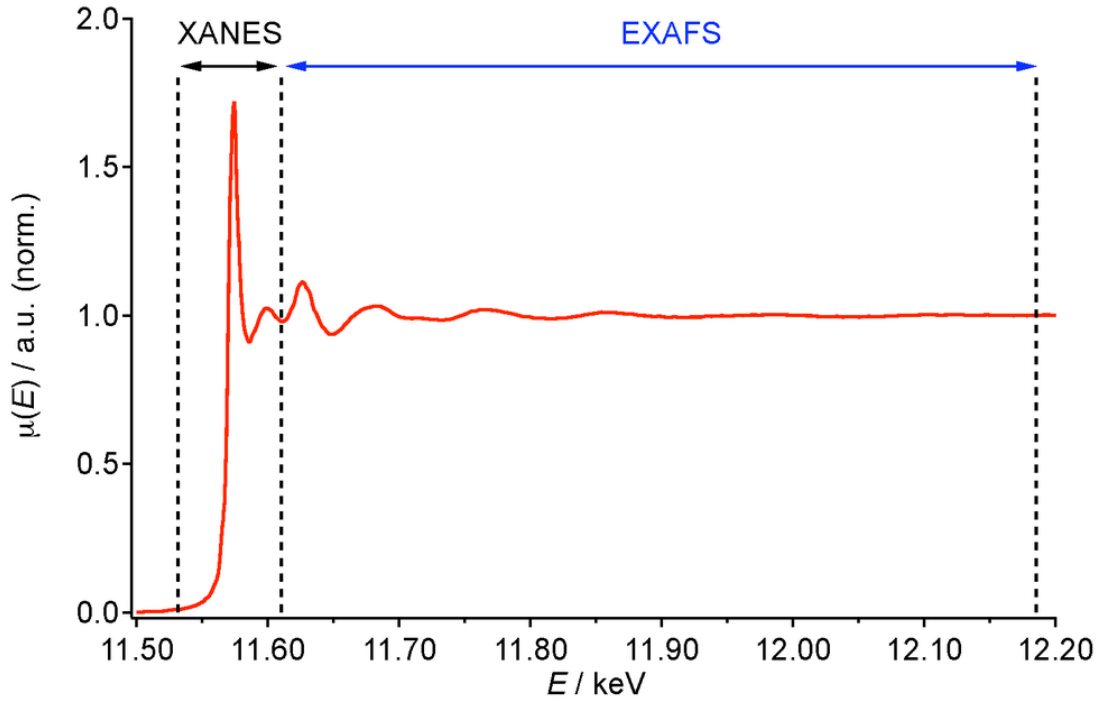

Figure 1.8: XAS spectrum example: the decaying tendency of the absorption coefficient after the edge has been removed for clarity. XANES and EXAFS regions are highlighted https://sigray.com/x-ray-absorption-spectroscopy/ .

The physical reason for its appearance is quite simple to understand: indeed, in any absorption process, the energy of the absorbed photon must necessarily be acquired by the absorbing system. Electrons are bonded in atoms with discrete energies (Figure 1.9). A photon cannot therefore be absorbed by a core electron until its energy becomes equal or greater to the binding energy of the electron. Only in this case, in fact, the electron can be promoted in the continuum making the absorption process possible. Transitions are named as reported in the left part of Figure 1.9: a capital letter is used to identify the principal quantum number n (K for $n = 1$, L for $n = 2$, ...) and a suffix number labelling the levels in each shell from the deepest to the shallowest. For example K_I - edge indicates that the origin of the photoelectron is level $(1s)^2$. The energy and the shape of the absorption profile near the edge provide insights into the electronic structure of materials. A typical XAS spectrum can be ideally split up in two regions highlighted in Figure 1.8: the first one, known as *X-ray Absorption Near-Edge Structure* (XANES), identifies an energy range centered around the absorption edge ($\simeq 100$ eV) while the *Extended X-ray Absorption Fine Structure* (EXAFS) contains features appearing after the XANES region, tipically up to $\simeq 1000$ eV beyond the edge. The XANES region usually shows an absorbtion coefficient that overshoot the step-like behaviour. This is tipically due to an high density of unfilled states just below the continuum of free electron states. The XANES region is of particular interest because the local environment can modify the DOS around the continuum causing a small shift of the absorption edge. This feature allows a fingerprint classification not only of the elements (each one with a characteristic edge) but also of several valence states of the same element. Since this chemical shift can be quite small (a couple of eV) it is necessary to have high energy resolution in this region [10].

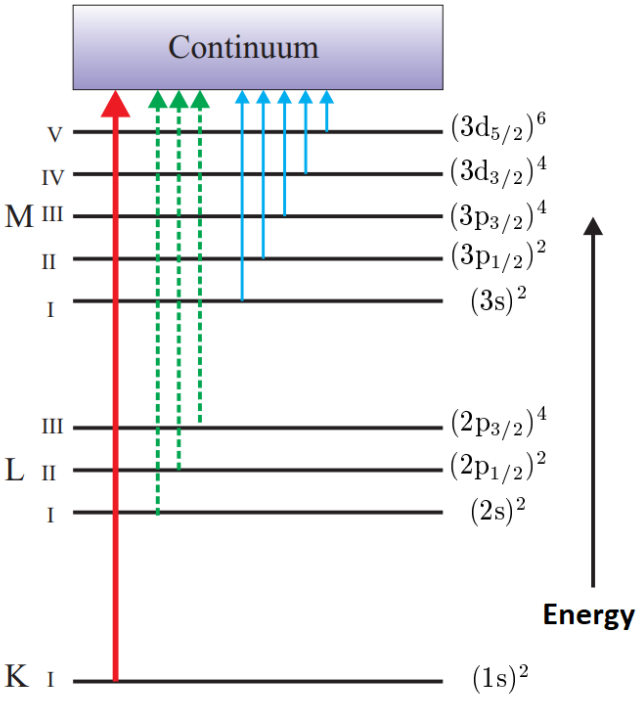

Figure 1.9: Schematic view of single-vacancy levels and corresponding nomenclature for the principal absorption edges (upwards arrows). Adapted from [9].

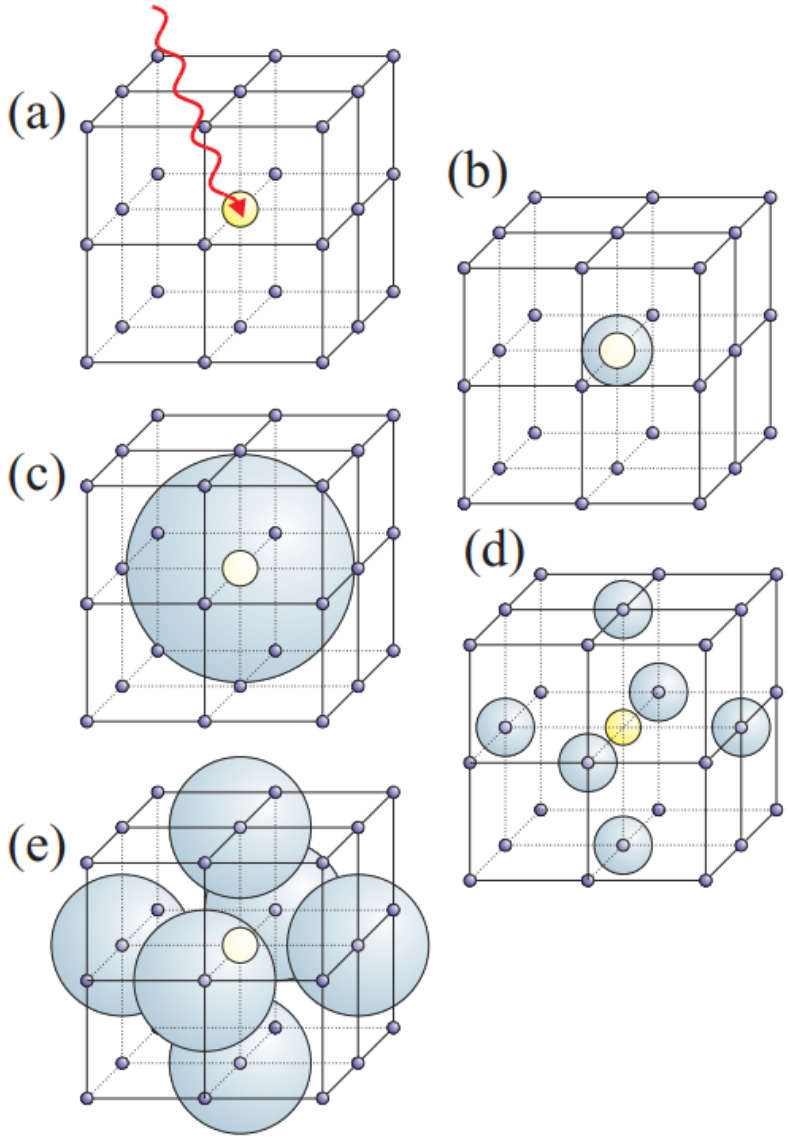

Figure 1.10: Schematic of the EXAFS process. (a) A photon with sufficiently high energy is absorbed by an atom. (b) A photoelectron is emitted by the atom and can be treated as a spherical wave. (c) The spherical wave reach the first neighbours of the emitting atom. (d) The photoelectron wavefunction is scattered by the neighbouring atoms, which then give rise to backscattered waves. (e) The interference between outgoing and back scattered wavefunctions gives rise to oscillations in the absorption coefficient $\mu(E)$. Tacken from [9].

For higher energies of the photon, the photoelectron is promoted to the continuum and propagates as a spherical wave [9]. This outgoing wave may than be back scattered by neighbouring atoms producing oscillations in the transmitted light $I(E)$ and, consequently, in the absorption coefficient $\mu(E)$. Within $10-50$ eV from the edge, the outgoing wave (the photoelectron) undergoes multiple scattering events due to its low kinetic energy. This is known as the *Near Edge X-ray Absorption Fine Structure* (NEXAFS) regime. At higher energies above the edge, due to the higher kinetic energy of the photoelectron, single scattering events dominate [9]. This is the *Extended X-ray Absorption Fine Structure* (EXAFS) region that, thanks to the negligible effect deriving from multiple scattering events, it is easier to be analyzed. In particular, it was demonstrated that the EXAFS oscillations are the Fourier transform of the radial distribution function of the atomic density [11]. The periodicity in energy of these oscillations is large, so resolution is not a strict requirement anymore, but on the other hand a high flux of photons is needed, for their amplitude is pretty weak [10]. This introductory presentation on EXAFS, while not having the intention of being exhaustive in any way, allows us to understand how useful the analysis of this region can be in the determination of the interatomic distances of the first few coordination shells around the absorber in both crystalline and amorphous materials. Very informative are XANES and EXAFS measurements at the K-edges of 3d and L-edges of 5d transition metals, which lie in the $5-15$ keV energy range.

2 | X-ray source

The production of X-rays is often connected to the acceleration of charged particles that, consequently, emit electromagnetic radiation. Although the origin of the radiation is the same, the nature of the force which generates the acceleration varies considerably according to the type of source taken into account. Synchrotron radiation takes its name from a specific type of particle accelerator. It has become a generic therm to describe radiation from charged particles traveling at relativistic speed in applied magnetic fields which force them to travel along curved paths [9]. This configuration allows to obtain a brilliance which is enormously higher than that of standard laboratory sources. Despite this, our attention will be directed to the most common X-ray tubes.

Figure 2.1: *The European Synchrotron Radiation Facility* (ESRF).

2.1. The standard X-ray tube and its spectrum

In a standard X-ray tube free electrons are produced (thermoionic emission) by a glowing filament. The electrons are then accelerated towards a metal anode that we will call from now on target. When the electron reaches proximity to an atom of the target it is typically deflected by the electronic cloud and/or by the nucleus of the atom itself emitting a continuum of radiation called *Bremsstrahlung radiation*. In this setup, the accelerating voltage (V) between the filament and the target and the current of electrons (I_A) emitted by the filament can be independently varied with the only limitation imposed by the cooling efficiency of the anode. If the continuous spectrum arises from electrons that have been decelerated and possibly completely stopped by the target, at the same time the free electron could cause an atomic electron to be removed from one of the inner shell creating a vacancy [9]. The subsequent relaxation of an electron from an outer shell produces fluorescent lines superimposed to the Bremsstrahlung continuum as shown in Figure 2.3. It is important to underline that, for our purposes, the fluorescence peaks are undesirable. These, in fact, would lead to a rapid saturation of the detector and would not allow to exploit the reflections of different harmonics. However, because of energy conservation, the maximum energy that an emitted photon can have is equivalent to the kinetic energy provided by the accelerating voltage (V) to the electron. Simply by decreasing this voltage, therefore, it is possible to cut off the fluorescence peaks.

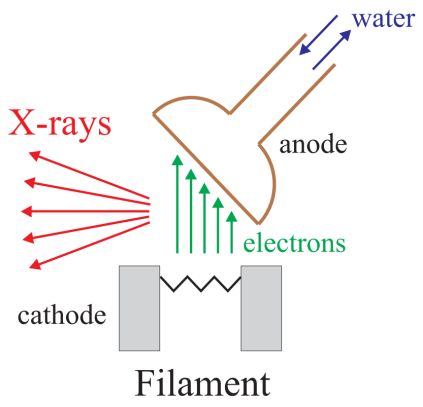

Figure 2.2: Schematic view of a standard X-ray tube [9].

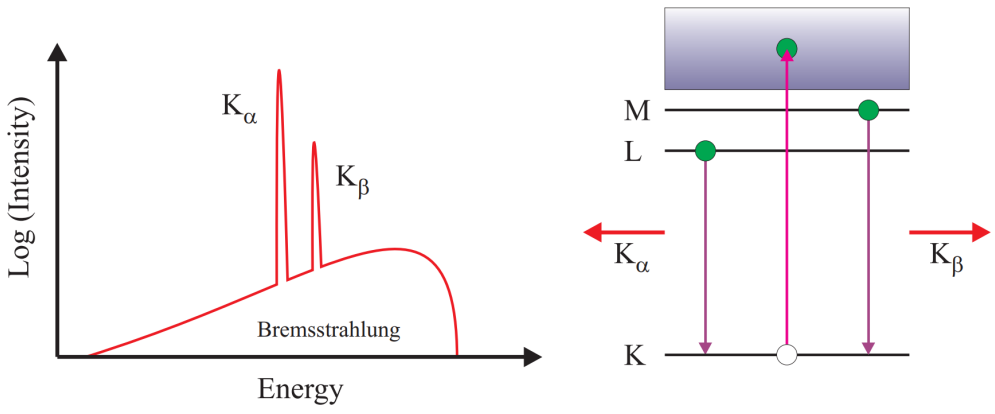

Figure 2.3: The X-ray tube spectrum composed by the Bremsstrahlung continuum with fluorescent lines superimposed [9].

2.2. Characterization of the Incoatec source.

Here are reported the results of the measurements performed on the micro-focus Incoatec $I\mu S$ 1.0 X-ray source. The main elements of the experimental setup are the source and the detector. The source is driven by a high voltage generator and is located on a fixed support. On the contrary, the detector is placed on a mobile trolley used to vary the distance from the source. The alignment between the two elements was made using a pointer fixed on the top of the source. The aim of the experiment is to study the characteristics of the emission spectra of the aforementioned source. The main quantity of interest is the photon flux evaluated over the full energy range and its voltage and current dependencies.

Source

The $I\mu S$ 1.0 Source is an air-cooled Micro-focus X-ray source provided by Incoatec[1].

Source Technical Details	
High Voltage	$\leq 50\,\mathrm{kV}$
Current	$\leq 650\,\mu\mathrm{A}$
Power	$\leq 30\,\mathrm{W}$

Table 2.1: Thecnical details of the generator of the IμS 1.0 X-ray source from vendor.

The technical details from the vendor are reported in table 2.1: as advised by the provider of the source the voltage and current of the tube were set to a maximum of 40 kV and 500 µA. The Source is available with different target materials: in our experiment the Molybdenum one is employed. The source is commonly used with a Montel optical system positioned at the exit slit. It is used to collimate and monochromatize the beam. Since, for our purposes, a non collimated and white beam is needed, we will not make use of this optics during the experiments.

[1] https://www.incoatec.de

Figure 2.4: The Incoatec Micro-focus Source IμS 1.0 with Montel optics [5].

Detector

In order to record the emission spectra we used an X-ray and Gamma-ray high resolution CdTe detector from Amptek[2] with a square active area of 3×3 mm^2. To not saturate the detector, because of the high flux, we used multiple collimators with hole diameter from 1 mm to 0.2 mm and thickness of 2 mm. All collimators are made of alloy HD17 i.e 90% W, 6% Ni, 4% Cu (Figure 2.5).

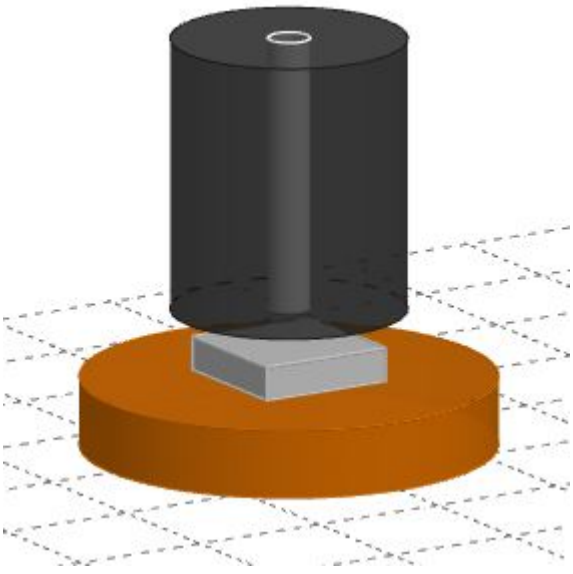

Figure 2.5: The square area of the detector with a circular collimator in front.

[2]https://www.amptek.com

The detector exploits a total of 4096 channels. In order to convert the channel scale into an energy scale, there must be at least two known peaks in the spectrum. In this specific case, the detector was calibrated using the known values of they K-α and K-β lines (17.48 keV and 19.61 keV) of the Molybdenum anode. However it is important to underline how, in order to obtain an accurate calibration, peaks that are not too close together are needed. For this reason it should be considered that far from the Mo peaks, the spectra could be not perfectly calibrated. The resulting energy width of each channel after the calibration was set to about 41 eV. The calibration is reported in equation 2.1.

$$E(\text{keV}) = 0.265152 + 0.0413351 \cdot channel \tag{2.1}$$

The ΔE in energy of each channel is given by the slope of the calibration equation:

$$\Delta E = 41.3351\text{eV} \tag{2.2}$$

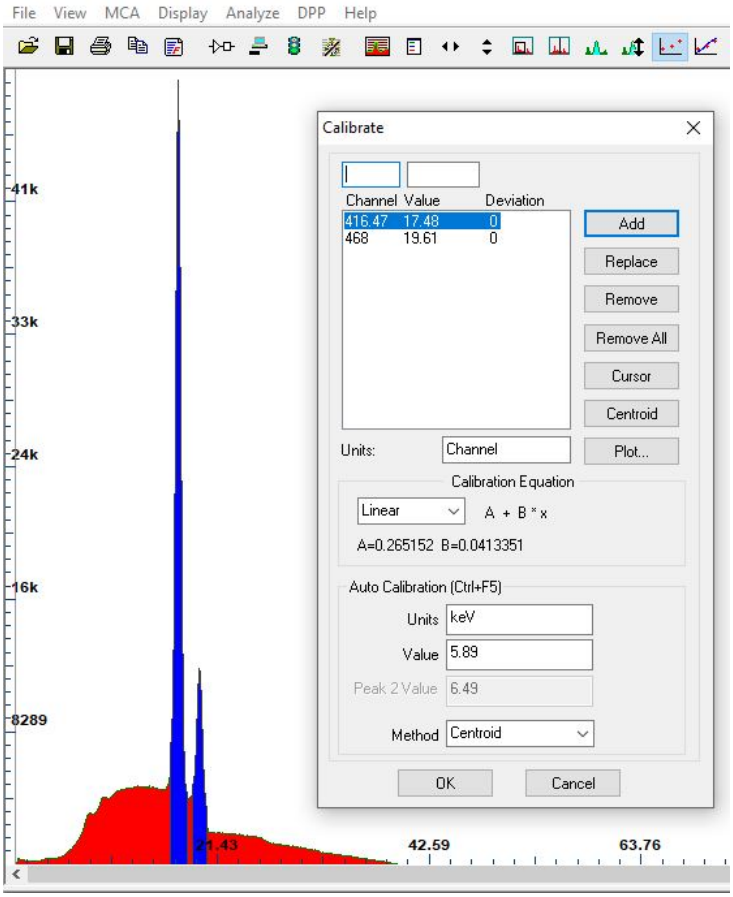

Figure 2.6: Calibration of the energy axis. The blue colored peaks are the known values of the K-α and K-β lines (17.48 keV and 19.61 keV) of the Mo anode.

2.2.1. Experiment and Data Analysis

Preliminary considerations

All the spectra are recorded with an integration time of 300 s. The detector counts the number of photons collected in each channel during the integration time. In order to compare measurements taken at different distances and with different collimators i.e. different solid angles, the data are given in *Specific Spectral Radiant Intensity*, defined as:

$$I_w(E) = \frac{counts}{T \cdot \Delta E \cdot \Omega \cdot W} \tag{2.3}$$

where T is the integration time [s], ΔE is the energy width of the channel [eV], W is the power [W] i.e. the product between the accelerating voltage [V] and the current [A] emitted by the filament and Ω is the solid angle subtended by the detector active area

$$\Omega = \frac{A}{d^2}$$

with A and d as detector area and source-to-detector distance respectively. Note that the effective area of the detector is a square of 3x3 mm when no collimators are being used; if instead the collimators are applied before the detector the effective area is circular.
Sometimes can be more convenient to consider the spectra not normalized to the power. It is useful especially if we want to observe the dependence to the current keeping the tube voltage constant or vice versa. For this reason also the *Spectral Radiant Intensity* will be considered:

$$I(E) = \frac{counts}{T \cdot \Delta E \cdot \Omega} \tag{2.4}$$

Spectra at constant power

In this section spectra collected at constant power (2 W) are analyzed (see Figure 2.8). The power of the tube is computed as:

$$P_T = V I_A \tag{2.5}$$

Where I_A is the anode current and V the voltage applied to the tube which can be set independently. As expected the Molybdenum K-α and K-β lines start being visible only for anode voltages above 20 keV. As explained before the increase of the tube voltage

results in an increase of the maximum photon energy. The Bremsstrahlung has a trend well approximated, at high energy, by the Kramer relation 2.6

$$n(E) \propto Z\frac{E_0 - E}{E} \tag{2.6}$$

where $n(E)$ is the density of emitted photons at energy E, E_0 is the energy of the scattered electrons (emitted from the filament) and Z is the atomic number of the anode. Because of energy conservation, E_0 will be the maximum detectable energy for a photon. It is important to note that, unlike what experiments show, at low energies the Kramer relation 2.6 diverges. This apparent discrepancy can be explained by remembering that photons at lower energies are more absorbed. It means that, after the generation inside the material, they have a lower probability to be externally emitted. Also for this reason, only a small amount of electron energy is converted into radiation.
Starting from Figure 2.8 and choosing three specific energies ($7 - 10 - 15$ keV averaging around these energies), it is possible to study the trend of the Specific spectral radiant intensity as a function of the accelerating voltage (and of the anode current): it is important to underline how in Figure 2.7 both the tube voltage and the current vary in order to keep the power fixed.

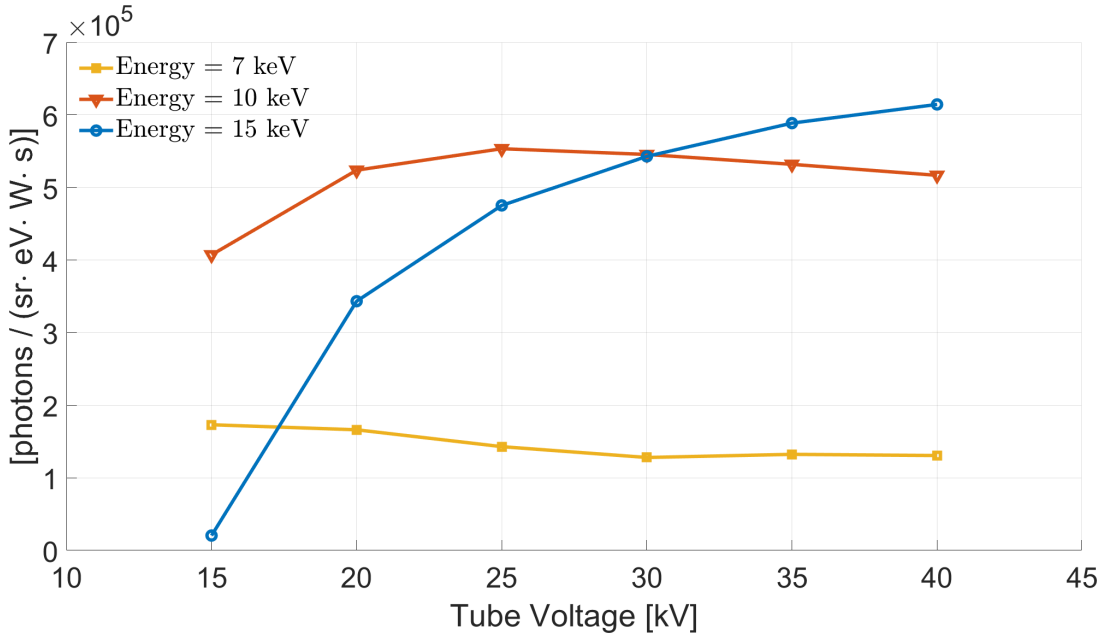

Figure 2.7: *Specific spectral radiant intensity* at three specific energies in function of both the tube voltage and the current in order to keep a constant power.

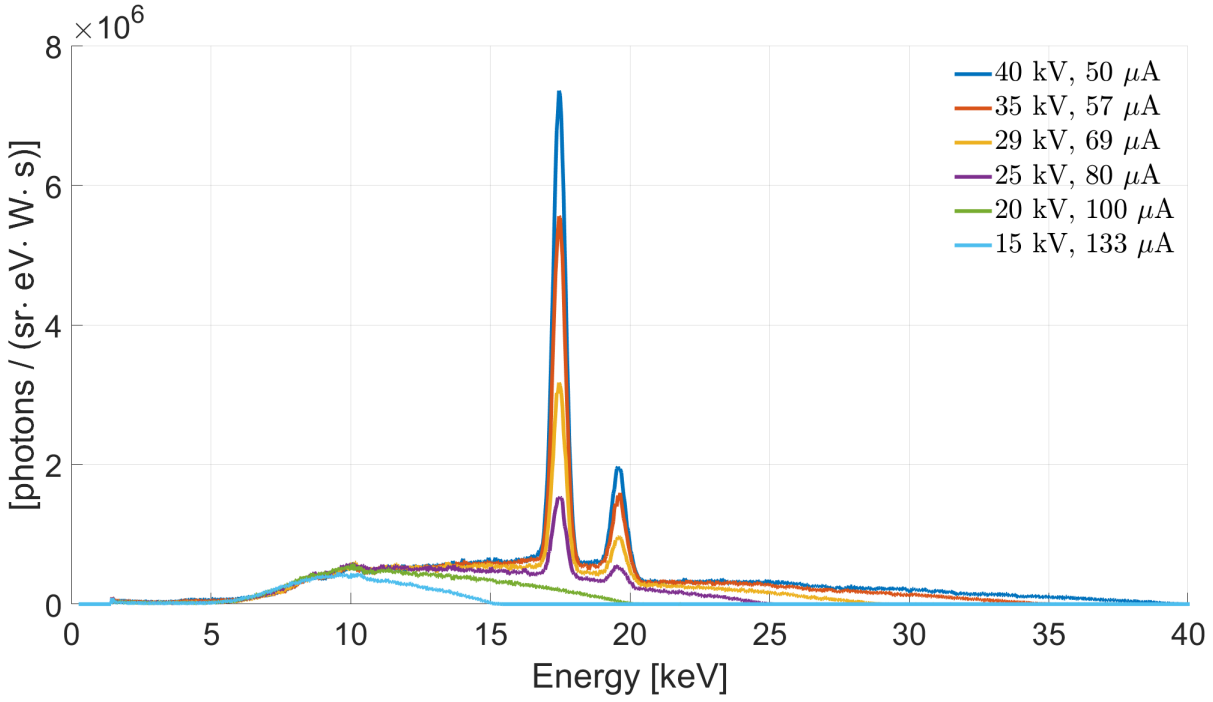

Figure 2.8: *Specific spectral radiant intensity* at constant power.

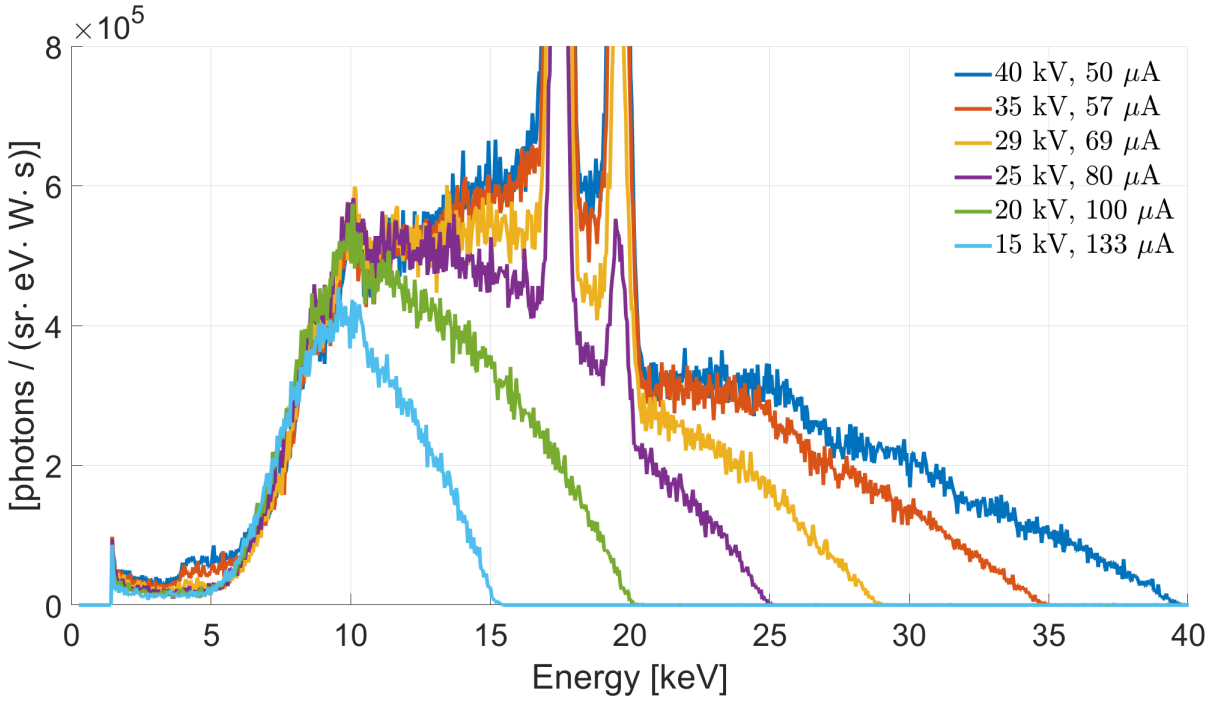

Figure 2.9: Zoom of Figure 2.8.

Spectra at constant current

The following section is devoted to the analysis of the voltage dependence of the *Spectral radiant intensity* keeping constant the current at the anode (5 µA). Starting from the original measurements (not normalized to the power) and choosing three specific energies ($7 - 10 - 15$ keV averaging around these energies), it is possible to study the trend of the *Spectral radiant intensity* as a function of the accelerating voltage V as shown in Figure 2.10

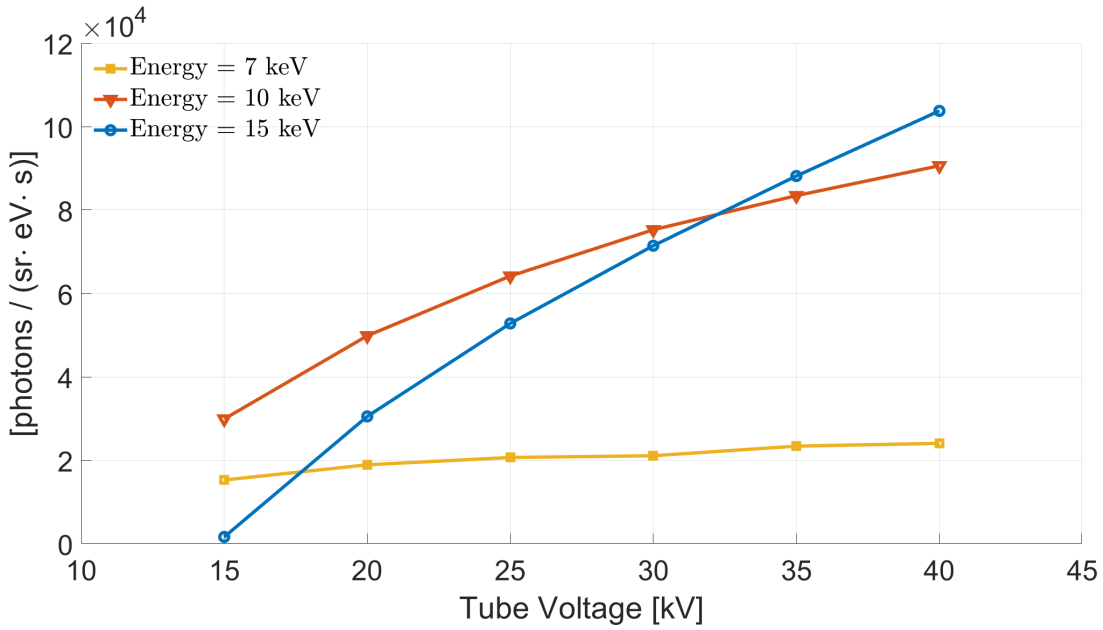

Figure 2.10: *Spectral radiant intensity* at three different energies in function of the tube voltage V.

An increasing trend is common to all the energies. Higher energies are extremely influenced by the change in voltage while a flatter trend is observed for low energies: remembering that electrons with higher energies E_0 (the energy of electrons is directly linked to the accelerating voltage) penetrate more the anode we can deduce that the absorption of the photons before escaping the anode increase with E_0. On the other hand the Kramer relation 2.6 says that

$$n(E) \propto E_0$$

Therefore it is reasonable to think that the increase of photons due to higher voltages can be compensated by the absorption especially for low energy photons i.e. for photons that are more absorbed. Figure 2.11 reports the graphs normalized to the power.

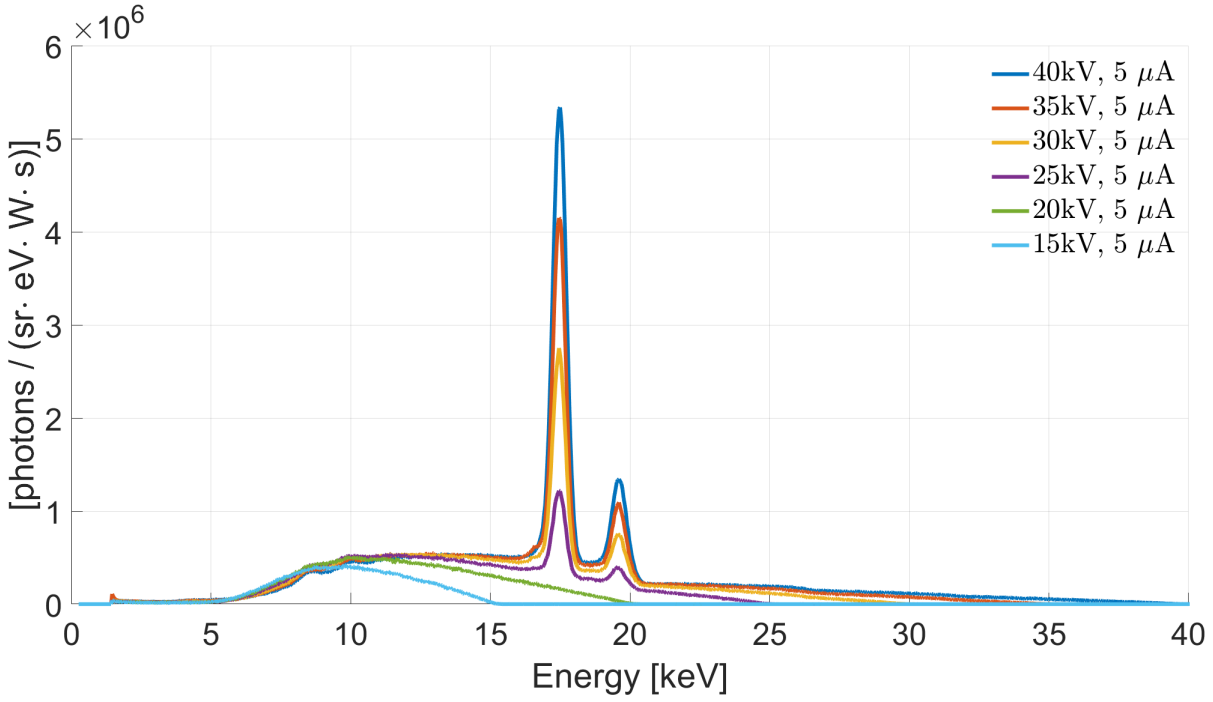

Figure 2.11: *Specific spectral radiant intensity* at constant current 5 µA.

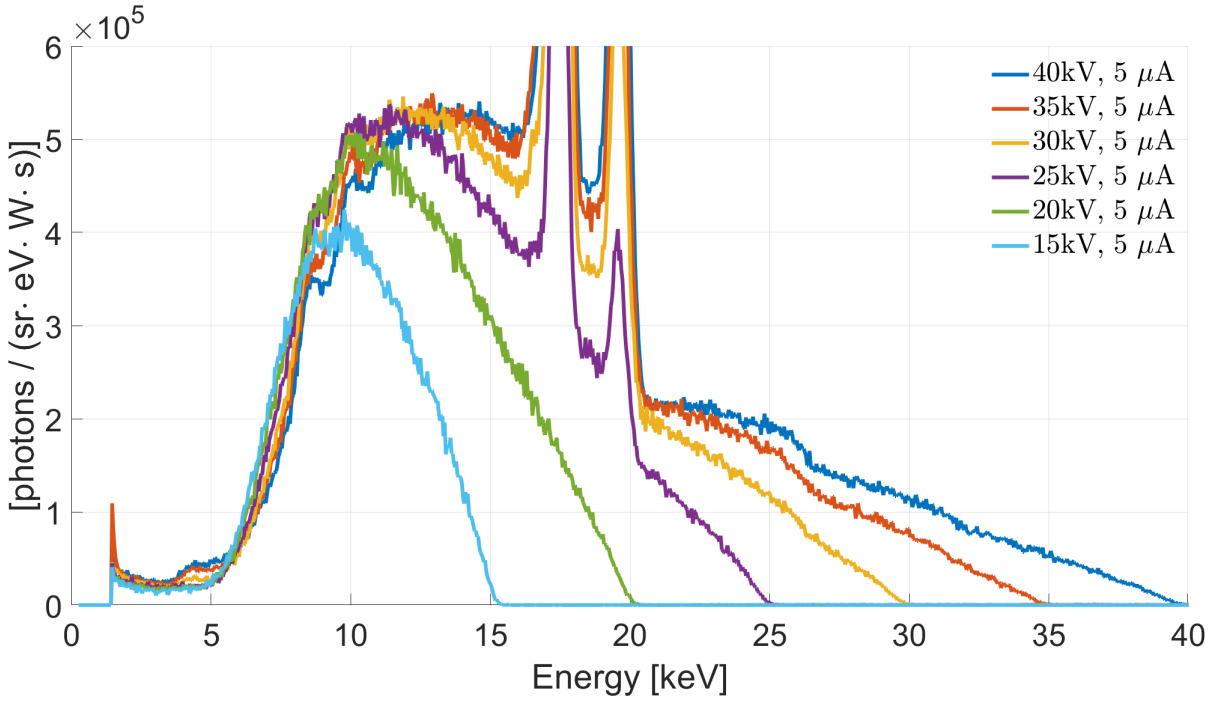

Figure 2.12: Zoom of the spectra at constant current.

Spectra at constant voltage

This section reports the dependence of the *Spectral radiant intensity* as a function of the tube current keeping constant the applied voltage at the anode (40 kV). It is reasonable to imagine how, increasing the current i.e. the number of electrons that hit the target, the *Spectral radiant intensity* should linearly increase. The linearity between the current and the brilliance is emphasized in Figure 2.13 where linear fits perfectly approximate the experimental points.

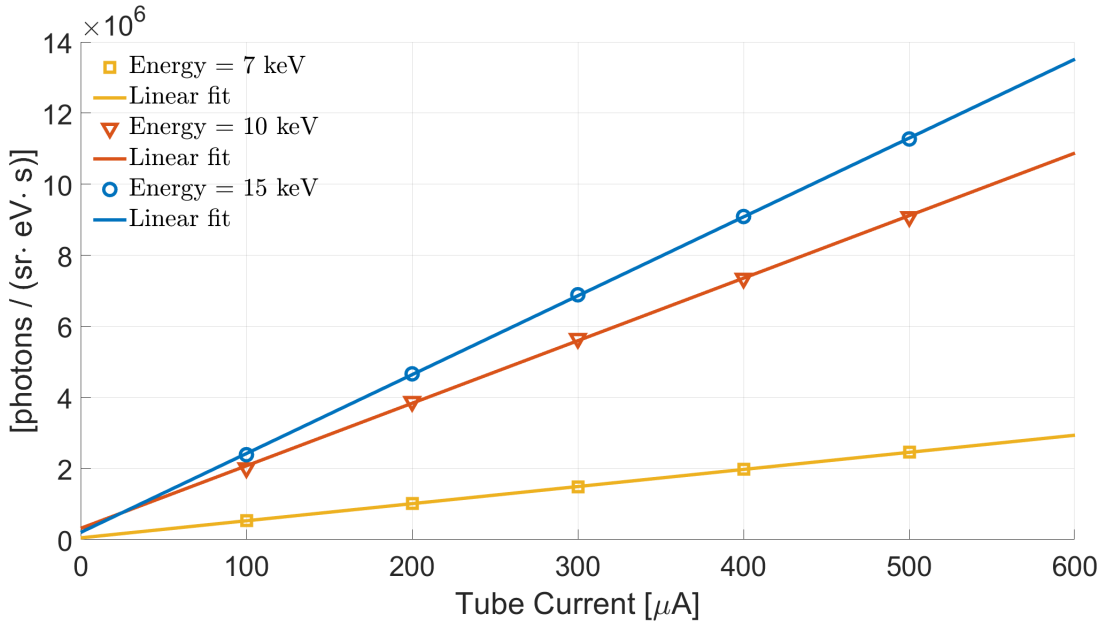

Figure 2.13: *Spectral radiant intensity* at three different energies in function of the tube current keeping the accelerating voltage 40 kV.

Increasing the current therefore increases the number of photons measured in each channel in the same way, without modifying the shape of the spectrum. Changing the voltage at the anode, on the other hand, also generates a substantial change in the shape of the spectra as seen previously. This implies that, in order to make reasonable comparisons and to check the consistency between different sets of measurements, it is good to consider simultaneously only the spectra at the same voltage. Following this approach it is clear that the *Specific spectral radiant intensity* of different measures taken at constant voltage must coincide (see Figure 2.14).

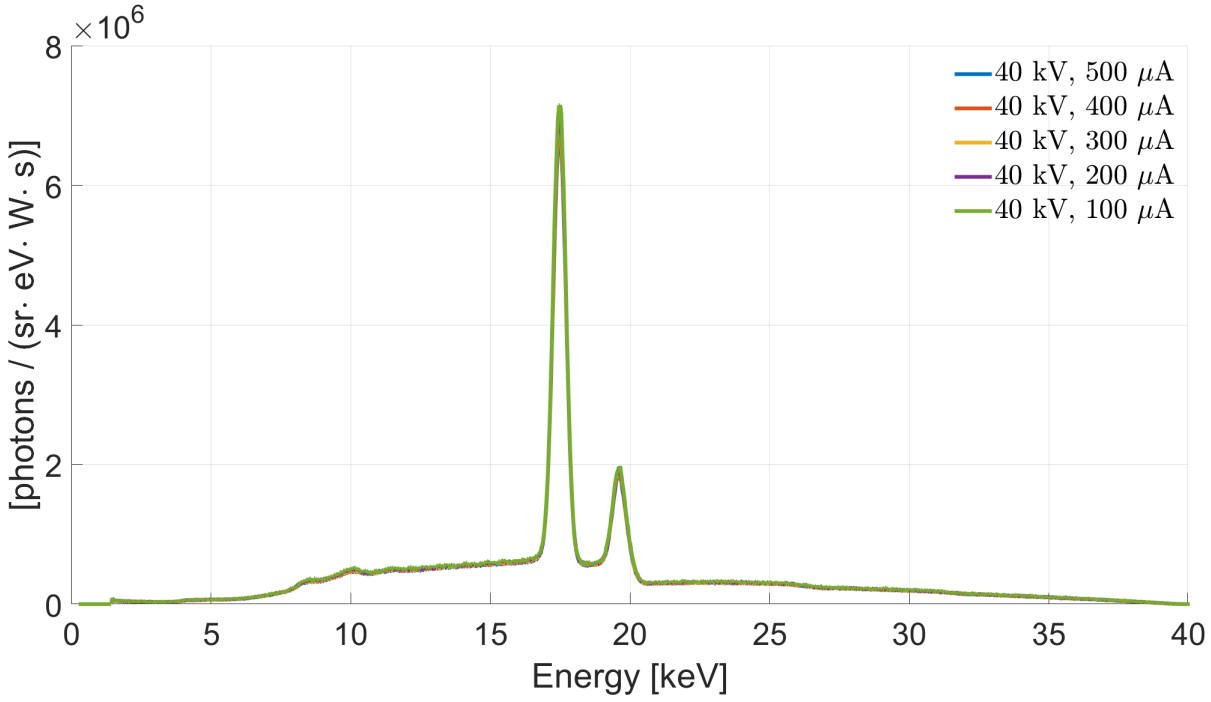

Figure 2.14: *Specific spectral radiant intensity* at constant voltage 40 kV.

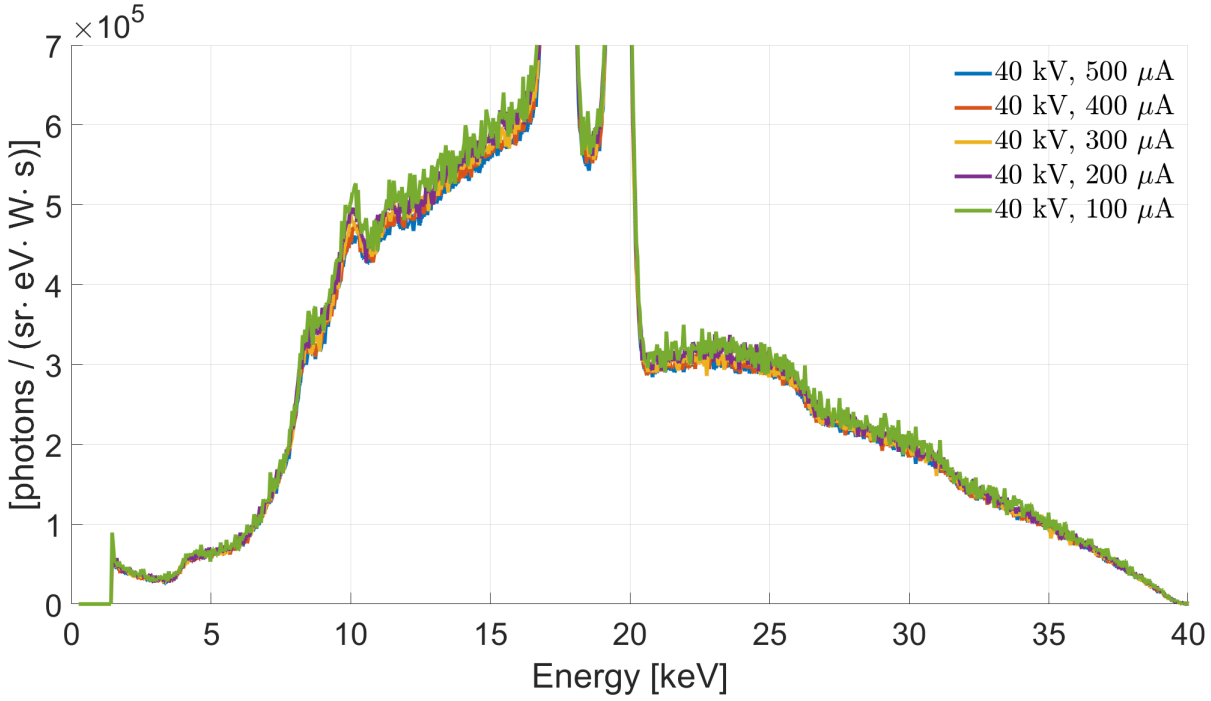

Figure 2.15: Zoom of the spectra at constant voltage.

Conclusion

The tests performed on the Incoatec $I\mu S$ 1.0 source were successful and are extremely encouraging; indeed, the performance of the source suggests that XAS measurements are feasible with laboratory spectrometer within a reasonable amount of time (see Chapter 7). In general, we aim at the maximum number of photons emitted by the source, implying that we should typically work at the largest electron current and accelerating voltage. Note that increasing the voltage beyond 20 kV, however, causes the rapid appearance of the unwanted fluorescence peaks of the anode material: if their energy is an integer multiple of the scanned energy, then they will be reflected by the crystal analyzer and unavoidably pollute the measurement (see Chapter 3). In this condition, a good choice could be to limit the tube voltage at 20 kV: considering $I_A = 650\,\mu A$ as reported in Table 2.1 we will obtain a power $P = 13\,W$ i.e. well below the threshold of 30 W set by the source manufacturer. In order to correctly estimate the *spectral radiant intensity* it will therefore be enough to consider any spectrum at $V = 20\,kV$ expressed in *specific spectral radiant intensity* and multiply it by a factor $W = 13$.

3 | Diffraction and Spectrometer geometry

The aim of this chapter is to present the basic ideas regarding diffraction in solids in order to clearly justify the geometry of the spectrometer and introduce the main contributions to the energy resolution of the instrument.

3.1. How to monochromatize a white beam

In order to make a spectral analysis is important to be able to separate different frequencies coming from a polichromatic source: for this reason the introduction of an element able to separate different frequencies is needed. The natural choice is to exploit the diffraction from a crystal. [12, 13].

3.1.1. Diffraction from a Bravais lattice

Diffraction takes place when an incoming wave interacts elastically with a periodic structure giving rise to spherical waves originating from each scattering center (the model and its founding hypotheses are better discussed in Appendix A). Let's just consider a plane wave with wavevector $\boldsymbol{k}$ impinging on two atoms.

From Figure 3.1 it is not difficult to see that in order to have constructive interference between the two outgoing spherical waves, the difference between the optical paths must be equal to an integer multiple m of the wavelenght λ:

$$\boldsymbol{d} \cdot (\boldsymbol{n'} - \boldsymbol{n}) = m\lambda \tag{3.1}$$

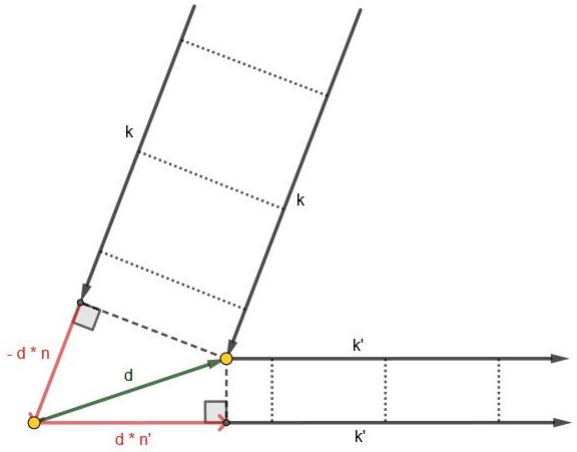

Figure 3.1: An incoming plane wave scattered by two obstacles (in yellow). The front wave is represented in dashed lines. The difference between the optical paths in red.

where:

- $\boldsymbol{d}$ = is the distance between the two scattering centres;
- $\boldsymbol{n} = \boldsymbol{k}/|\boldsymbol{k}|$ is the unitary vector parallel to the direction of the incident wave;
- $\boldsymbol{n'} = \boldsymbol{k'}/|\boldsymbol{k'}|$ is the unitary vector parallel to a possible (and up to now unknown) direction of the out-coming diffracted wave;
- λ is the wavelength of the incoming and of the diffracted wave remembering that we are considering by hypothesis only elastic scattering;

Because of the last consideration it is clear that the incoming and outgoing wavevectors can differ only by their directions. Multiplying by a factor $2\pi/\lambda$ and taking the exponential of both sides of equation 3.1, the diffraction condition can be written as:

$$\exp i(\boldsymbol{G} \cdot \boldsymbol{d}) = 1 \tag{3.2}$$

where $\boldsymbol{G} = (\boldsymbol{k'} - \boldsymbol{k})$ is by definition a vector of the reciprocal lattice. The following relation 3.3 is known as *Von Laue condition* for diffraction:

$$\boldsymbol{k'} = \boldsymbol{k} + \boldsymbol{G} \tag{3.3}$$

It is useful to give a graphical interpretation of equation 3.3 (see Figure 3.2), remembering a property common to each family of crystallographic planes:

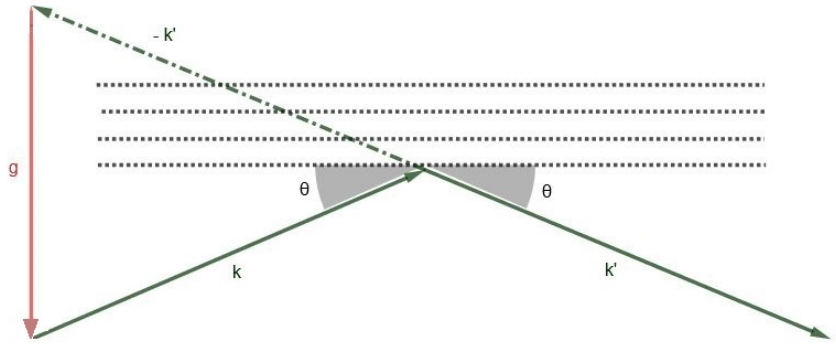

Figure 3.2: A graphical interpretation of Von Laue condition. A given family of crystallographic planes related to a particular reciprocal lattice vector $\boldsymbol{G}$ acts like a mirror for a particular wavevector $\boldsymbol{k}$.

a family of crystallographic planes can be identified by the shorter vector $\boldsymbol{G} = h\boldsymbol{a}^* + k\boldsymbol{b}^* + l\boldsymbol{c}^*$ of the reciprocal lattice that is *perpendicular* to that family of planes. The components of this vector are the *Miller Indices* that uniquely identify the crystallographic family of planes. From Figure 3.2 it is evident that

$$|\boldsymbol{G}| = 2|\boldsymbol{k}| \cdot \sin\theta = \frac{4\pi}{\lambda} \cdot \sin\theta \tag{3.4}$$

remembering the relation

$$|\boldsymbol{G}| = n\frac{2\pi}{|\boldsymbol{d}|} \tag{3.5}$$

the Bragg condition 3.6 comes directly

$$n\lambda = 2|\boldsymbol{d}| \sin\theta_B \tag{3.6}$$

where θ_B is called Bragg angle.

The behavior of a lattice can be easily compared to that of a mirror [13]. In fact a periodic structure specularly reflects the incident radiation. The substantial difference is that, assuming to hit the lattice at a certain Bragg angle with polychromatic radiation, only the wavelength that respects the Bragg's law 3.6 will be reflected. The crystal will therefore reflect monochromatic radiation[1] while the remaining part of the radiation will be transmitted and/or absorbed by the crystal itself.

[1] If the incidence angle is the same all over the surface of the crystal.

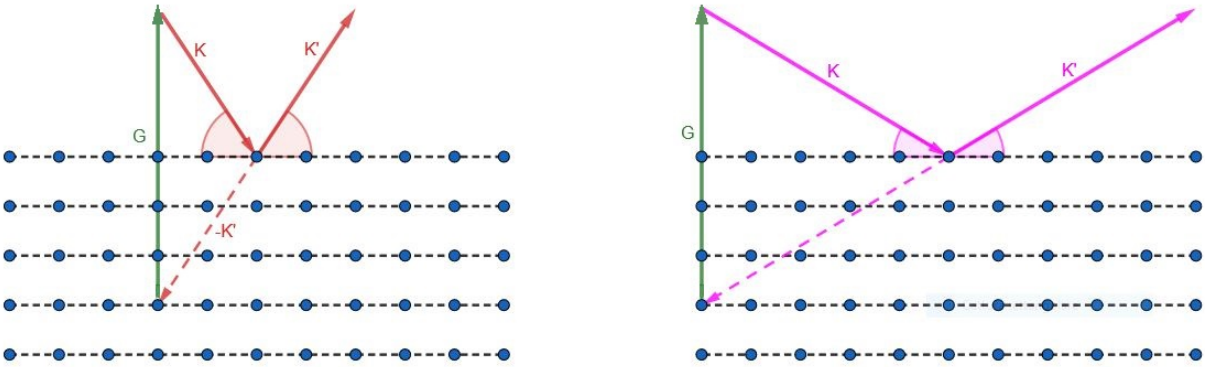

Figure 3.3: For a given family of crystallographic planes, $\boldsymbol{G}$ is fixed. Increasing the diffracted energy (length of vector $\boldsymbol{k}$) leads to a decreasing in the Bragg angle.

3.1.2. From Bravais lattices to real crystals

A real crystal is built starting from a Bravais lattice by anchoring a basis made up of one or more atoms to each point of the lattice itself (i.e, formally a crystal is given by the convolution between lattice and base). Consequently the amplitude of the radiation scattered from a crystalline material can be written in general as:

$$F^{crystal}(\boldsymbol{Q}) = \sum_{l}^{all\ atoms} f_l^0(\boldsymbol{Q}) \exp\left(i\boldsymbol{Q}\cdot\boldsymbol{r}_l\right) \tag{3.7}$$

were $f_l^0(\boldsymbol{Q})$ is the *atomic form factor* (see Appendix A) and $\boldsymbol{Q} = \boldsymbol{k'} - \boldsymbol{k}$, is the scattering wave vector that is choosen by the position of the detector. The vector position $\boldsymbol{r}_l$ can be written as $\boldsymbol{R}_n + \boldsymbol{r}_j$ were $\boldsymbol{R}_n$ is a Bravais lattice vector and $\boldsymbol{r}_j$ labels the position of an atom within the unit cell. The previous formula can so be decomposed in two summations:

$$F^{crystal}(\boldsymbol{Q}) = \sum_{n}^{all\ atoms} \exp\left(i\boldsymbol{Q}\cdot\boldsymbol{R}_n\right) \sum_{j}^{in\ cell\ atoms} f_j^0(\boldsymbol{Q}) \exp\left(i\boldsymbol{Q}\cdot\boldsymbol{r}_j\right) \tag{3.8}$$

Let's focus on the sum over n: because of Equation 3.2 we know that, in order to satisfy Von Laue condition 3.3 we need to restrict the $\boldsymbol{Q}$ domain, considering only those vectors belonging to the *reciprocal lattice*. From now on we will consider only the points of the reciprocal space corresponding to Bragg peaks and, consequently, it will be legitimate to write:

$$\boldsymbol{Q} = \boldsymbol{G} \tag{3.9}$$

Let's now consider the sum over j, better known as *unit cell structure factor*:

$$\sum_j f_j^0(\boldsymbol{G}) \exp\left(i\boldsymbol{G}\cdot\boldsymbol{r}_j\right) \tag{3.10}$$

The *unit cell structure factor* will be responsible of the amplitude modulation of the Bragg's peaks and it takes into account the phase shifts due to the reciprocal positions $\boldsymbol{r}_j$ of the atoms within the unit cell. This means that, for a crystal with a base consisting of a single atom $\boldsymbol{r}_j = 0$, Equation 3.10 reduces to the *atomic form factor*.
The square modulus of the *unit cell structure factor* will be responsible for the modulations in intensity of the Bragg peaks. It is therefore common that, some reflections consistent with Bragg's law are absent because of the destructive interference contained in the unit cell structure factor [9].
Of particular interest and simplicity is the case of *Si* and *Ge*: these crystals, in fact, are commercially available thanks to their countless applications, especially in the field of electronics. They are both characterized by a diamond-like structure. The starting point to calculate their unit cell structure factor is to choose a Bravais lattice and, consequently, the right base. The choice is not unique: often, Si and Ge are described as the convolution between an *fcc* lattice and a base made of two atoms (see Figure 3.5). However, it would be useful to refer to a simple cubic *sc* Bravais lattice: only in this case, in fact, the inter-planar distances d_{hkl} can be expressed by the following relation:

$$d_{hkl} = \frac{a}{\sqrt{h^2 + k^2 + l^2}} \tag{3.11}$$

where a is the side of simple cubic cell. Therefore the problem is easily solvable by decomposing it into two steps:

- let us start by calculating the structure factor of an *fcc* crystal described as the convolution between a *simple cubic lattice* with a base of four atoms;
- the structure factor of Si and Ge will be obtained simply by multiplying the result obtained in the previous step (that is the Bravais lattice of a diamond-like structure) by the proper *unit cell structure factor* made of two atoms.

Structure factor of an fcc crystal

As anticipated, a *face centered cubic (fcc)* crystal can be built considering a *simple cubic (sc)* lattice with a base made of four atoms identified by the following vectors $\boldsymbol{r}_j$ (see

Figure 3.4):

$$\boldsymbol{r_1} = 0 \quad , \quad \boldsymbol{r_2} = \frac{1}{2}(a_1 + a_2) \quad , \quad \boldsymbol{r_3} = \frac{1}{2}(a_2 + a_3) \quad , \quad \boldsymbol{r_4} = \frac{1}{2}(a_3 + a_1) \tag{3.12}$$

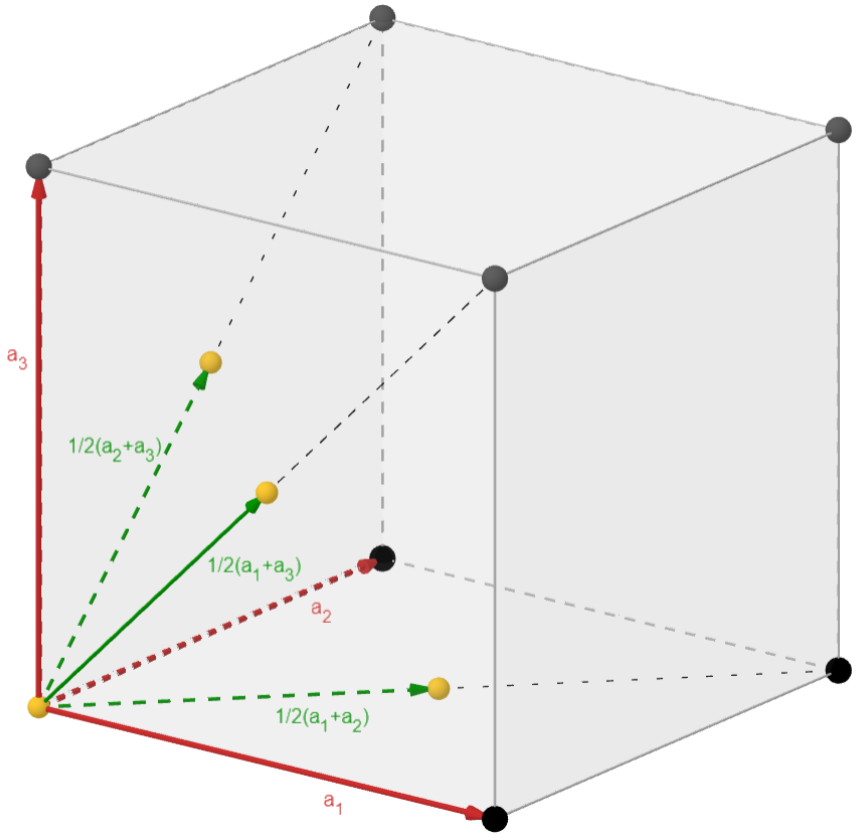

Figure 3.4: *Face centered cubic* crystal built starting from a *simple cubic* lattice (black spots) with a base of four atoms (yellow spots).

Consequently, the *unit cell structure factor* is:

$$F^{unit\ cell}(\boldsymbol{G}) = f^0(\boldsymbol{G})[1 + \exp i\pi(h+k) + \exp i\pi(k+l) + \exp i\pi(l+h)] \tag{3.13}$$

where $f^0(\boldsymbol{G})$ can be taken out of the summation on the assumption that all atoms are equal. The *fcc structure factor* is different from zero if and only if:

- h, k, l are all even or all odd.

Structure factor of a diamond like crystal

A diamond like crystal can be treated considering an *fcc* lattice with a base made of two atoms identified by the vectors $\boldsymbol{r}_j$ (see Figure 3.5):

$$\boldsymbol{r_1} = 0 \quad , \quad \boldsymbol{r_2} = \frac{1}{4}(a_1 + a_2 + a_3) \tag{3.14}$$

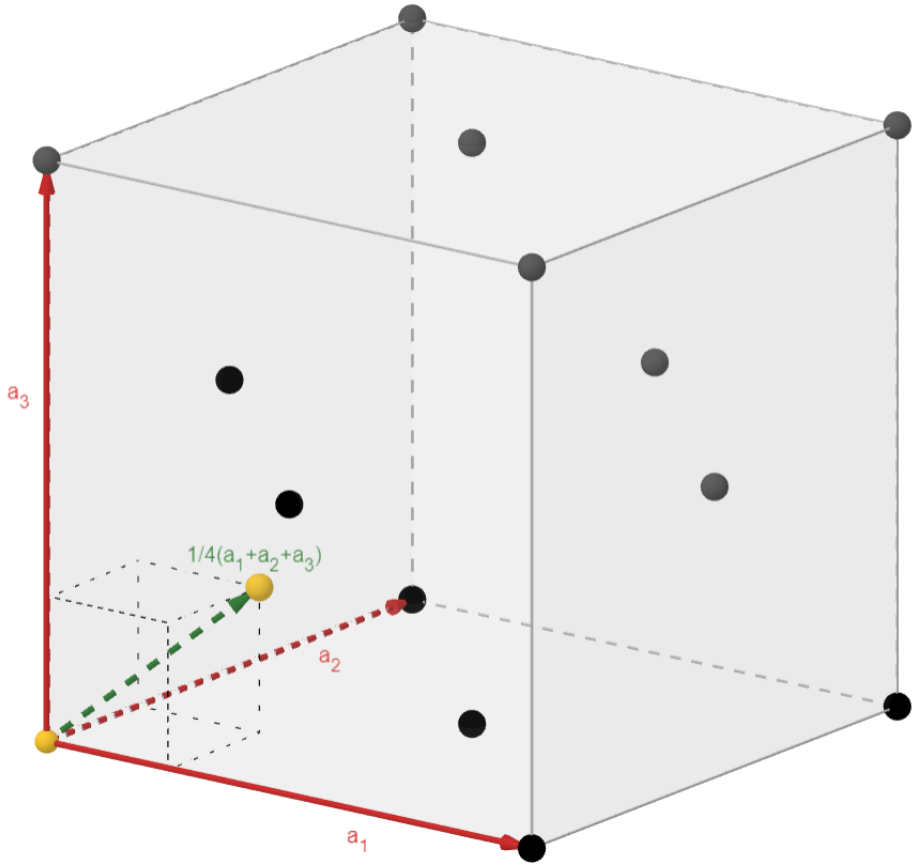

Figure 3.5: *Diamond structure* built starting from a *face centered cubic* lattice (black spots) with a base of two atoms (yellow spots).

Now the lattice is not a simple cubic as in the previous case. It means that the *lattice sum* (the sum over n in equation 3.8) gives as result the Bragg's law modulated by the factor 3.13. This term will be further multiplied by the two atoms *unit cell structure factor*:

$$F^{unit\ cell}(\boldsymbol{G}) = f^0(\boldsymbol{G})[1 + \exp i\frac{\pi}{2}(h + k + l)] \tag{3.15}$$

Equation 3.15 vanishes if $h + k + l = 2, 6, 10 \ldots$

Putting together this condition with equation 3.13 we find that, in order to have a Bragg spot one of the following conditions must be met:

- *h, k, l* are all odd,
- *h, k, l* are all even with $h + k + l = 4n$ with n $\in$ N.

The Bragg angle for some of the allowed reflections are reported (Figure 3.6 for Si and Figure 3.7 for Ge) as a function of the energy. As evident, in order to perform a wide scan in energy without ever going below $\theta_B = 30°$ it will always be necessary to exploit the reflections given by different miller indices[2]. A possible and convenient choice for a diamond-like structure is the family of planes [220] and the reflections of the first harmonics that allow to use a single crystal to cover the desired energy range (approximately from 3 keV to beyond 14 keV). The choice, in order to cover the greatest number of edges, fell on Ge[220] and subsequent harmonics (Ge[440] and Ge[660]). All the quantitative considerations as well as the simulations reported in this document will therefore refer to a *Germanium analyzer oriented along the [220] direction.*

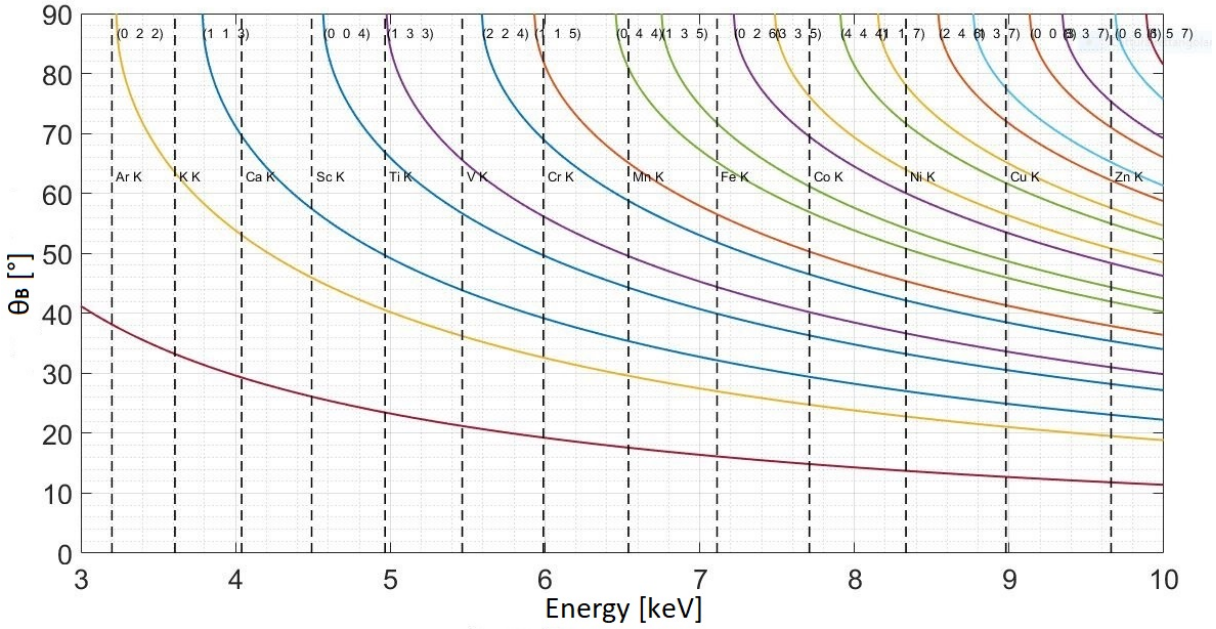

Figure 3.6: The reflected energies are plotted as a function of the corresponding Bragg angles for different families of Si crystallographic planes. Some K edges are highlighted as black vertical lines.

[2]As will be discussed, the resolution of the spectrometer drastically worsens as θ_B decreases.

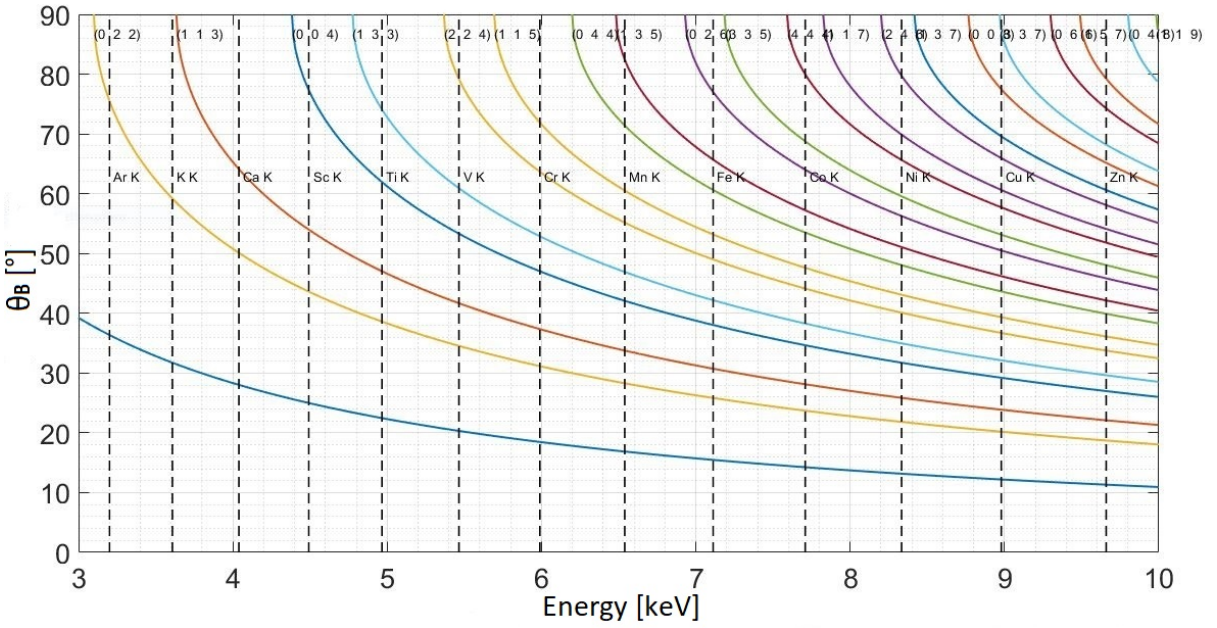

Figure 3.7: The reflected energies are plotted as a function of the corresponding Bragg angles for different families of Ge crystallographic planes. Some K edges are highlighted as black vertical lines.

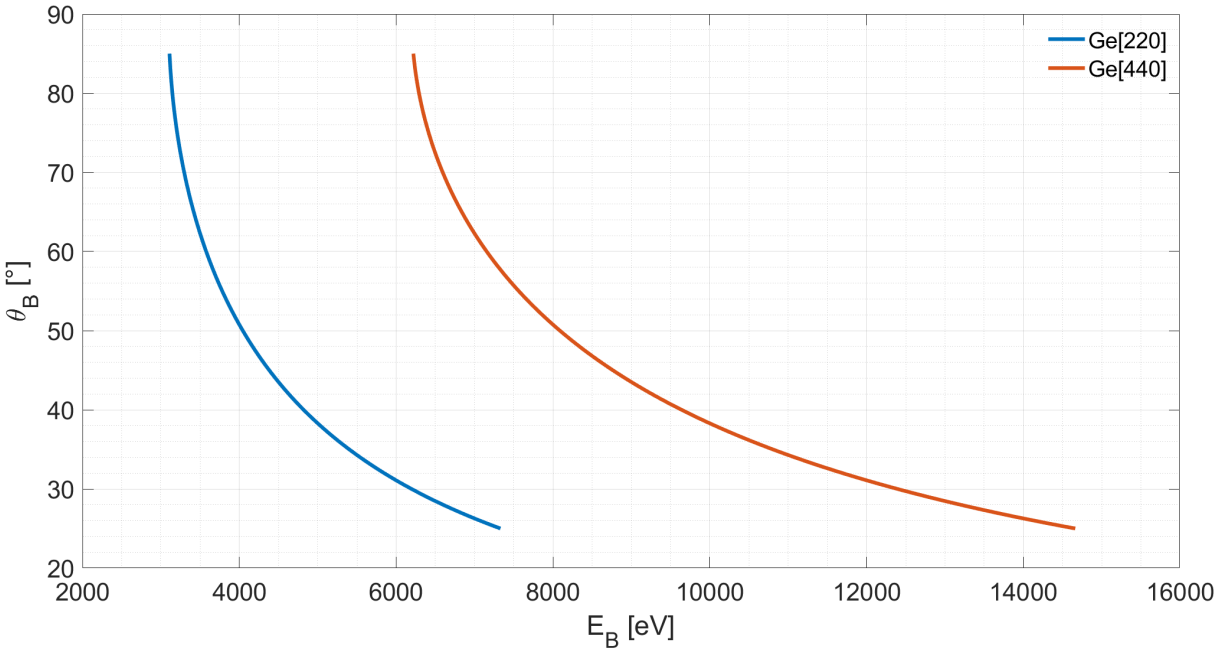

Figure 3.8: Bragg angle as a function of the corresponding reflected photon energy for Ge[220] and Ge[440].

3.2. Two-dimensional bent crystals

The introduction of bent crystals arises from the need to focus the reflected beam in a small region of space. This would allow the use of point-like detectors increasing the signal to noise ratio. It will therefore be natural, underlined the strong analogy between mirrors and crystals, to exploit the physical laws of curved mirrors to study the focusing properties of a monochromator [14]. For a 2D bent mirror with curvature radius R, the well-known formula applies [15]:

$$\frac{R}{2} = \frac{\sin\theta}{p} + \frac{\sin\theta}{q} \tag{3.16}$$

where p and q are the source — mirror and the mirror — focus distances, respectively. The previous equation is satisfied when the well known *Johann condition* holds:

$$\begin{cases} p = R \cdot \sin\theta, \\ q = R \cdot \sin\theta. \end{cases} \tag{3.17}$$

Note that the diffraction theory proposed in 3.1 is valid for flat crystals. When a perfect crystal is elastically bent, the diffracted beam is modified with respect to the flat case mainly because of two reasons:

- first, the bent geometry generates an angular distribution of the incidence angle of the rays with respect to the surface of the crystal that is clearly different from that generated by a flat crystal. This angular distribution causes changes in the diffracted spectrum that can be studied with ray tracing (see Chapter 5) and calculated analytically, as shown in the next paragraph (see Chapter 4),
- second, when the crystal is bent, the crystallographic atomic planes suffer a distortion and the local reflectivity of the crystal varies drastically on its surface. In other words, the mechanical tensions related to the bending entail a misalignment between the atomic planes causing, in general, an enlargement of the diffraction profiles [16] (see Chapter 6).

3.2.1. The Rowland circle

As shown in Figure 3.9 the Johann condition 3.17 requires to place and move source, analyzer and detector on a circular trajectory (called Rowland circle) with diameter R equal to the curvature radius of the crystal[3]. In conclusion Figure 3.10 resumes the double function of a Johann curved crystal, namely that of focusing and monochromatising a polychromatic beam. As shown higher reflected energies correspond to lower Bragg angles. Unfortunately, the use of Johann crystals in Rowland geometry is altered by aberrations which both degrade, especially at grazing incidence, the focus and the energy resolution of the instrument as explained below. Since our goal is to build a spectrometer with a single analyzer, it will be necessary to develop an appropriate design that allows to work properly even in such extreme conditions.

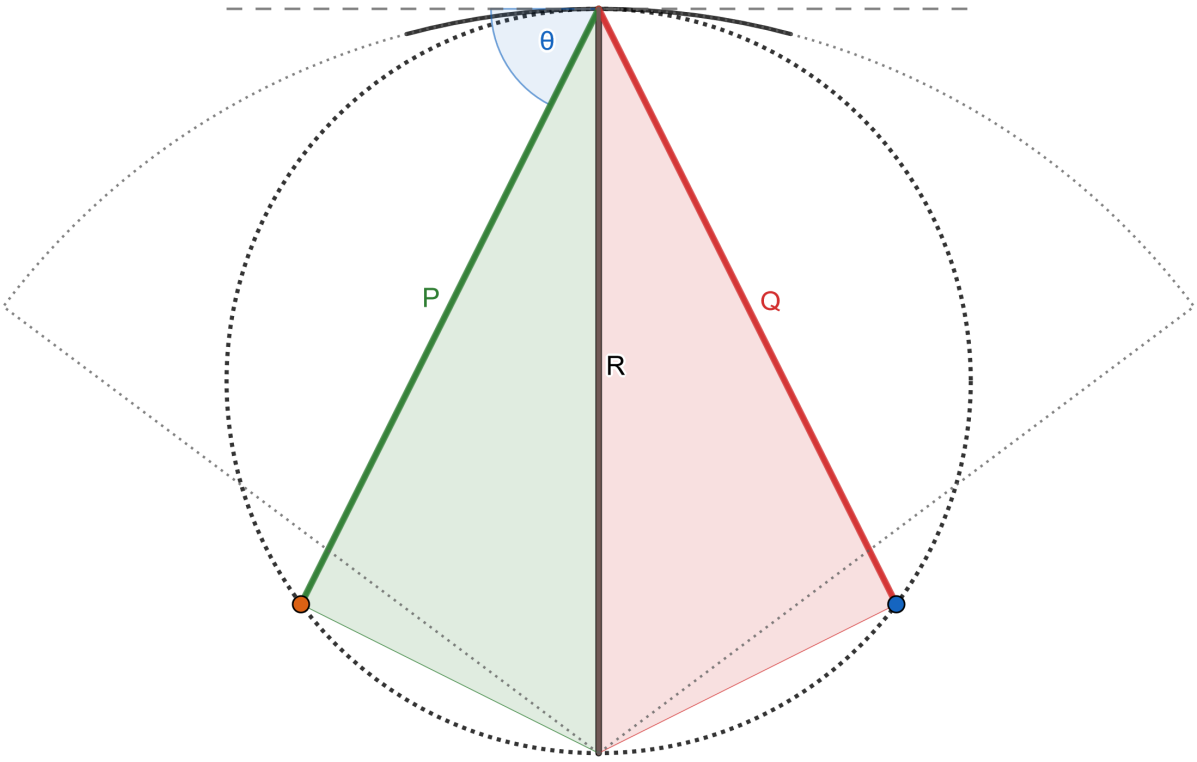

Figure 3.9: Representation of *Johann condition*: source, crystal and detector must stay on the circular trajectory (*Rowland circle*) in order to satisfy the spherical mirror law 3.16.

[3]The reader must not be confused by the fact that, in all this work, ***R*** represents the curvature radius of the crystallographic planes and, consequently, the ***Diameter*** of the Rowland circle.

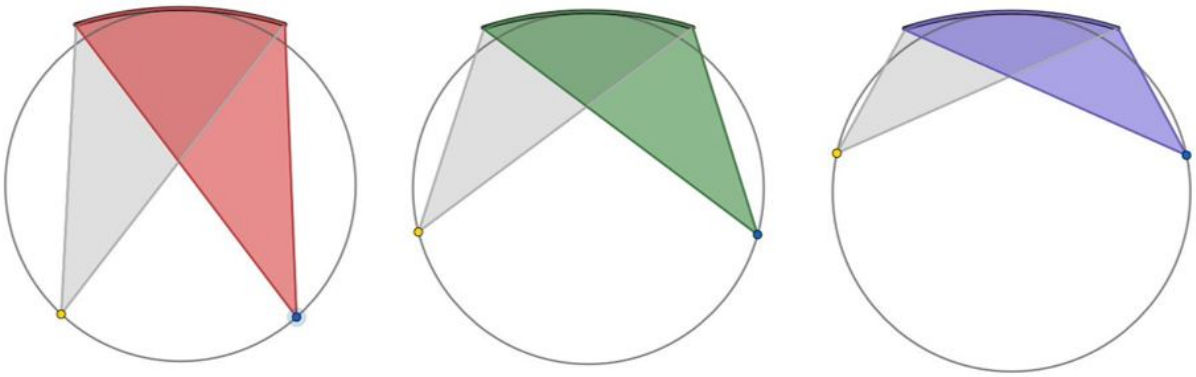

Figure 3.10: Three reflections at different Bragg angles are represented. The choice of colors underlines how, by decreasing the incidence angle, the reflected energy increases.

3.2.2. Johann-type crystals

After this brief and general introduction on the two-dimensional description of the spectrometer setup, let us discuss the energy resolution and focusing properties of a *Johann-type crystal* [17]. Understanding the geometric origin of some undesirable effects caused by this kind of crystals will allow us to naturally introduce a new type of analyzers in which, at least ideally, these effects will be suppressed.

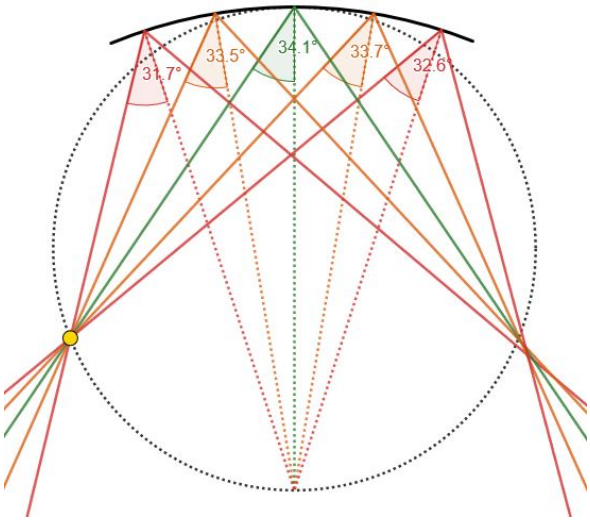

Figure 3.11: Geometric resolution worsening of a *Johann Crystal*. The Bragg angle is not exactly the same all over the surface of the crystal. This inevitably leads to a reflected line widening.

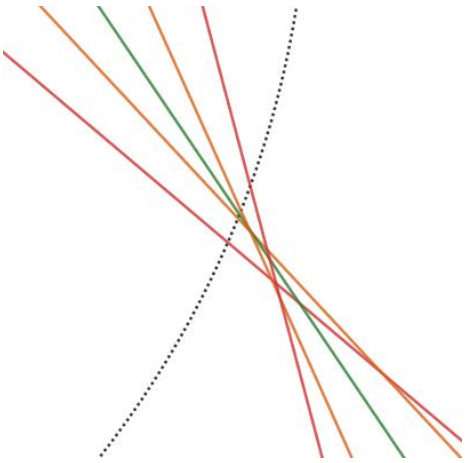

Figure 3.12: Zoom of the focus obtained with a *Johann-type crystal*. The image clearly shows a not perfect focus on the detector position.

A first observation is that, as shown in Figure 3.12, a Johann-type crystal is not able to perfectly focus all the collected light. It is mainly due to the fact that the lens equation 3.16 is valid only for rays close enough to the optical axis. For an extended mirror and in a grazing geometry, where also rays distant from the axis are collected, it is not surprising that the obtained focus is not exactly a point. In addition, as shown in Figure 3.11, also considering a point-like source, the Bragg angle is not exactly the same all over the surface of the crystal meaning that the crystal reflects slightly different energies. A first trivial way to reduce these effects is to reduce the size of the analyzer. On the other hand this operation would lead to a strong decrease in the collected light (increasing, in this way, the scanning time) making this option impracticable.

3.2.3. Johansson-type crystals

At this point it is worth asking whether it is possible to overcome the two problems that arise using Johann crystals [18]. In this regard, a brief reference to some Euclidean geometry results may be convenient. As shown in Figure 3.13, all the angles at the circumference (in green) that insist on the same arc have the same value.

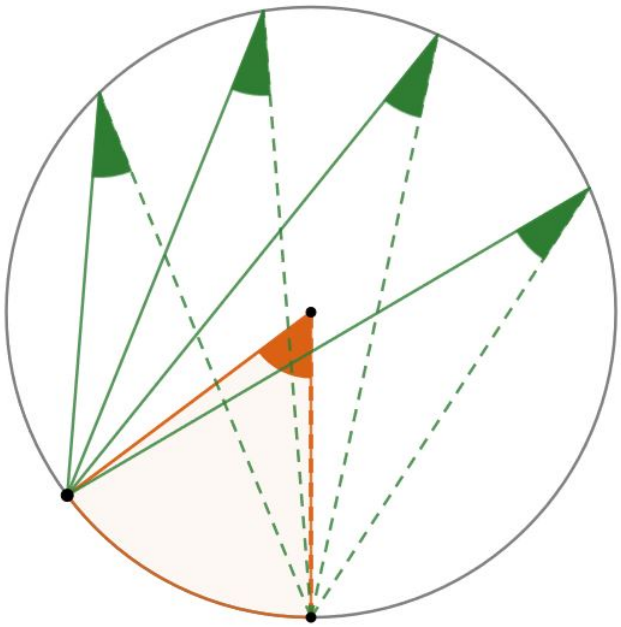

Figure 3.13: The angles to the circumference (green) that insist on the same arc are all congruent: in fact, each of these angles have in common the same angle at the center (orange).

From this simple theorem we can derive some characteristics that we would like our analyzer to possess: the reflection must necessarily occur on the Rowland circle in order to have the same angle allover the surface of the crystal (see Figure 3.13). On the same time we can not modify the curvature of the crystallographic planes because it is fixed by the Rowland diameter. From the considerations above we would like the surface of our crystal to be entirely on the Rowland circle. It is then sufficient to take a *Johann crystal* and dig properly its surface. The *Johansson crystal* thus obtained and shown in Figure 3.14 also posses the advantage of ideally focusing the collected radiation. This is because, since the angles at the circumference are equal, they must necessarily insist on the same arc that is identified by two points i.e, the position of the source and the focus.

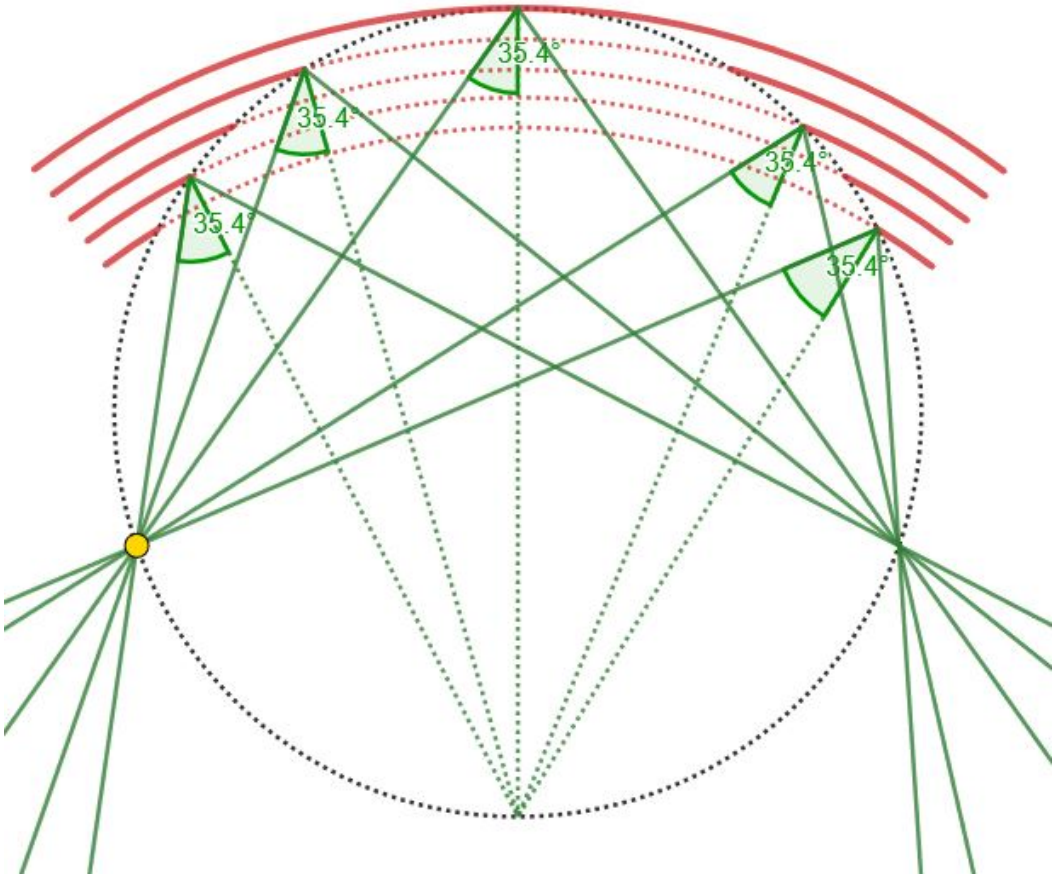

Figure 3.14: The crystallographic planes of a *Johansson crystal* are represented in red. In dashed red the portion of crystal to be removed starting from a Johann-type crystal. The graphical simulation undoubtedly shows how the incidence angles are the same over the entire surface of the crystal and how the radiation is focused exactly in one point, unlike what happens for a Johann crystal.

3.3. From 2D analysis to real space

All the considerations made in the previous paragraphs, although of fundamental importance, have a strong limitation: in fact, until now we have never taken into account the third dimension of the spectrometer. Considering the ideal case in which the source and detector are point-like, in fact, it is clear that a rotational symmetry around the axis passing through the source and detector exist (see Figure 3.15). The optimal three-dimensional geometry will therefore be obtained simply by rotating the two-dimensional set-up around this axis [19]. However, one thing is immediately evident: the position of the axis (more precisely its distance from the center of the analyzer) changes with Bragg angle. Working close to back-scattering this distance will approach the diameter of the Rowland circle while, by decreasing the Bragg angle it will decrease.

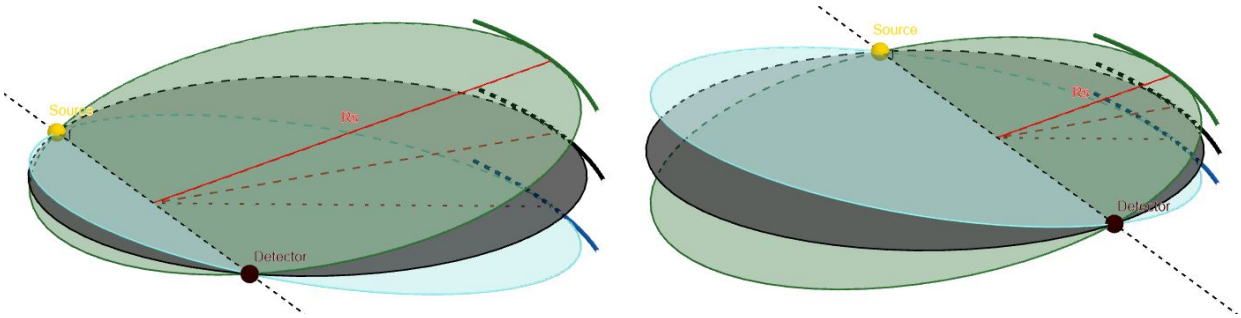

Figure 3.15: 3D geometry obtained by rotating the 2D geometry around the source-detector axis. As shown in red, the sagittal optimal curvature radius must change during the scan.

As visible in Figure 3.15, the ideal sagittal curvature radius of the analyzer is exactly this distance. The *optimal crystal* must therefore have a *toroidal shape* in which the *meridional radius is fixed* and equal to the diameter of the Rowland circle while the *sagittal radius must be dynamically changed* during the scan (Figure 3.16a). The first idea that might come to mind is to take a crystal with a fixed meridional curvature and change the sagittal one by applying a variable torque to the analyzer during the scan. This procedure, however, as well as being difficult to apply, would generate stress inside the material which, as will be explained, would lead to a rapid worsening of the resolution of the instrument. A more realistic approach is to approximate the ideal crystal analyzer by a set of independent cylindrical stripes (Figure 3.16b) of finite width whose relative positions can be dynamically adjusted as a function of Bragg angle [6]. However, the choice of cylindrical stripes necessarily worsens the energy resolution of the spectrometer as well as the focusing properties [6].

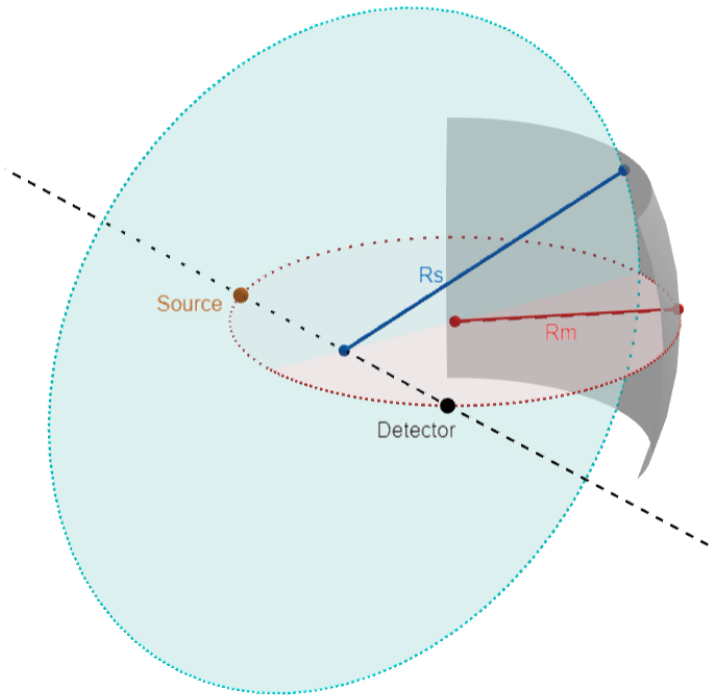

(a) Toroidal Analyzer.

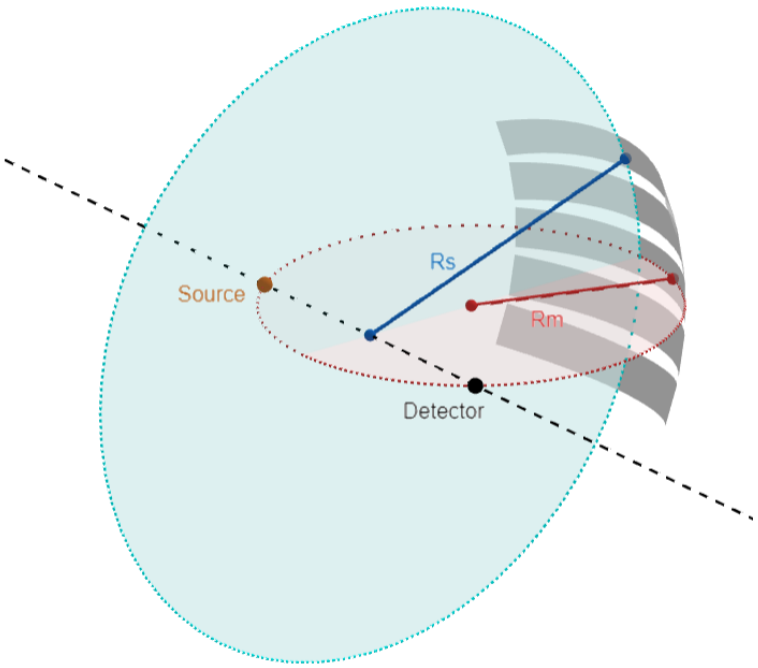

(b) Cylindrical stripes.

Figure 3.16: Comparison between a *toroidal analyzer* and *five cylindrical stripes* that map the same toroidal shape. While R_m (meridional radius) is fixed, R_s (sagittal radius) must be changed during the scan.

In a first version, the spectrometer will consist of a single Johansson-type cylindrical crystal of length $L = 10\,\text{cm}$ and width $Z = 1\,\text{cm}$. In this phase I would simply like to point out some properties related to the focus generated on the detector (see Figure 3.17): if, in the meridional plane, the crystal perfectly focus the light both thanks to its curvature and to the shape of the surface (see subsection 3.2.3), on the sagittal plane the crystal is flat being a cylinder. It means that, in the sagittal direction, the crystal does not change the divergence of the incoming beam that is fixed by the height Z of the crystal itself. Since the distance between the analyzer and the detector is exactly equal to the distance between the source and the analyzer, it is reasonable to expect a linear focus with height equal to $2Z = 2\,\text{cm}$.

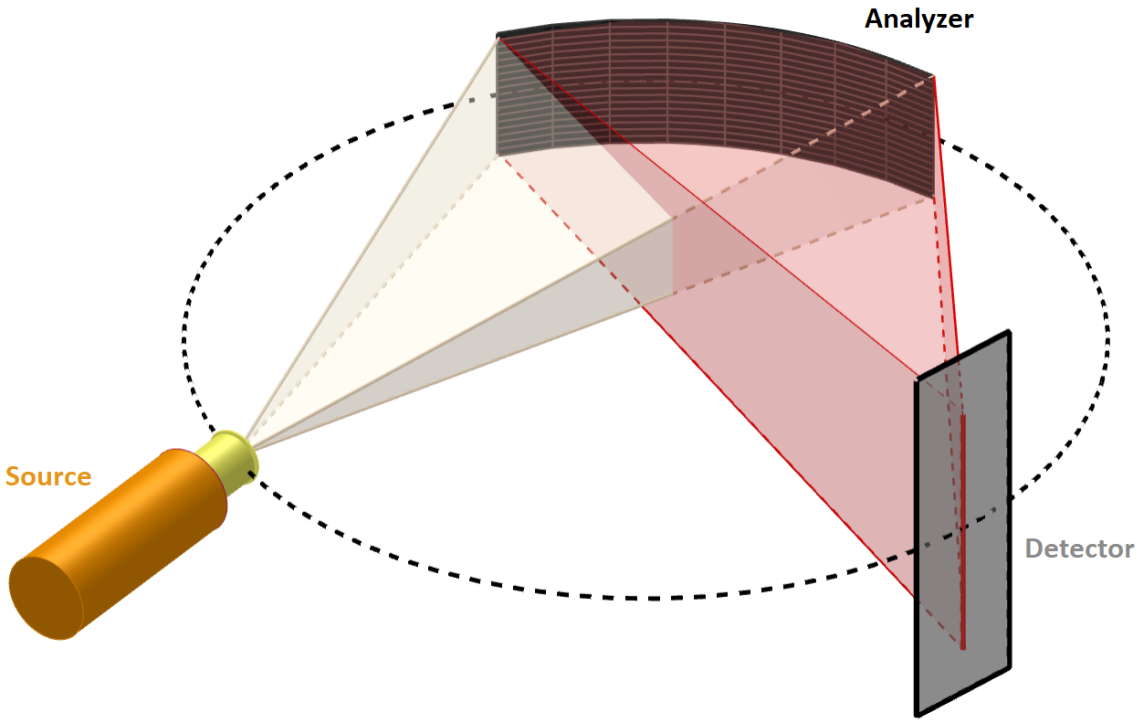

Figure 3.17: The focal properties of a Johansson-type cylindrical analyzer are shown: the focus will be two times the width Z of the analyzer.

The above reasoning is only approximately correct: by observing the projection of the spectrometer on the meridional plane, in fact, it is immediate to appreciate how only for the central ray the analyzer-detector distance is equal to the source-analyzer distance (see Figure 3.18). All the beams that hit the analyzer on the left side will make a longer path to reach the detector than the path they took to reach the analyzer, thus contributing to a further lengthening of the focus if compared to what was previously estimated.

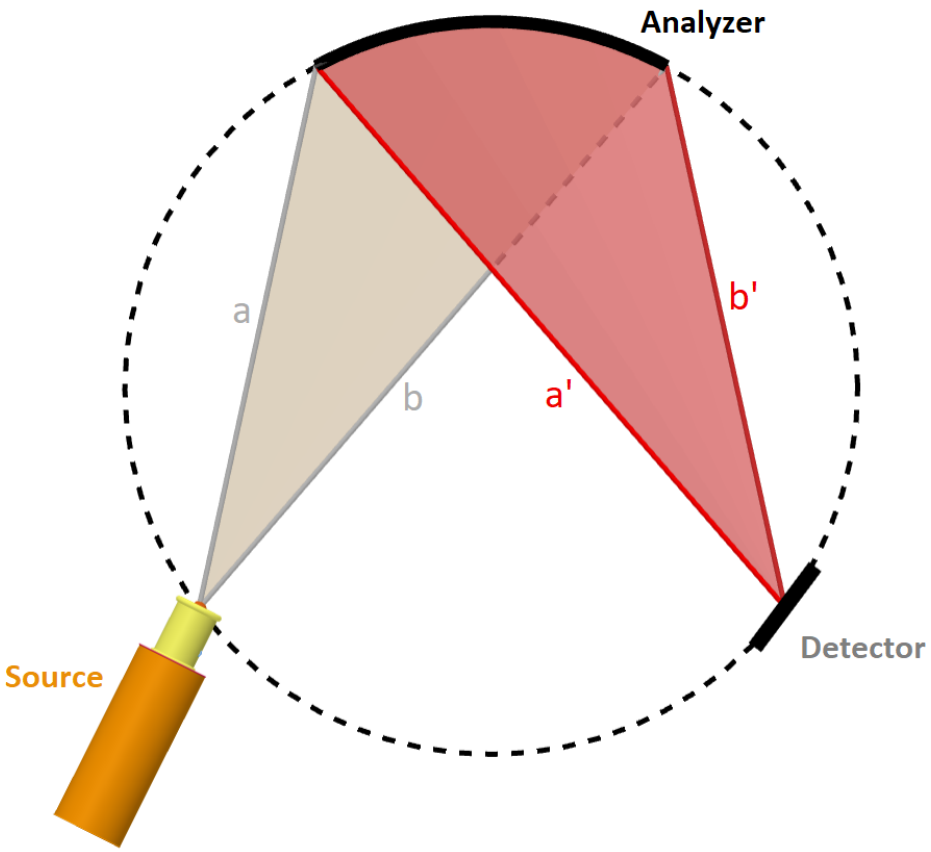

Figure 3.18: Projection of the spectrometer on the meridional plane.

A simple way to correctly calculate the focal dimension D is exploit the following proportion:

$$a : (a + a') = Z : D$$

where a is the shorter incoming path and, consequently, a' is the longer outgoing path.

In the next chapters the different contributions that lead to a worsening of the energy resolution of the instrument will be more deeply analyzed, initially addressing the problem from a theoretical point of view and then comparing the results obtained with ray tracing simulations.

4 | Geometric contribution to the energy resolution

As introduced in the previous chapter, in order to have a perfect monochromatic beam it would be necessarily for all the incoming rays to intercept the analyser at the same angle. This is not possible mainly for two reasons:

1. Cylindrical stripes will necessarily introduce a spread of the reflected angles around the nominal Bragg angle. This contribution is called *Analyzer contribution to the energy resolution.*

2. Due to the non-negligible size of the source, there will be rays that starting from different positions will intercept the analyzer with slightly different angles. This further contribution is called *Source contribution to the energy resolution.*

The purpose of this chapter will be to derive analytical formulas to quantify the deviation from the nominal Bragg angle due to the two contributions taken both separately and simultaneously. The formulas thus obtained will be discussed trying to emphasize their physical meaning, comparing them with the results reported in some papers. In the following, we will assume that the crystal curvature does not produce any intrinsic distortion in the diffraction profile. In other words, the crystal behaves locally (i.e, in each small area of its surface) as a flat crystal. The worsening of the resolution due to the bending will be treated separately in Chapter 6.

4.1. Analyzer contribution to the resolution

In order to take into account only the analyzer contribution to the energy resolution, in the following discussion we will assume a point-like source. As pointed out in 3.2.3, Johansson crystals are not affected by aberrations. It is fundamental to underline that this statement is perfectly true only if we are dealing with a toroidal crystal (see Figure 3.16a). This is not the case of a cylindrical crystal because there will be a distribution of incidence angles across the width of the crystal i.e. out of the Rowland plane (Figure

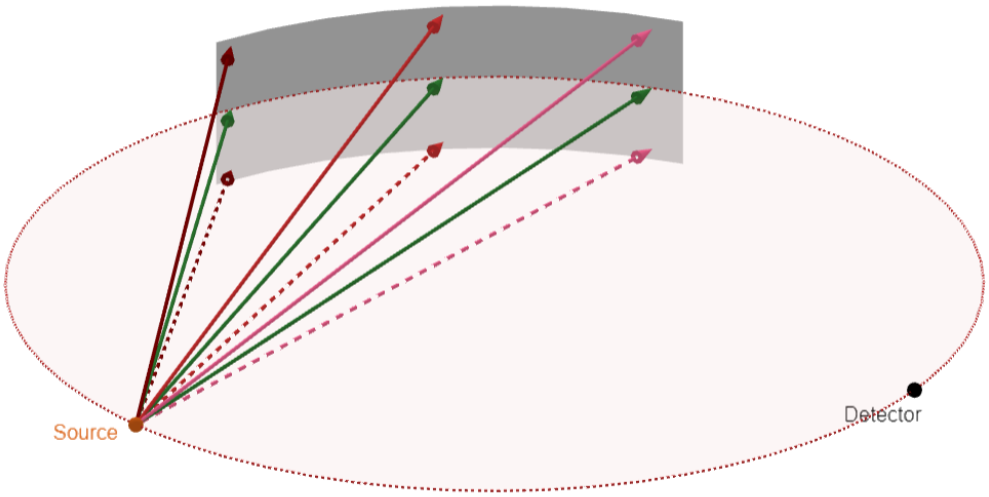

Figure 4.1: Different rays impinging on a cylindrically bent Johansson crystal. In green are depicted the rays at Bragg condition, in shades of red the rays with a slightly different incident angle.

4.1) which causes a degradation of the energy resolution.

The time has come to quantitatively answer the following questions:

1. what is the deviation $\Delta\theta_a$ of a generic ray from the nominal Bragg angle?;
2. what is the energy deviation ΔE_a corresponding to $\Delta\theta_a$?

The answer to the second question is trivial: by differentiating the Bragg's law 3.6 and dividing the result by the Bragg's law itself it is immediate to obtain:

$$\frac{\Delta\lambda}{\lambda_B} = \cot\theta_B \Delta\theta \tag{4.1}$$

and taking advantage of the well-known relation

$$\frac{\Delta\lambda}{\lambda_B} = -\frac{\Delta E}{E_B} \tag{4.2}$$

it comes immediately that

$$\frac{\Delta E}{E_B} = -\cot\theta_B \Delta\theta \tag{4.3}$$

were E_B and λ_B represent the energy and the wavelength, respectively, of the radiation satisfying Bragg condition. In the following, using simple trigonometric relations supported by Figure 4.2 and Figure 4.3, we will find analytical expressions for the angular variation $\Delta\theta_a$ as a function of the crystal coordinates (l and z)[1] in a reference system with origin placed at the center of the crystal. To be more precise, we will work mainly with the complementary angles (identified in the Figures 4.2 and 4.3 with γ_B and γ).

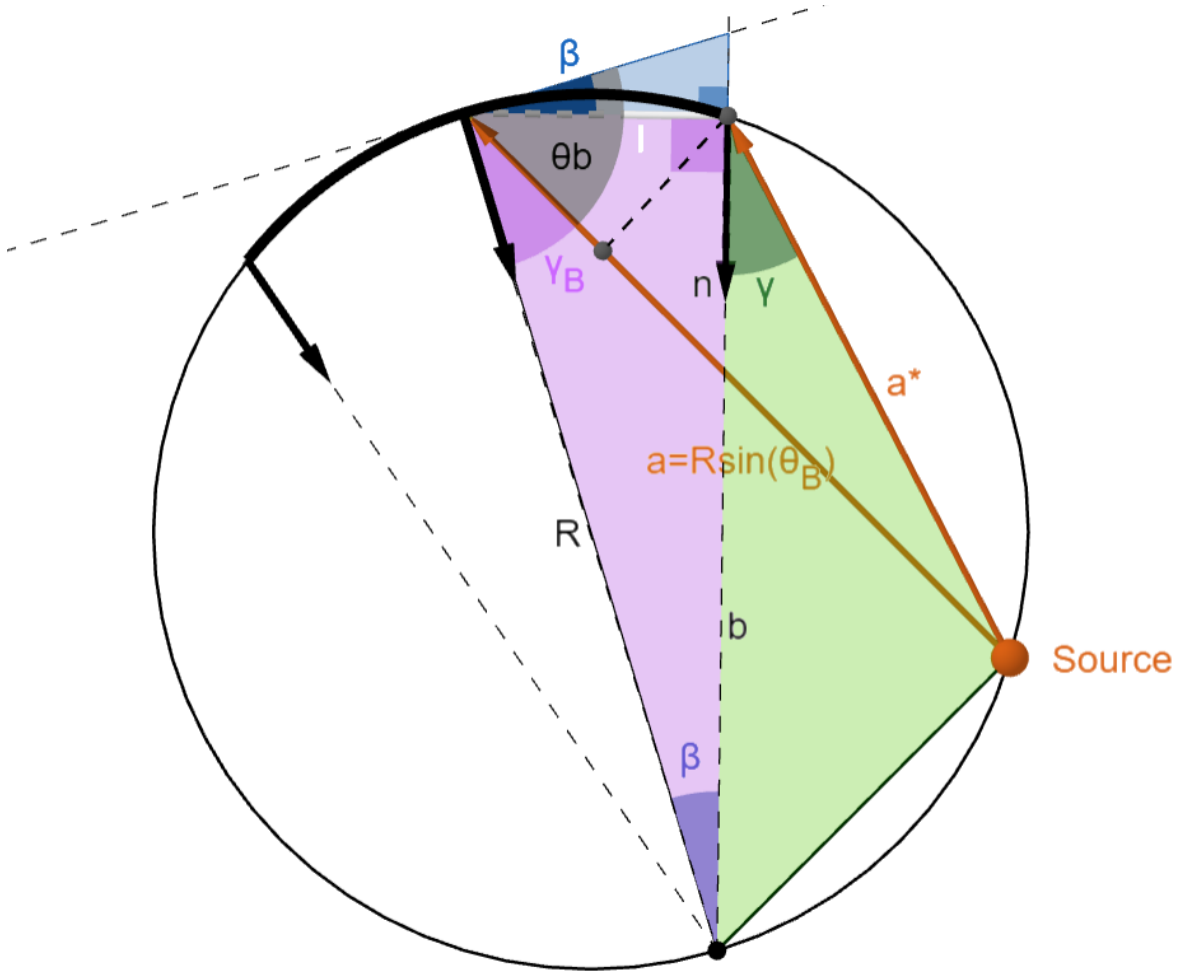

Figure 4.2: View from above of Figure 4.3 particularly useful to visualize the existence of some right triangles. The normal vectors in black are referred to the crystallographic planes of the analyzer.

[1]The corresponding capital letters (L and Z) will be used to indicate the maximum values of these coordinates (i.e. the half-length and half-height of the analyzer).

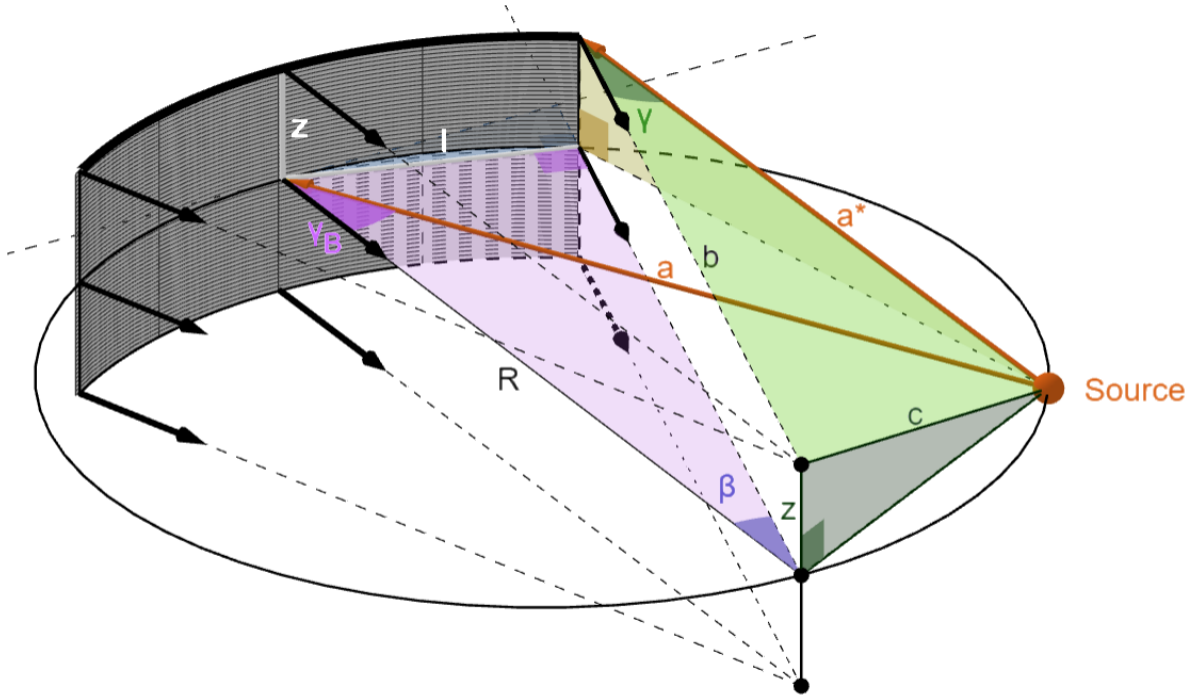

Figure 4.3: 3D representation of two rays (a and a*) incident respectively at the center of the crystal and at the extremity. Additional geometric elements are represented for the sole purpose of supporting the reader in the calculations.

In order to avoid misinterpretations of the figures, it is important to underline that the only elements with physical meaning (apart from the source and the crystal) are the two orange rays (a and a^*) originating from the source and incident on the crystal respectively in the center (it is the nominal ray, incident at θ_B) and in a generic point (with a generic θ incidence angle that will deviate from θ_B as a function of the coordinates (l, z) of the crystal). The other graphical constructions have only the purpose of supporting the reader in the following calculations. Starting from Figure 4.2 and exploiting the Pythagorean theorem on the purple triangle we can write:

$$b = \sqrt{R^2 - l^2} \tag{4.4}$$

then always referring to the purple triangle:

$$\sin\beta = \frac{l}{R} \tag{4.5}$$

Because of the similarity between the purple and blue right-angled triangles, all their

angles are equal. Since the half-length of the crystal L is always much smaller than its curvature radius R we can write:

$$\beta \simeq \frac{l}{R} \tag{4.6}$$

Taking advantage of the relations obtained above and relying on the Figure 4.2 and Figure 4.3 we can find a^* and c applying the Pythagorean theorem respectively on the yellow and dark green right-angled triangle obtaining:

$$\begin{cases} a^* = \sqrt{\left(R\sin\theta_B - l\cos\left(\theta_B - \dfrac{l}{R}\right)\right)^2 + l^2\sin^2\left(\theta_B - \dfrac{l}{R}\right) + z^2}, & \text{(4.7a)} \\ b = \sqrt{R^2 - l^2}, & \text{(4.7b)} \\ c = \sqrt{R^2\cos^2\theta_B + z^2}, & \text{(4.7c)} \end{cases}$$

As shown in Figure 4.3, a^*, b and c are the three sides of the triangle represented in light green. This triangle is not a right triangle. Nevertheless, to relate the sides to the angles we can exploit the generalization of the Pythagorean theorem[2]

$$c^2 = (a^*)^2 + b^2 - 2a^*b \cdot \cos\gamma \tag{4.8}$$

remembering that γ is complementary to the local incidence angle θ we can rewrite 4.8

$$c^2 = (a^*)^2 + b^2 - 2a^*b \cdot \sin\theta \tag{4.9}$$

and so

$$\sin\theta = \frac{(a^*)^2 + b^2 - c^2}{2a^*b} \tag{4.10}$$

by substituting a^*, b and c and making the appropriate simplifications (without any approximation)

$$\sin\theta = \frac{2R^2\sin^2\theta_B - 2Rl\sin\theta_B\cos\left(\theta_B - \frac{l}{R}\right)}{2a^*\sqrt{R^2 - l^2}} \tag{4.11}$$

that can be rewritten as

[2]Also known as the cosine theorem.

$$\sin\theta = \frac{2R\sin\theta_B(R\sin\theta_B - l\cos(\theta_B - \frac{l}{R}))}{2R(R\sin\theta_B - l\cos(\theta_B - \frac{l}{R}))\cdot\sqrt{1-\frac{l^2}{R^2}}\cdot\sqrt{1+\frac{l^2\sin^2(\theta_B-\frac{l}{R})+z^2}{(R\sin\theta_B - l\cos(\theta_B-\frac{l}{R}))^2}}} \tag{4.12}$$

writing the equation in this way is easy to observe how the numerator can be partially simplified. It is also possible to rearrange the roots at the denominator obtaining:

$$\sin\theta\cdot\sqrt{1+\frac{l^2\sin^2(\theta_B-\frac{l}{R})+z^2}{(R\sin\theta_B - l\cos(\theta_B-\frac{l}{R}))^2} - \frac{l^2}{R^2} - \left[\frac{l^2}{R^2}\cdot\frac{l^2\sin^2(\theta_B-\frac{l}{R})+z^2}{(R\sin\theta_B - l\cos(\theta_B-\frac{l}{R}))^2}\right]} = \sin\theta_B \tag{4.13}$$

Thanks to the fact that $\frac{l}{R} << 1$ and $\frac{z}{R} << 1$ the term in square brackets is clearly an infinitesimal of higher order than the others and, consequently, it can be neglected. Developing the root in Taylor series:

$$\sin\theta\cdot\left(1+\frac{l^2\sin^2(\theta_B-\frac{l}{R})+z^2}{2(R\sin\theta_B - l\cos(\theta_B-\frac{l}{R}))^2} - \frac{l^2}{2R^2}\right) = \sin\theta_B \tag{4.14}$$

From equation 4.14 is immediate to obtain the difference $\sin\theta_B - \sin\theta$

$$\sin\theta_B - \sin\theta = \sin\theta\cdot\left(-\frac{l^2}{2R^2} + \frac{l^2\sin^2(\theta_B-\frac{l}{R})+z^2}{2(R\sin\theta_B - l\cos(\theta_B-\frac{l}{R}))^2}\right) \tag{4.15}$$

The last step to be taken in order to conclude the reasoning is to relate the difference between the sines of the incidence angles ($\sin\theta_B - \sin\theta$) with the difference $\Delta\theta_a$ between the angles themselves (what we actually want to calculate). This is possible simply by exploiting the definition of the derivative of the sine function: considering in fact that, in a real case, θ_B and θ will be very close in value, it is quite reasonable to write:

$$\sin\theta_B - \sin\theta \simeq \cos\theta\Delta\theta_a \tag{4.16}$$

Simply by substituting 4.16 inside 4.15 we find:

$$\Delta\theta_a = \tan\theta_B \left(\left[-\frac{l^2}{2R^2} + \frac{l^2 \sin^2(\theta_B - \frac{l}{R})}{2(R\sin\theta_B - l\cos(\theta_B - \frac{l}{R}))^2} \right] + \left[\frac{z^2}{2(R\sin\theta_B - l\cos(\theta_B - \frac{l}{R}))^2} \right] \right) \tag{4.17}$$

Let us now make some physical considerations on the first term in square brackets: it is evident that this term depends only on the l coordinate of the crystal. We know that, in a Johansson crystal, at least when $z = 0$ there can not be any variation in the incident angle due to the l coordinate (Section 3.2.3). From this simple observation we can already deduce that the first term, because of its independence from the z coordinate, must necessarily be null. Let's prove it:

$$\left[-\frac{l^2}{2R^2} + \frac{l^2 \sin^2(\theta_B - \frac{l}{R})}{2(R\sin\theta_B - l\cos(\theta_B - \frac{l}{R}))^2} \right] = \left[-\frac{l^2}{2R^2} + \frac{l^2}{2R^2} \cdot \frac{\sin^2(\theta_B - \frac{l}{R})}{(\sin\theta_B - \frac{l}{R}\cos(\theta_B - \frac{l}{R}))^2} \right] \tag{4.18}$$

finally making use of the well-known trigonometric formula

$$\sin\left(\theta_B - \frac{l}{R}\right) = \sin\theta_B \cos\left(\frac{l}{R}\right) - \cos\theta_B \sin\left(\frac{l}{R}\right) \tag{4.19}$$

and assuming, as already done many times, that $\frac{l}{R} << 1$, Equation 4.18 can be rewritten as:

$$\left[-\frac{l^2}{2R^2} + \frac{l^2}{2R^2} \cdot \frac{(\sin\theta_B - \frac{l}{R}\cos\theta_B)^2}{(\sin\theta_B - \frac{l}{R}\cos(\theta_B - \frac{l}{R}))^2} \right] \simeq \left[-\frac{l^2}{2R^2} + \frac{l^2}{2R^2} \right] = 0 \tag{4.20}$$

We can therefore write the **final formula describing the geometric contribution to the energy resolution of a cylindrical Johansson crystal:**

$$\Delta\theta_a = \tan\theta_B \cdot \left(\frac{z^2}{2(R\sin\theta_B - l\cos(\theta_B - \frac{l}{R}))^2} \right) \tag{4.21}$$

Observing relationship 4.21 just obtained and its representations (Figures 4.4 and 4.5), some observations arise spontaneously:

- $\Delta\theta_a$ is exactly zero $\forall l$ when $z = 0$. It is the main peculiarity of a Johansson analyzer;
- the variable z appears squared: this implies that its sign does not affect $\Delta\theta_a$. Physically this result is quite reasonable as the Rowland circle identifies a symmetry plane for the spectrometer: what happens above this plane must consequently be the same as what happens below (Figure 4.6a);
- contrary to the z variable, the sign of the l variable affects $\Delta\theta_a$ (Figure 4.6b). Again, the result is not surprising. In fact, only in the case in which the source is placed in front of the crystal (back-scattering condition) should a left-right symmetry be expected. In this limit, indeed, there is no longer any dependence on the sign of l as shown below:

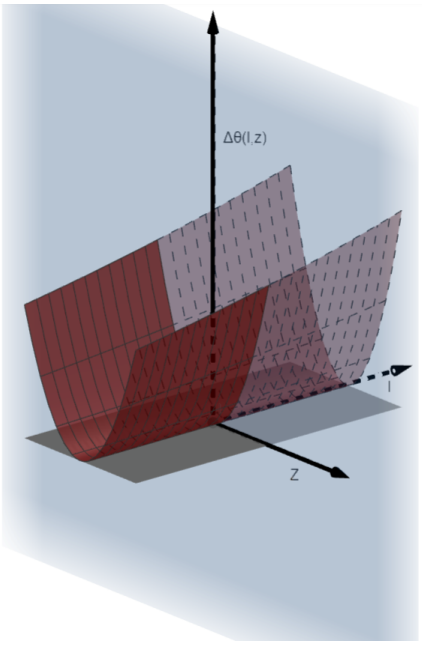

Figure 4.4: 3D plot of Equation 4.21. The effect of coordinate l is exaggerated.

$$\lim_{\theta_B \to\ \pi/2} \left[l \cdot \cos\left(\theta_B - \frac{l}{R}\right)\right] = l \cdot \sin\frac{l}{R} \simeq \frac{l^2}{R}$$

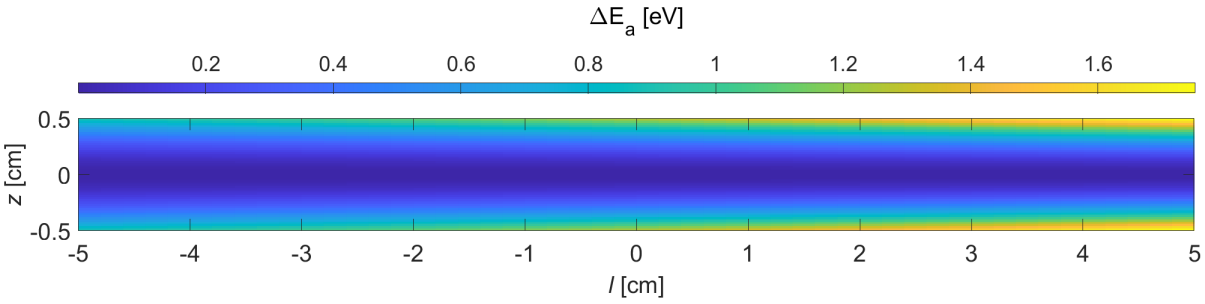

Figure 4.5: Geometric contribution of the analyzer with Rowland diameter R = 50 cm and $\theta_B = 30°$. Different colors indicate different ΔE_a.

- as a last comment it is interesting to underline how the dependence due to the l coordinate becomes more and more important as θ_B decreases. In fact, in formula 4.21 l is multiplied by $\cos\theta_B$. Despite this, however, the contribution due to l will always be less important than that due to z. In fact, for reasonable incidence angles (not too small), the dominant part of the denominator of Equation 4.21 will always be $R\sin\theta_B$. For this reason, in some circumstances only the contribution due to the z coordinate of the stripes will be considered.

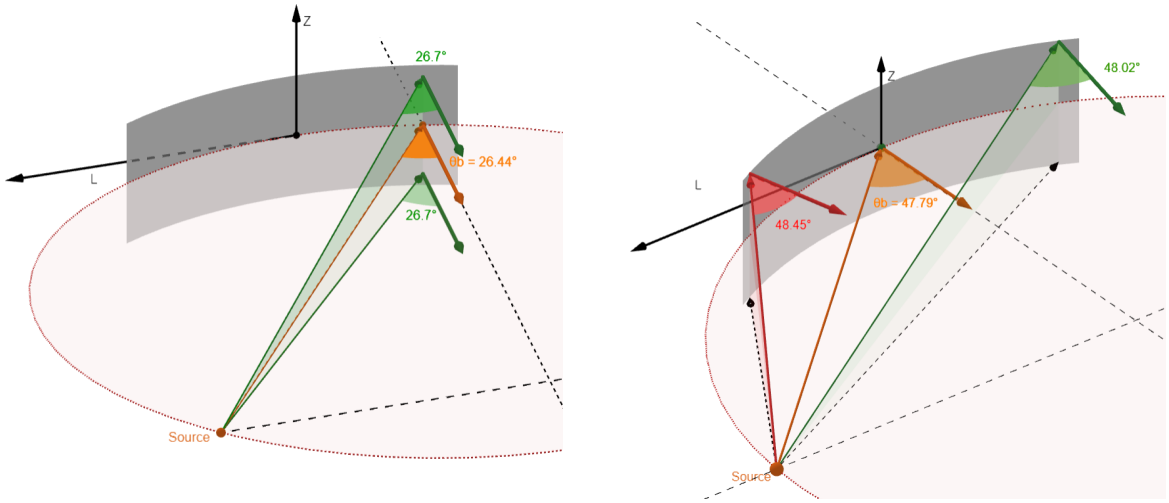

(a) z symmetrical dependence. (b) l asymmetrical dependence.

Figure 4.6: 4.6a shows the symmetrical dependence on the z coordinate (green angles have the same value). 4.6b shows the asymmetrical dependence on the l coordinate (green and red angles have different values).

Comparison with results reported in literature

- Stepanenko [20] reports that, for a Johansson cylindrically bent crystal the following formula holds:

$$\frac{\Delta\lambda}{\lambda_B} \simeq \frac{z^2}{2R^2\sin^2\theta_B} \tag{4.22}$$

that, neglecting the l-component of the crystal, can be directly linked to our result trough Equation 4.1;

- Rovezzi [6] reports the following formula:

$$\Delta\theta_a = \tan\theta_B \left(1 - \frac{1}{\sqrt{1 + \left(\frac{z}{R\sin\theta_B}\right)^2}} \right) \tag{4.23}$$

Simply by expanding the square root at the denominator:

$$\Delta\theta_a = \tan\theta_B \left(\frac{1 + \left(\frac{z^2}{2R^2\sin^2\theta_B}\right) - 1}{1 + \left(\frac{z^2}{2R^2\sin^2\theta_B}\right)} \right) \simeq \tan\theta_B \left(\frac{z^2}{2R^2\sin^2\theta_B} \right) \tag{4.24}$$

that is, neglecting the length l of the crystal, the same result derived in the previous section 4.21.

4.2. Source contribution to the resolution

Following the same ideas of section 4.1 we will now concentrate on the contribution to the energy resolution due to the finite size of the source: in order to take into account only this contribution, in the following we will assume a point-like analyzer.
In analogy with what was done in the previous case, our goal is to derive $\Delta\theta_s$ considering the nominal ray a starting from the centre of the source and a general ray a^* originating from the point $(s_y,\, s_z)$ of the source. As in the previous demonstration, for convenience, Figure 4.7 shows also the complementary angles γ_B and γ.

Our goal will be to find an expression for the generic incidence angle γ. To do this, it is necessary to find the three sides of the triangle highlighted in green in Figure 4.7. Let's start finding b: by applying the cosine theorem to the gray triangle we can write:

$$(b^*)^2 = c^2 + s_y^2 - 2s_y c \cdot \cos\left(\pi/2 - \gamma_B\right) \tag{4.25}$$

Substituting $c = R/2$ in equation 4.25:

$$b^* = \sqrt{\frac{R^2}{4} + s_y^2 - Rs_y \cdot \sin\gamma_B} \tag{4.26}$$

Applying the Pythagorean theorem to the blue triangle it is immediate to obtain b:

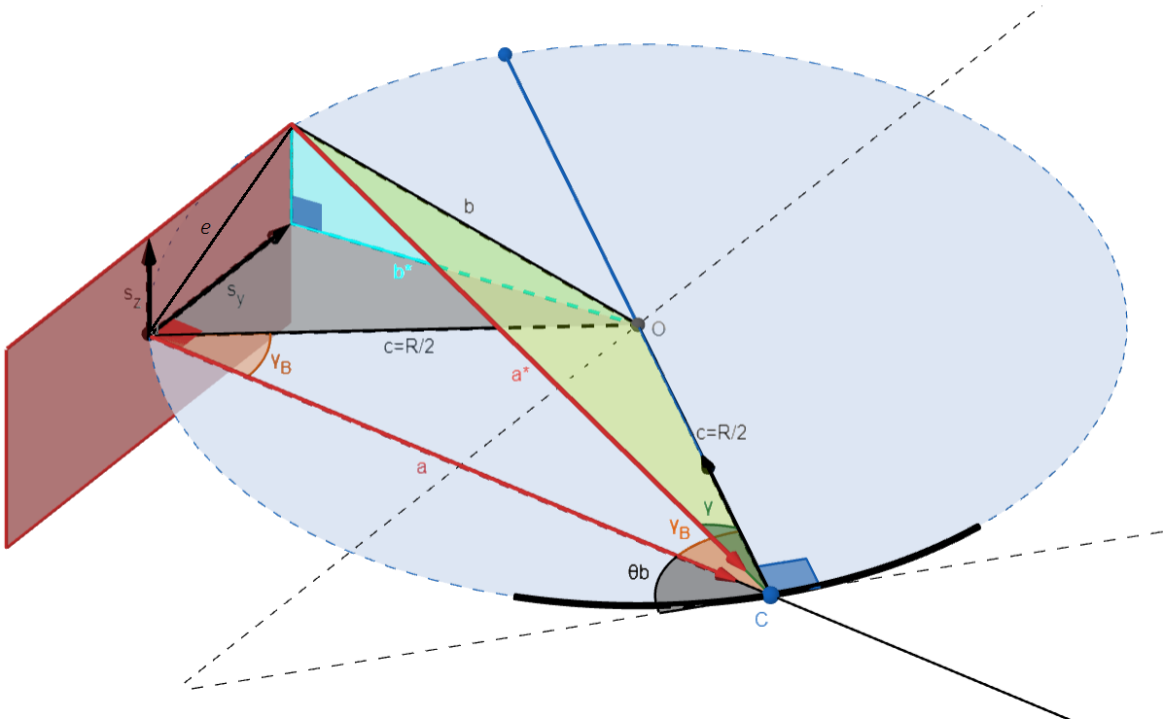

Figure 4.7: 3D representation of two rays (a and a^*) originating respectively from the center of the source and from a generic point (s_y, s_z) where s_y and s_z are the coordinates of the source (represented by the red rectangle) starting from its center. Additional geometric elements are represented for the sole purpose of supporting the reader in the calculations.

$$b = \sqrt{\frac{R^2}{4} + s_y^2 - Rs_y \cdot \sin\gamma_B + s_z^2} \tag{4.27}$$

In order to find a^* we can apply the Pythagorean theorem to the triangle having as catheti a and e and as hypotenuse our unknown a^*:

$$\begin{cases} a = R\sin\theta_B & \text{(4.28a)} \\ e = \sqrt{s_y^2 + s_z^2}, & \text{(4.28b)} \\ a^* = \sqrt{R^2\sin^2\theta_B + s_y^2 + s_z^2}, & \text{(4.28c)} \end{cases}$$

We have therefore obtained, as we set out to do, the three sides of the green triangle:

$$\begin{cases} a^* = \sqrt{R^2 \sin^2\theta_B + s_y^2 + s_z^2}, & (4.29a) \\ b = \sqrt{\dfrac{R^2}{4} + s_y^2 - Rs_y \cdot \sin\gamma_B + s_z^2} & (4.29b) \\ c = R/2, & (4.29c) \end{cases}$$

Using the cosine theorem on this triangle and exploiting the relations[3] $\cos\gamma = \sin\theta$ and $\sin\gamma_B = \cos\theta_B$

$$b^2 = (a^*)^2 + c^2 - 2a^* c \cdot \sin\theta \tag{4.30}$$

Substituting equations 4.29 inside equation 4.30

$$-Rs_y \cdot \cos\theta_B = R^2 \sin^2\theta_B - R\sqrt{R^2 \sin^2\theta_B + s_y^2 + s_z^2} \cdot \sin\theta \tag{4.31}$$

from which it is possible to derive an expression for the sine of the incidence angle:

$$\sin\theta = \frac{R\sin^2\theta_B + s_y \cos\theta_B}{R\sin\theta_B \sqrt{1 + \frac{s_y^2 + s_z^2}{R^2 \sin^2\theta_B}}} \tag{4.32}$$

Since the dimensions of the source are orders of magnitude smaller than R, the square root can be expanded in Taylor series obtaining:

$$\sin\theta \left(1 + \frac{s_y^2 + s_z^2}{2R^2 \sin^2\theta_B}\right) = \sin\theta_B + \frac{s_y}{R}\frac{1}{\tan\theta_B} \tag{4.33}$$

Similarly to what was done in section 4.1 finding the difference $\sin\theta_B - \sin\theta$ and exploiting the definition of the derivative (see 4.16) it is immediate to obtain the **final formula describing the geometric contribution to the energy resolution of the source:**

$$\Delta\theta_s = -\frac{s_y}{R\sin\theta_B} + \tan\theta_B \left(\frac{s_y^2 + s_z^2}{2R^2 \sin^2\theta_B}\right) \tag{4.34}$$

observing equation 4.34 we notice how s_z appears squared unlike s_y which also has a linear term. The square terms of s_z is compatible with the meridional specular symmetry (in total analogy to what has been said for the z component of the crystal). Comparing

[3] the relations are consistent since (γ , θ) and (γ_B , θ_B) are, by definition, complementary angles.

equation 4.21 and 4.34 we notice that the contribution of z and s_z to $\Delta\theta_a$ and $\Delta\theta_s$ respectively, are formally identical because the flat shape of the crystal in the sagittal direction. What is even more important to underline is that, due to the small size of the source, quadratic terms can be totally neglected. Consequently, it will be particularly important to pay attention to the s_y dimension of the source. We can now estimate the total angular deviation given by both the finite source size and the extension of the cylindrical crystal in the sagittal direction.

4.3. Total geometric contribution to the energy resolution

We are now able to estimate how much the incidence angle of a given ray differs from the Bragg angle as a function (separately) of the coordinates (s_y, s_z) of departure and (l, z) of arrival of the ray itself.
At this point, however, it is necessary to underline a further aspect: equations 4.21 and 4.34 do not tell us the probability that a randomly chosen ray deviates by a certain $\Delta\theta$ from the Bragg angle. They only tell us all the possible displacements that we can have. Knowing the probability will allow us to calculate also the statistical weight of each angular deviation $\Delta\theta$. In other words, this frequency distribution can be seen as an answer to the following question: what is the probability that a ray randomly chosen deviates by a given value $\Delta\theta$ from the Bragg angle? In this new context we can see the terms $\Delta\theta_a$ and $\Delta\theta_s$ as *random variables* directly related to their *relative frequency distributions* $p_a(\Delta\theta_a)$ and $p_s(\Delta\theta_s)$, respectively. On the other hand we will be interested in the overall geometric contribution: it can be shown (Appendix C) that, neglecting the component s_z for the source and l for the crystal, the total geometric contribution to energy resolution $\Delta\theta_g$ is simply given by:

$$\Delta\theta_g = \Delta\theta_a + \Delta\theta_s \tag{4.35}$$

the two random variable are so decoupled. Therefore, knowing that the two variables are independent, the correspondent frequency distribution $p_g(\Delta\theta_g)$ is given by the convolution of $p_a(\Delta\theta_a)$ and $p_s(\Delta\theta_s)$ (see Appendix B). By introducing the effect of the l component we are no more authorized to consider Equation 4.35 valid. Nevertheless as will be shown in Chapter 5 the convolution of the frequency distributions is still a very good approximation in order to estimate the real $p_g(\Delta\theta_g)$.

4.3.1. Frequency distribution of the analyzer

The goal of the following paragraph will be to find an analytical formulation for the *relative frequency distribution* referred to $\Delta\theta_a$. All the considerations we will make from now on will be based on the assumption that the analyzer is uniformly irradiated by the source[4]. We therefore calculate the probability $p_a(\Delta\theta_a)d\Delta\theta_a$ that a randomly chosen ray falls in the range $\Delta\theta_a \pm \frac{d(\Delta\theta_a)}{2}$ from the Bragg angle. As graphically suggested by Figure 4.8 this probability is simply the ratio:

$$p_a(\Delta\theta_a)|d\Delta\theta_a| = \frac{4L|dz|}{4LZ} = \frac{|dz|}{Z} \tag{4.36}$$

where the numerator is the area of the two red bands (see Figure 4.8) and the denominator is the area of the analyzer[5]. Since the coordinate l has a limited impact on $\Delta\theta$ we can neglect its effect by setting $l = 0$. In this framework:

$$\Delta\theta_a = \tan\theta_B \left(\frac{z^2}{2R^2\sin^2\theta_B}\right) \tag{4.37}$$

this parabola can be derived obtaining

$$\left|\frac{d\Delta\theta_a}{dz}\right| = \tan\theta_B \left(\frac{|z|}{R^2\sin^2\theta_B}\right) \tag{4.38}$$

thus finding an analytical formula for the frequency distribution:

$$p_a(z) = \frac{|dz|}{Z\cdot|d\Delta\theta_a|} = \frac{R^2\sin\theta_B\cos\theta_B}{Z\cdot|z|} \tag{4.39}$$

using equation 4.37 and substituting it in equation 4.39 we can finally write:

$$p_a(\Delta\theta_a) = \frac{R^2\sin\theta\cos\theta}{\sqrt{2R^2\sin\theta\cos\theta\Delta\theta_a}\cdot Z} = \frac{R\sqrt{\sin\theta\cos\theta}}{\sqrt{2\Delta\theta_a}\cdot Z} \propto \frac{1}{\sqrt{\Delta\theta_a}} \tag{4.40}$$

This result is reasonable and positive for our interests: the more a ray deviates from the Bragg angle, the less its statistical weight will be relevant. This concept is easily deducible from Figure 4.9: the yellow areas are smaller than the red ones. To conclude, a brief observation regarding Equation 4.40 just obtained is proper: this function, representing

[4]This assumption is reasonable and derives directly from the hypothesis $L << R$.

[5]Neglecting the curvature of the crystal and treating it as a rectangle.

a probability density, must necessarily be normalizable (i.e. integrable):

$$\int_0^{\Delta\theta_a^{max}} \frac{1}{\sqrt{\Delta\theta_a}} d\Delta\theta_a \neq \pm\infty \tag{4.41}$$

This *improper integral converge* as expected also if the function 4.40 diverges in $\Delta\theta_a \to 0$.

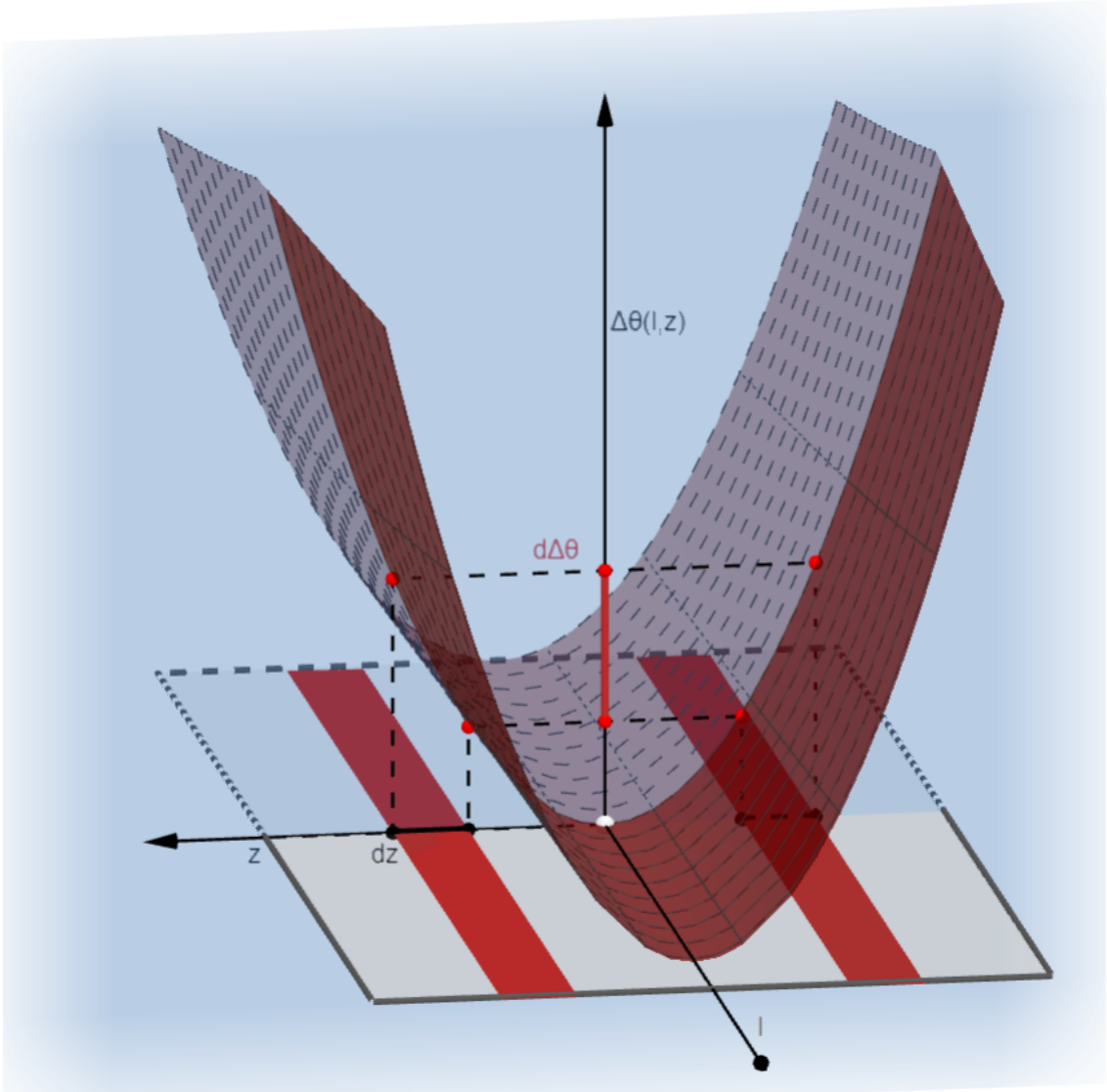

Figure 4.8: Graphical view of the probability $p_a(\Delta\theta_a)d\Delta\theta_a$ under the hypothesis of uniform irradiation of the analyzer. The probability, for a ray, to fall in the interval $d\Delta\theta_a$ is represented by the ratio between the two red areas and the analyzer surface (in gray).

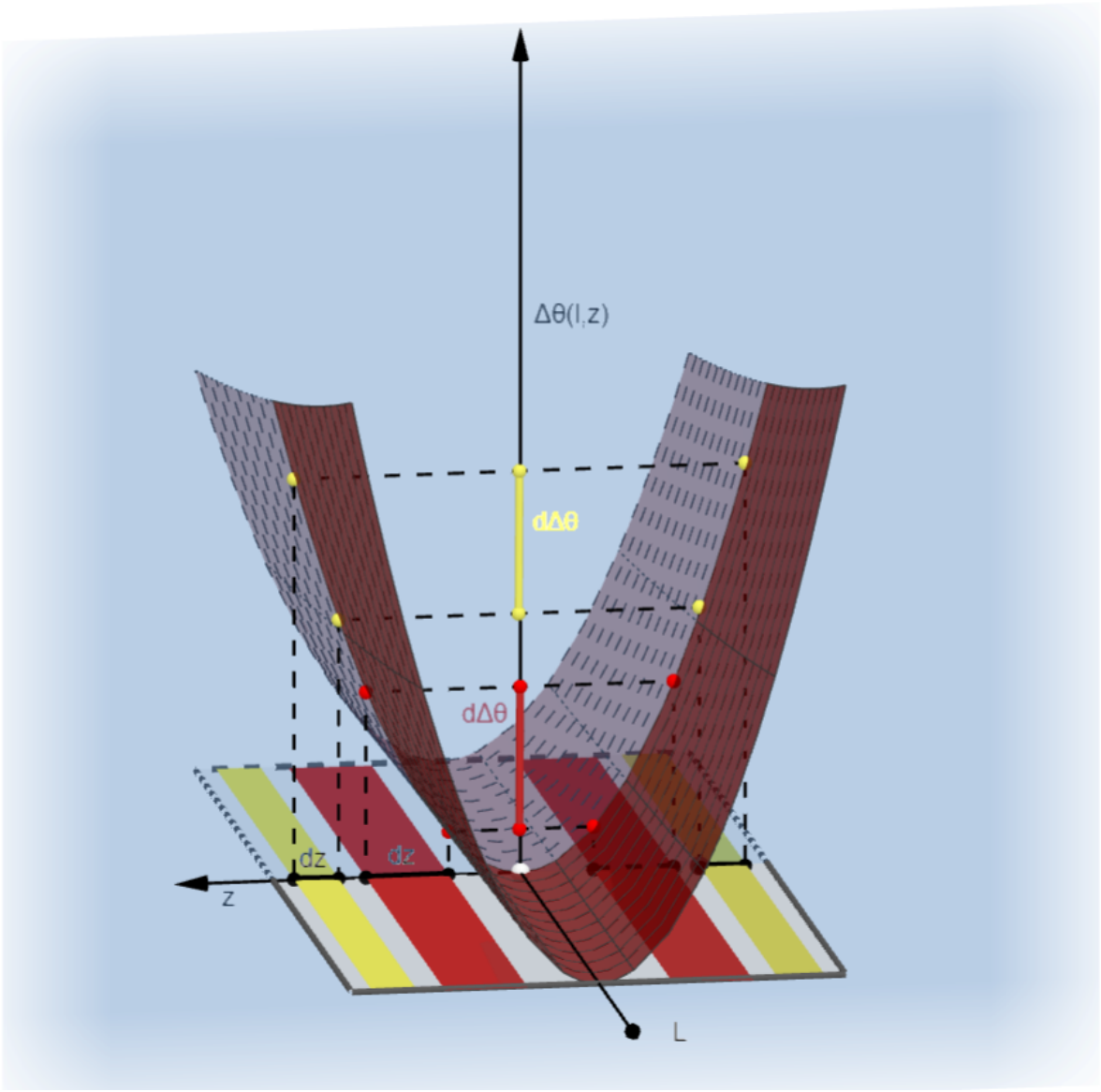

Figure 4.9: Graphical view of the probability $p_a(\Delta\theta_a)d\Delta\theta_a$ under the hypothesis of uniform irradiation of the analyzer. The probability, for a ray, to fall in the interval $d\Delta\theta_a$ red (yellow) is represented by the ratio between the two red (yellow) areas and the analyzer surface (in gray). The probability decreases moving away from the center of the analyzer in the z direction.

4.3.2. Frequency distribution of the source

Following exactly the conceptual scheme of the previous paragraph we will find an analytical formulation for the relative frequency distribution of $\Delta\theta_s$. For convenience Equation 4.34 is here reported neglecting the quadratic terms:

$$\Delta\theta_s = -\frac{s_y}{R\sin\theta_B} \tag{4.42}$$

To underline how true this hypothesis is, note that in Figure 4.10 the effect of quadratic dependencies is deliberately amplified to make it visible.

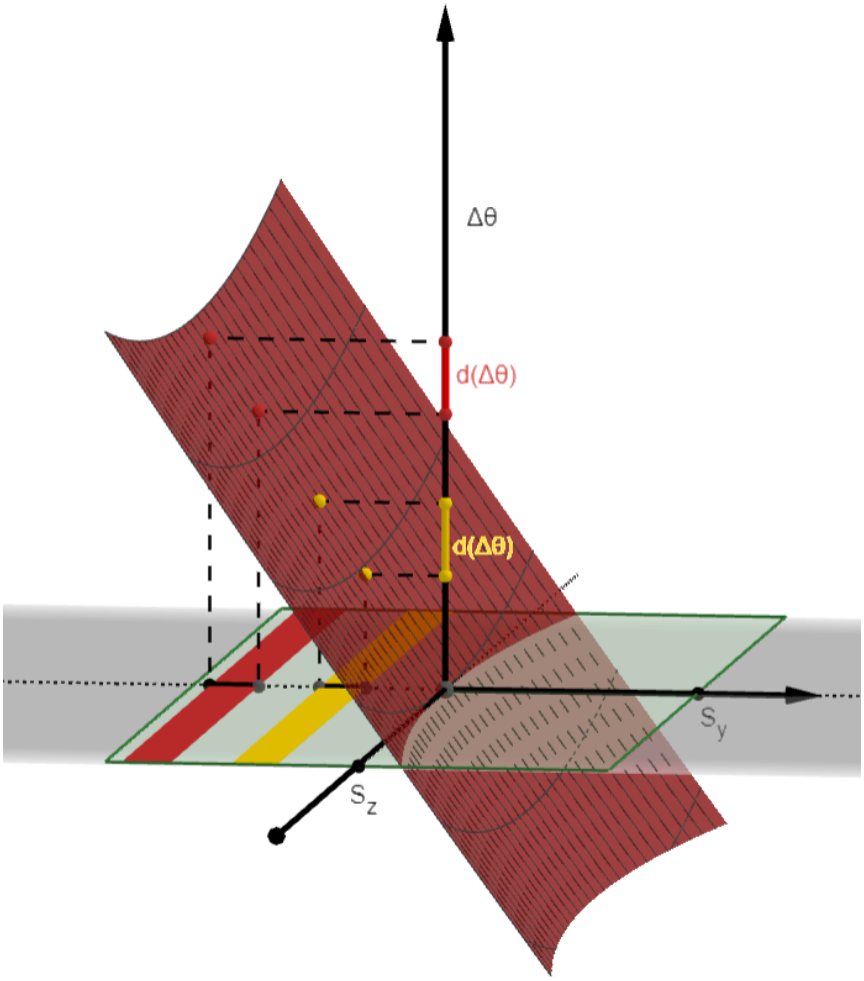

Figure 4.10: Graphical view of the probability $p_s(\Delta\theta_s)d\Delta\theta_s$ under the hypothesis of uniform emittance of the source. The probability, for a ray, to fall in the interval $d\Delta\theta_s$ red (yellow) is represented by the ratio between the red (yellow) area and the analyzer surface (in gray). The probability is constant in first approximation.

Consequently, unlike what happens for the analyzer (see Figure 4.9), in Figure 4.10 the red and yellow areas are equal due to the linear dependence just underlined. This implies a *constant probability distribution*:

$$p(\Delta\theta_s) = constant \tag{4.43}$$

Unfortunately this is not the end of the story: we must consider a Gaussian distribution for the emitted radiation. Coming back to Figure 4.10, despite the fact that the red band has the same area as the yellow one, being the first more in the periphery of the source it will have to be weighted less since it will be less probable, for a ray, to originate from that region. We will assume this weighting function to be a bi-dimensional Gaussian as shown in Figure 4.11

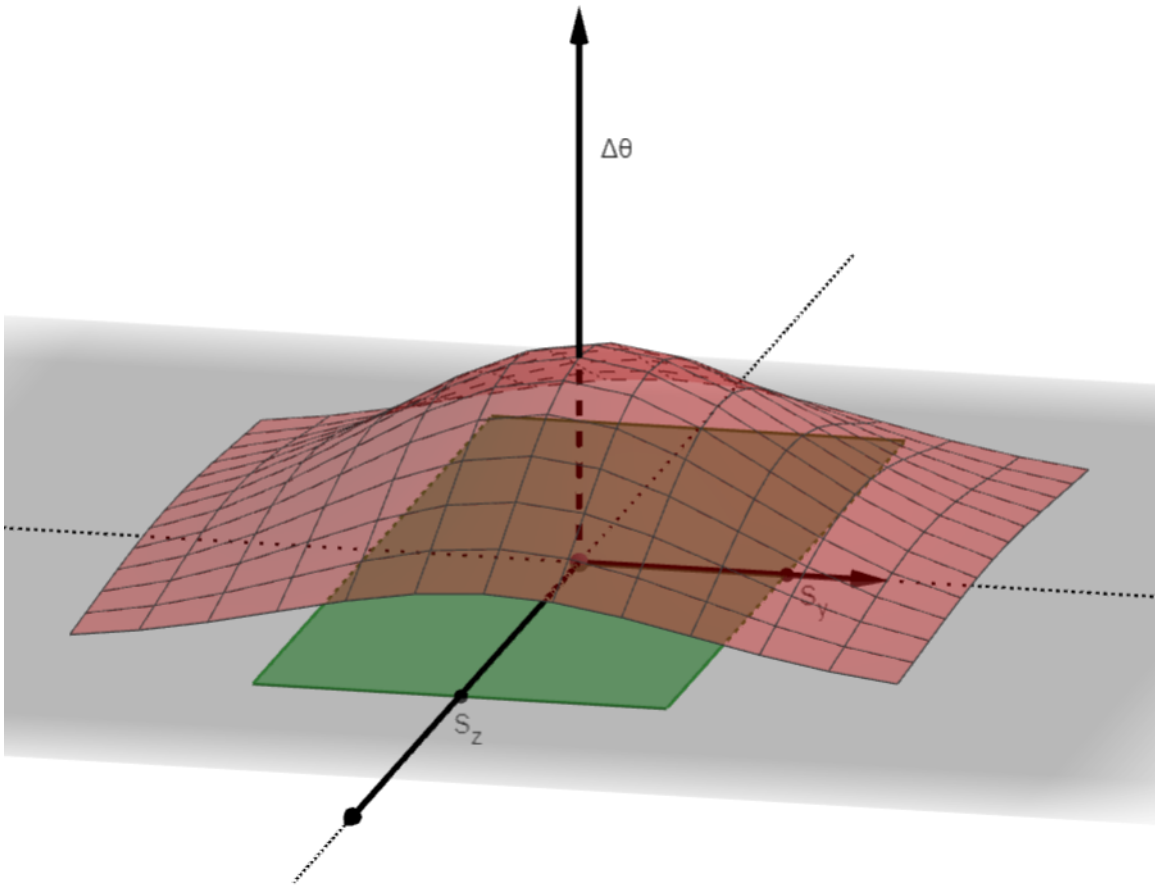

Figure 4.11: The bi-dimensional Gaussian in red representing the decreasing of the radiant emittance of the source (in green) starting from its center and going to the periphery.

As a direct consequence of the reasoning just made, in order to calculate the *frequency distribution of the source* it will be necessary to multiply Equation 4.43 by the Gaussian weighting function obtaining:

$$p_s(s_y, s_z) = C \cdot \exp\left[-\frac{s_y^2}{2\sigma_y^2} - \frac{s_z^2}{2\sigma_z^2}\right] \tag{4.44}$$

where s_y and s_z are the coordinates of a generic point of the source and σ_y and σ_z are the standard deviations of the 2D-Gaussian. In order to find $p(\Delta\theta_s)$ we can use equation 4.42 considering only the linear dependence on s_y:

$$p_s(\Delta\theta_s) = C \cdot \exp\left[-\frac{R^2 \sin^2\theta_B (\Delta\theta_s)^2}{2\sigma_y^2}\right] \tag{4.45}$$

Clearly the standard deviation σ_y must be intimately linked to the size of the source in the meridional direction and related to its FWHM by the relation:

$$FWHM_y = 2\sqrt{2\ln 2}\sigma_y \simeq 2.355\sigma_y \tag{4.46}$$

After this long journey we are finally able to estimate the probability for a ray to deviate by $\Delta\theta_s$ from the Bragg angle. Putting things together we are now able to determine the overall probability distribution $p_g(\Delta\theta_g)$ that, thanks to the independence between $\Delta\theta_a$ end $\Delta\theta_s$ (see Appendix C) is simply given by the convolution (see Appendix B) of $p_a(\Delta\theta_a)$ and $p_s(\Delta\theta_s)$:

$$p_g(\Delta\theta) = \int p_a(\Delta\theta - \Delta\theta') p_s(\Delta\theta') d\Delta\theta' \tag{4.47}$$

As a last comment it may be useful to note how the analyzer contribution (Equation 4.40) admits only positive $\Delta\theta_a$ unlike the source contribution (Equation 4.45) which, being Gaussian, is perfectly symmetrical. Therefore, the overall probability will appear as symmetric (asymmetric) if the source (analyzer) contribution dominate.

5 | Ray tracing simulations

Nowadays, *ray tracing software* are powerful means to simulate the behavior of electromagnetic radiation interacting with optical systems of various kinds. These programs have been improved and adapted over the years specifically for the study of synchrotron radiation as evidenced by the numerous programs available. Despite the vast availability of programs that, albeit with difficulty, could have been adapted to our specific case, it was considered less expensive and more instructive to write a simple ray tracing program able to provide us detailed information on *the geometric resolution* and *the focal properties* of the instrument.

5.1. The software: an overview

The basic idea on which the program is founded is extremely simple: rays originating from a source hit the crystal in such a way that the latter is uniformly irradiated[1] and are labelled according to their incidence angle. After reflection from the crystal, they are intercepted by a plane placed in the position of the detector and oriented in the direction of the crystal: from the intersection of the reflected rays with the plane it will be possible to obtain information on the focal shape and size. Furthermore, the energy distribution of the rays captured by the detector can be determined. All these information will be discussed, comparing them with the results predicted by the theory developed in Chapter 4. We will now go into more details, describing some features of the program:

The source

As already anticipated, the source is modeled by a set of *coplanar points* from which a number m of rays pre-established by the user will originate. The distribution of the points is clearly crucial and has a direct impact on the simulated resolution; in particular, *three source configurations* have a physical sense since, each of these allows to highlight a particular characteristic of the instrument:

[1] Hypothesis used to derive the results of section 4.1 and subsection 4.3.1.

1. *Point-like source:* this configuration allows to simulate the single geometric contribution deriving from the extension of the analyzer, thus allowing direct comparisons between results simulated and predicted from the developed theory (see chapter 4);
2. *Uniformly distributed rectangular source:* this configuration, if coupled to that of a point-like analyzer, will allow us to simulate only the geometric contribution deriving from the extension of the source, thus allowing a direct comparison with the results obtained in section 4.2;
3. *Gaussian source:* it is the configuration that should best approximate the real case. The specifications provided by INCOATEC indicating the size of the source, in fact, refer to the FWHM in both directions[2]. The user will insert the two FWHM values of the 2D Gaussian and the software will return a distribution of points in the plane randomly chosen with the only constraint that their surface density is Gaussian.

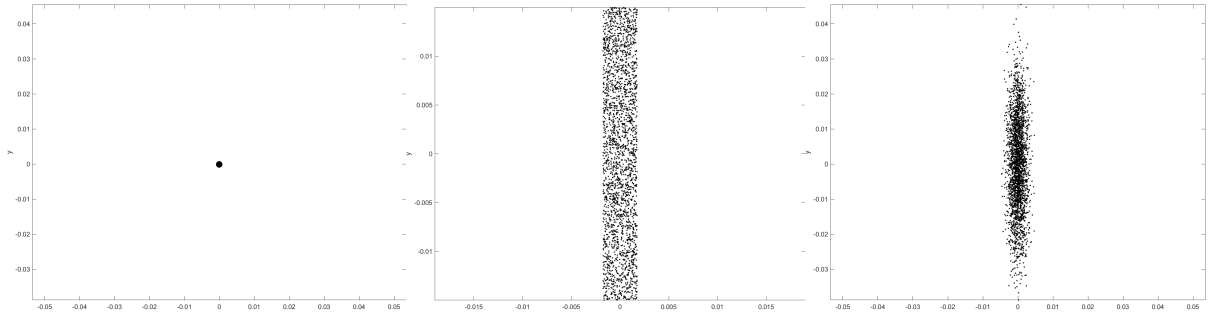

(a) Point-like source (b) Uniform rectangular source (c) Gaussian source

Figure 5.1: (a)Is a source made of a single point. (b)Is obtained starting from 2500 points uniformly distributed on a rectangular surface with sides $S_y = 35\,\mu m$ and $S_z = 300\,\mu m$. (c)Is obtained starting from 2500 randomly-chosen points distributed following a 2D Gaussian with $FWHM_y = 35\,\mu m$ and $FWHM_z = 300\,\mu m$.

The crystal

The crystal is modeled by the software considering two cylindrical surfaces:
one has the curvature radius of the Rowland circle and represents the real surface of the crystal[3]; the other one represents the crystallographic plane and, consequently, it will have a curvature radius doubled if compared to the previous surface. This is the surface that acts as a mirror i.e. the optical element with respect to which the rays coming from the

[2]More precisely following the specifications provided by Incoatec $FWHM_y = 35\,\mu m$ and $FWHM_z = 300\,\mu m$.

[3]Remember that a Johansson crystal is obtained starting from a Johann crystal and digging its surface in such a way that it could con-kiss everywhere the Rowland's circle (see subsection 3.2.3).

source will be reflected. The correspondence between incidence angle and reflected energy is given by the Bragg's law 3.6 considering the actual distance between crystallographic planes. The simulations reported in the following chapter will always refer to Ge[220] reflection ($a = 5.66$Å) and successive harmonics[4].
In summary, each ray will travel a straight path until it intercepts the first surface. At the intersection point, the reflection with respect to the normal referred to the second surface (crystallographic plane) will take place, thus allowing to exactly simulate the geometric behavior of a Johansson-type crystal. Reflected rays will continue along a straight path until they intercept the plane of the detector. The user can choose in how many points the crystal should be hit (this number is equivalent to the number m of rays starting from each point of the source). By choosing a single ray for each point of the source, the crystal will be hit only in its center, thus allowing only the geometric effects deriving from the extension of the source to be resolved. By choosing a different number of rays m, instead, the program will arrange the incidence points on the surface of the crystal so that they are equally distributed.

The detector

The reflected rays will continue along a straight path until they intercept the plane of the detector. The normal to this plane will always be oriented in the direction of the analyzer and, from the intersection between this plane and the rays, it will be easy to trace the size and shape of the focus. At the same time, however, it is important to underline how the rays incident on the crystal are labeled by their incidence angle. This will allow to go back directly both to the variable $\Delta\theta$ for each focal point and to the frequency distribution associated with it, first of all simulating the limiting cases of point-like source and point-like analyzer theoretically treated in the previous chapter and, finally, by coupling the two effects which, being independent, will lead to a frequency distribution very close to the convolution between the distributions of the two limiting cases. The chapter will continue according to this logic and this order trying to highlight the most interesting aspects from a physical point of view.

[4]As demonstrated in subsection 3.1.2, for a diamond-like crystal [440] and [660] reflections are allowed.

5.2. Simulation for the individual contributions

We start from the analysis of the analyzer and source contributions separately. The simulations reported below, unless otherwise specified, will always refer to a curvature radius of the crystallographic planes (Rowland circle diameter) $R = 50\,\text{cm}$ and a cylindrical Johansson-type crystal of length $2L = 10\,\text{cm}$ e width $2Z = 1\,\text{cm}$.

5.2.1. Analyzer contribution to energy resolution

The simulations shown in Figure 5.3 were made by taking 2500 rays with origin in the center of the source. These simulations must therefore be compared to Equation 4.21. As already pointed out in Chapter 4, the dependence due to the l coordinate becomes more and more important as θ_B decreases. This effect is clearly evident also in the simulations, especially when comparing Figure 5.3a with Figure 5.3d. As the simulations show, although this effect is negligible at high angles it becomes comparable to the contribution along the z coordinate going down in incidence angles. In Figure 5.2 the maximum displacement in energy predicted by Equation 4.21 and Equation 4.24 are compared with the simulated values. It is evident how, maintaining the l dependence in the formula for the energy resolution has greatly improved the agreement with the simulated data.

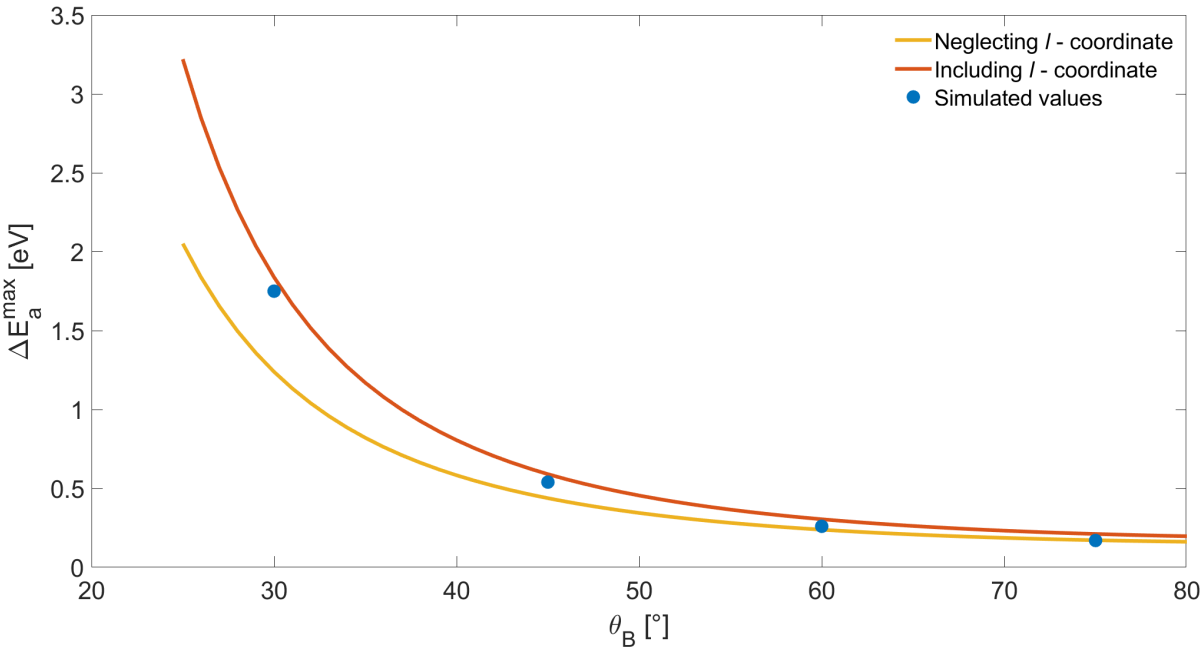

Figure 5.2: Maximum values $\Delta E_a^{max}(\theta_B)$ predicted by Equation 4.21 and 4.24 and simulated (Figure 5.3). Ge[220] reflections are here considered.

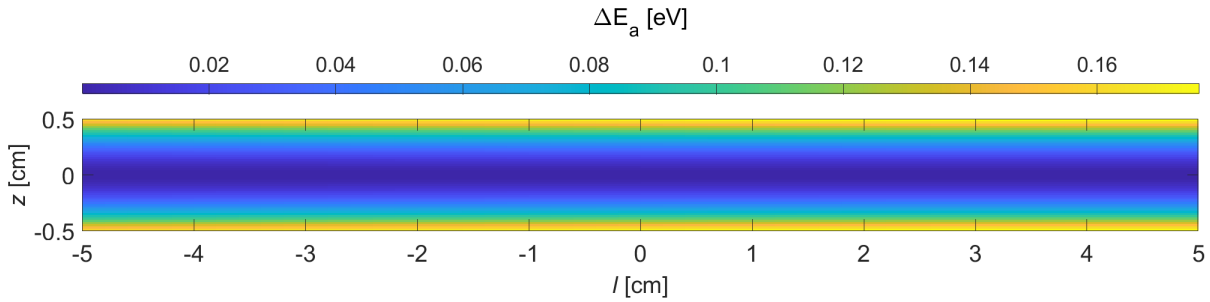

(a) Front view of the crystal when $\theta_B = 75°$.

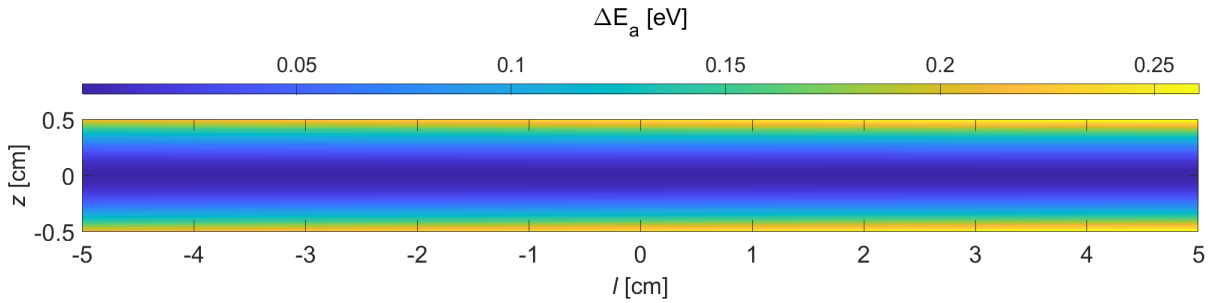

(b) Front view of the crystal when $\theta_B = 60°$.

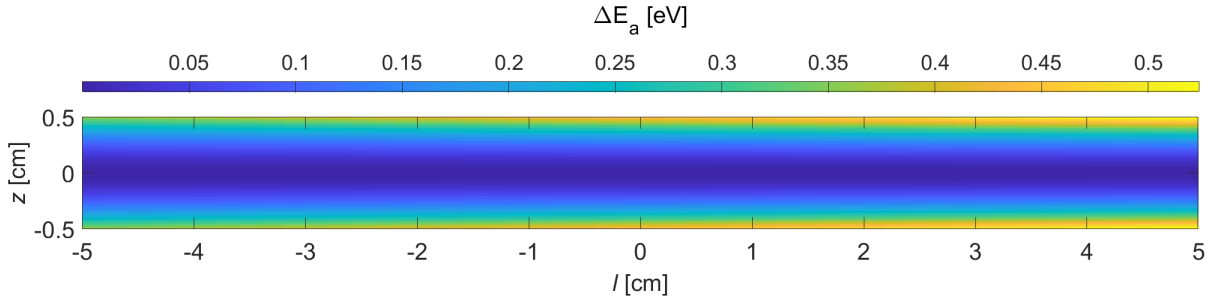

(c) Front view of the crystal when $\theta_B = 45°$.

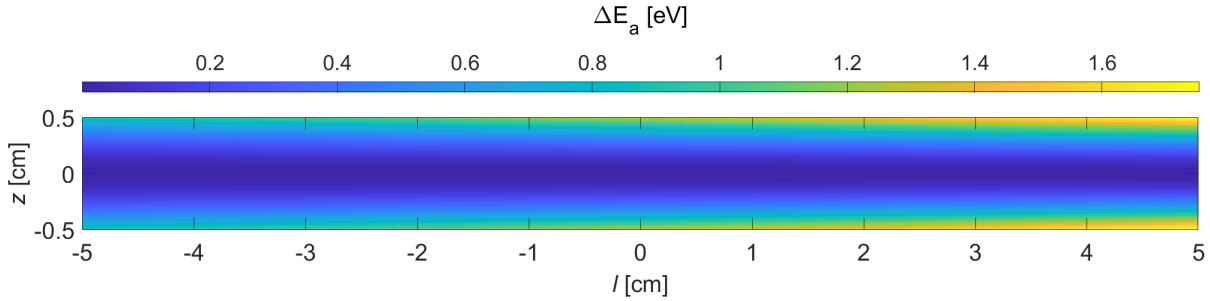

(d) Front view of the crystal when $\theta_B = 30°$.

Figure 5.3: Front view of the crystal: different colors represent different deviations ΔE_a from the Bragg energy (in the center of the analyzer). As the deviation increases, the colors turn from blue to yellow. Ge[220] reflections are here considered.

At this point, I think it is right to make a simple consideration that will be useful in a little while: as shown in Figure 5.3, the region of the crystal that provides a larger ΔE_a is always the part on the right (the one with $l > 0$). Looking at Figure 4.3, it is clear that the positive l regions are the parts of the crystal closest to the source. This is logical since, from the point of view of the source, the closest crystal region will appear more extended and, consequently, will be responsible for a worse energy resolution. Soon, this observation will help us to highlight a weak point of all theoretical treatment and of the simulations.[5]

We now turn to discuss the frequency distributions already extensively described in section 4.3.1. The software allows to count and separate the rays into energy intervals, producing the histograms shown in Figure 5.4. These must now be compared with the theoretical result predicted in subsection 4.3.1 and reported for convenience below:

$$p_a(\Delta\theta_a) \propto \frac{1}{\sqrt{\Delta\theta_a}} \propto \frac{1}{\sqrt{\Delta E_a}} \tag{5.1}$$

It is evident that the histograms are well approximated by the theoretical (red) curves up to a value of ΔE_a (about 0.16 eV for Figure 5.4a and 0.9 eV for Figure 5.4b) that, increasing the Bragg angle θ_B, approaches ΔE_a^{max} simulated. This discrepancy is due to the fact that, in deriving equation 5.1 we neglected the l-dependence of $\Delta\theta_a$ (or ΔE_a), not thereby including the contributions given from the edges of the analyzer which lead to a slight worsening of the energy resolution. This is the reason why, the simulations show a tail (longer if θ_b is small) not predicted by the analytical p_a. Thus, the discrepancy between theoretical and simulated data is explained. The tails are due to the meridional extension l of the crystal and follow a different trend. As we already know, the dependence in l becomes more and more important as θ_B decreases. In fact, if in Figure 5.4a the tail involves only few rays, the same cannot be said for Figure 5.4b. This show the importance of taking into account the meridional dimension of Johansson-type crystals at small Bragg angles.
We have critically analyzed the simulations in the case of a point-like source, comparing these results with those predicted by the approximate theory and finding coherence between the discrepancies shown by the theory, considering the approximations made to derive it. As a last question: how could simulations differ from reality?

[5] I strongly believe it is the only, albeit small, geometric approximation made by the ray tracing simulation.

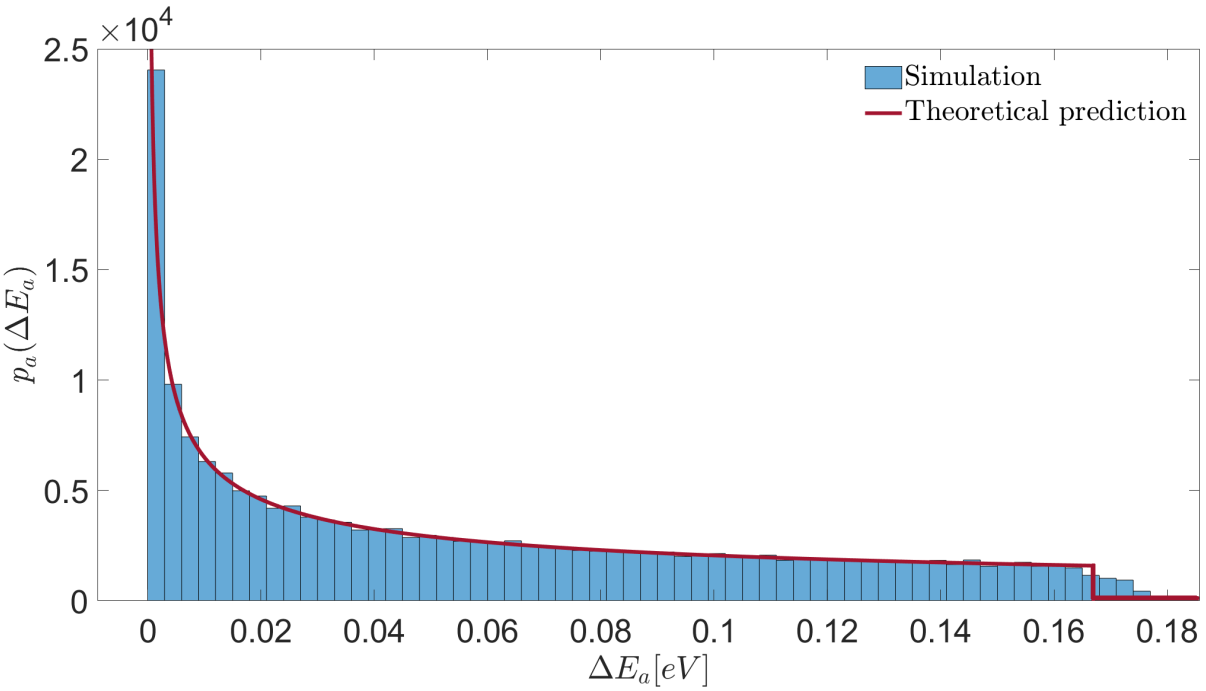

(a) Frequency distribution when $\theta_B = 75°$ compared with theoretical prediction

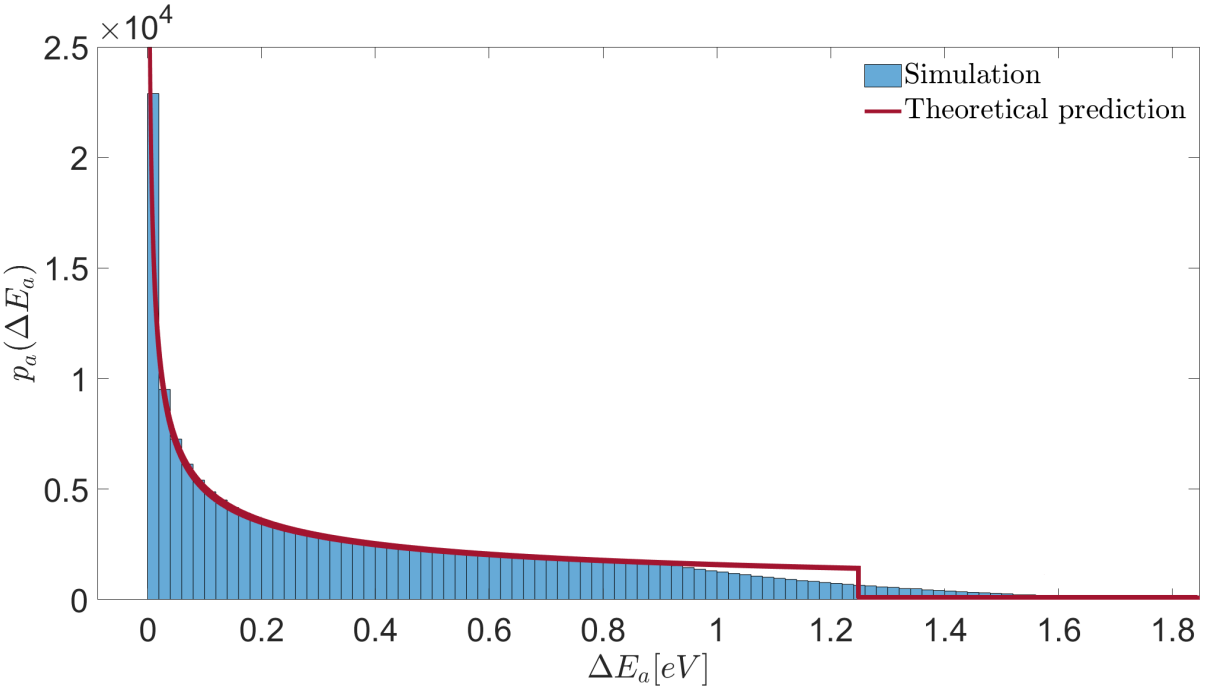

(b) Frequency distribution when $\theta_B = 30°$ compared with theoretical prediction

Figure 5.4: Frequency distributions in the two extreme conditions ($\theta_B = 75°$ and $\theta_B = 30°$) simulated with a point source and 90000 rays impinging uniformly the crystal. The red curve represents the trend 5.1 predicted in section 4.3.1. Ge[220] reflections are here considered.

The only real approximation that has been made in writing the code is to assume that the crystal is uniformly irradiated at any θ_B. However, it must be emphasized that, especially at low incidence angles, there is a region of the crystal closer to the source and a region further away (see Figure 5.5). The emission cone of the source will have a certain divergence so that, as the distance from the source increases, it is absolutely logical to expect a decrease in the density of rays. The closest part of the crystal will therefore be more irradiated than the farthest part. As noted earlier the neighboring part of the crystal is also the one that contributes most to the resolution degradation. For this reason it is logical to expect more rays at high ΔE_a and fewer at low ΔE_a than in the simulated histograms 5.4. However, I am strongly convinced that this effect is negligible given the small length of the crystal compared to the typical distances between source and crystal. A future software update may include this effect to make simulations even more realistic than they already are.

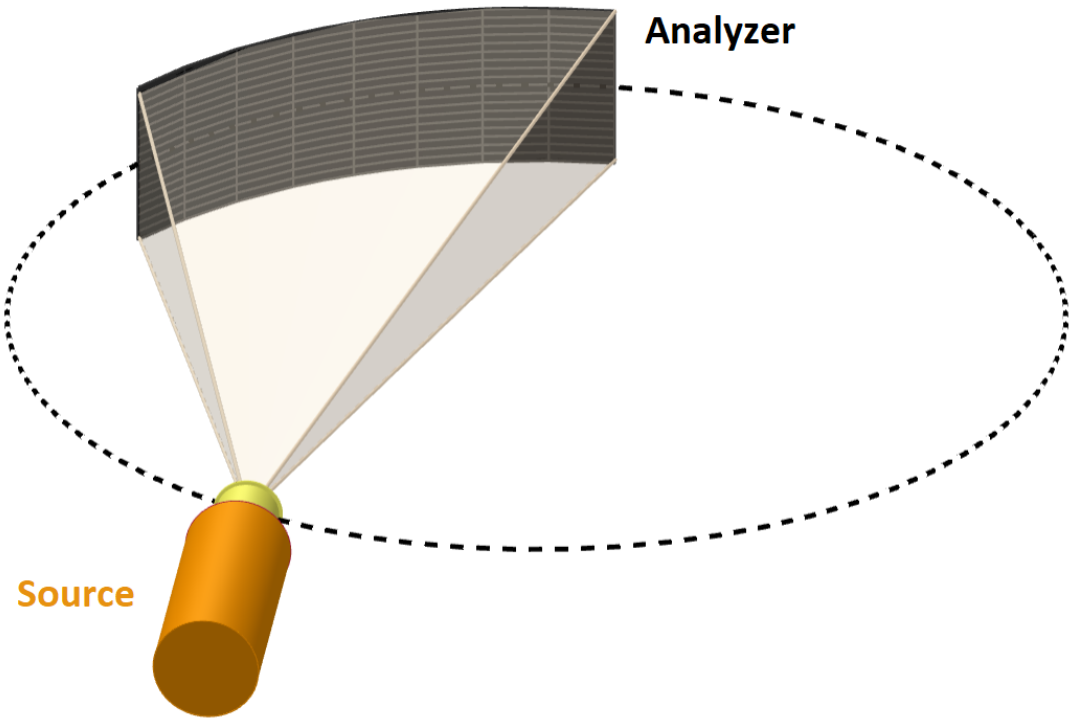

Figure 5.5: The beam emitted by the source hits the analyzer: especially at grazing incidence, the farthest part of the crystal will be irradiated less than the nearer part.

5.2.2. Source contribution to energy resolution

We will now carry out an analogous analysis considering a point analyzer and an extended source to isolate its geometric contribution. First of all, rectangular sources will be simulated: in this way, in fact, it is possible to exactly estimate the ΔE_s^{max} predicted by the theory (equation 4.34) as the latter was obtained under the hypothesis of rectangular source (see section 4.2). We will then move on to a detailed analysis of the real case of practical interest, namely that of a Gaussian source.
The theoretical result find in section 4.2 is here reported for practicality transforming the deviations in angle into deviations in energy simply through equation 4.3 and neglecting quadratic dependencies:

$$\Delta E_s = -E \cot\theta_B \left[-\frac{s_y}{R \sin\theta_B} \right] \tag{5.2}$$

From this result then, it was possible to obtain a constant frequency distribution (see section 4.3.2):

$$p_s(\Delta E_s) = constant \tag{5.3}$$

The simulations shown in (Figure 5.6) refer to a rectangular source ($2S_y = 35\,\mu m$ and $2S_z = 300\,\mu m$) composed of 90000 points chosen randomly within the rectangular surface, each originating a ray. The histograms clearly show a flat frequency distribution as expected. Furthermore, it is confirmed that the effects of quadratic terms, neglected in the analytical expression for the frequency distribution of energies, are negligible. It can be deduced because the simulations are totally symmetrical: the quadratic terms, on the other hand would make the histograms weakly asymmetric (see Equation 4.34). It is important to underline the fact that the source, unlike the analyzer, has dimensions of the order of µm and therefore, the assumption $S_{y_z}/R \ll 1$ is certainly more effective than the assumption $L/R \ll 1$ made in the case of the analyzer. For this reason we expect, for the source, a better agreement between analytical results and simulations.

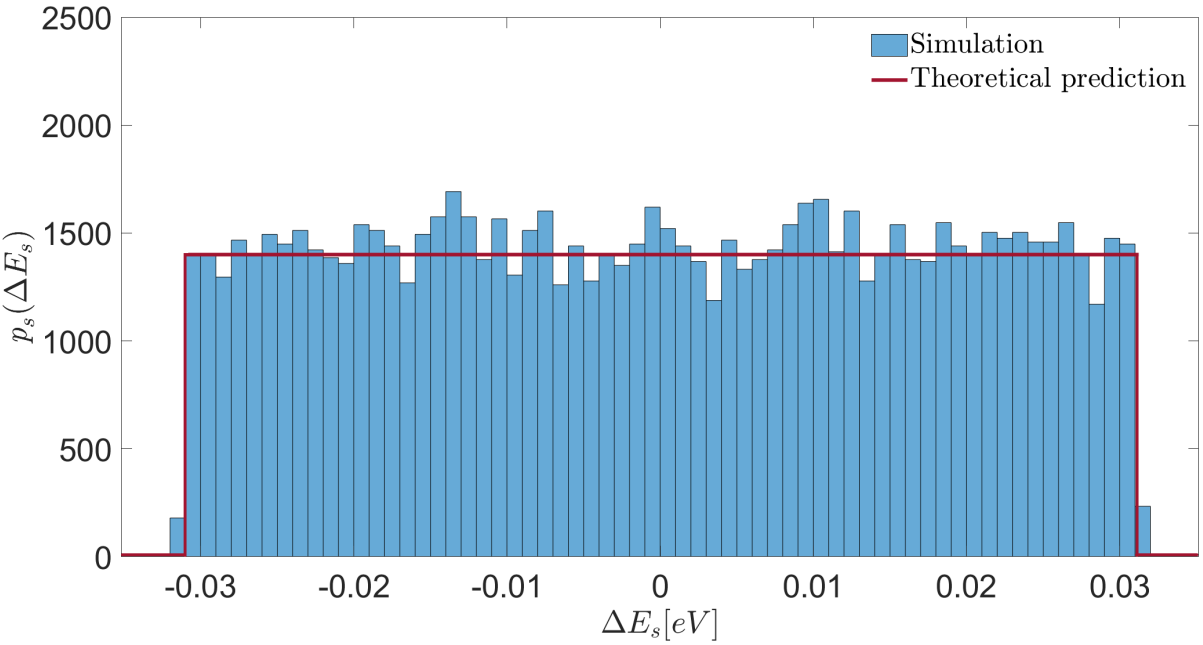

(a) Frequency distribution when $\theta_B = 75°$

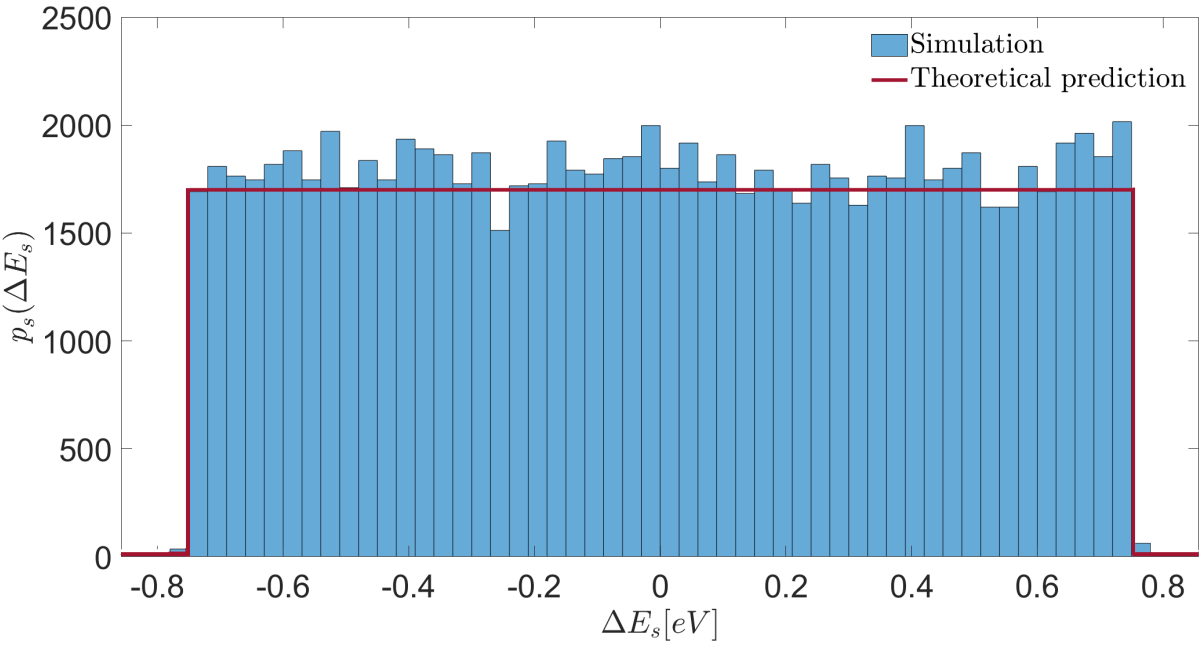

(b) Frequency distribution when $\theta_B = 30°$

Figure 5.6: Frequency distributions in the two extreme conditions ($\theta_B = 75°$ and $\theta_B = 30°$) simulated with a rectangular source (35×300 µm^2) and 90000 rays impinging in the centre of the crystal. Ge[220] reflections are here considered.

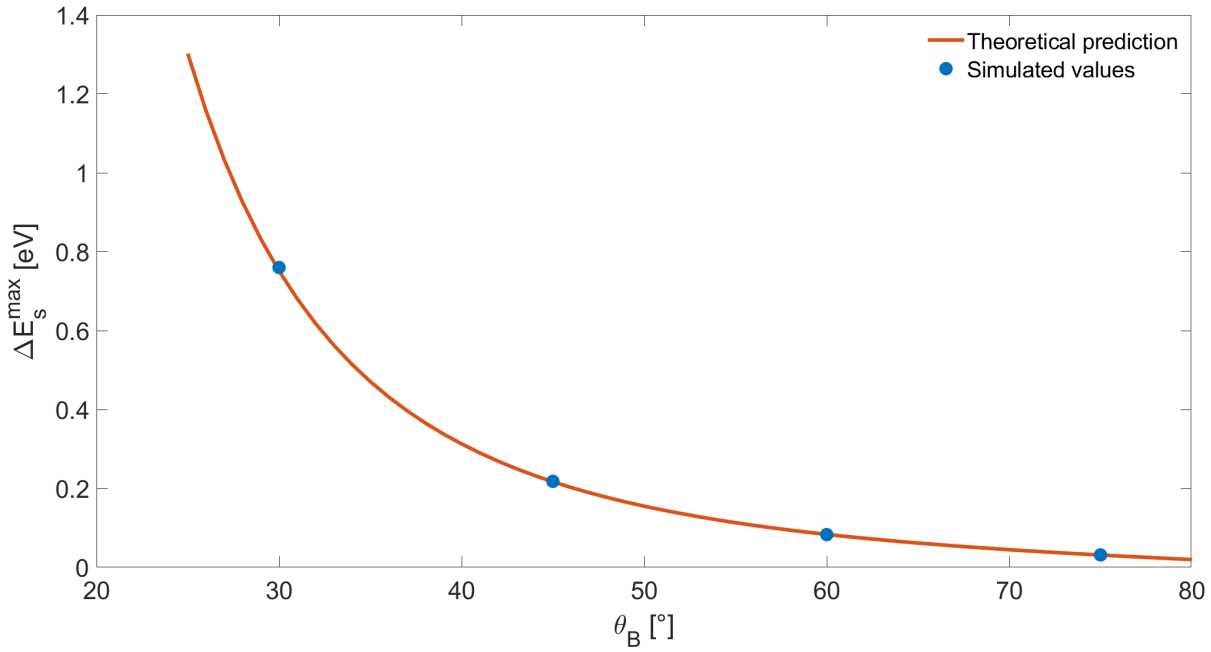

Figure 5.7: Maximum values $\Delta E_s^{max}(\theta_B)$ theoretically predicted and simulated. Ge[220] reflections are here considered.

In the case of a source with a Gaussian distribution of points, as seen in section 4.3.2 also the frequency distribution will change from a constant to a Gaussian:

$$p_s(\Delta E_s) = C\ \exp\left[-\frac{(2\sqrt{2\ln 2})^2\ R^2 \sin^2\theta_B\ \tan^2\theta_B\ (\Delta E_s)^2}{2\ E^2\ FWHM_y^2}\right] \tag{5.4}$$

This is a Gaussian with zero mean and standard deviation σ_s:

$$\sigma_s = \frac{E \cdot FWHM_y}{2\sqrt{2\ln 2}\ R\ \sin\theta_B\ \tan\theta_B} \tag{5.5}$$

where $FWHM_y$ is the full width at half maximum dimension of the source in the meridional plane. Clearly, considering the successive harmonics (Ge[440] and Ge[660]) the reflected energies will be respectively double and triple and, consequently, the standard deviation. In Figure 5.9, the theoretical standard deviation (Equation 5.5) is plotted. In particular, also the standard deviations obtained by the Gaussian fit of the simulations (Figure 5.8) are reported in order to emphasize the perfect agreement with theory.

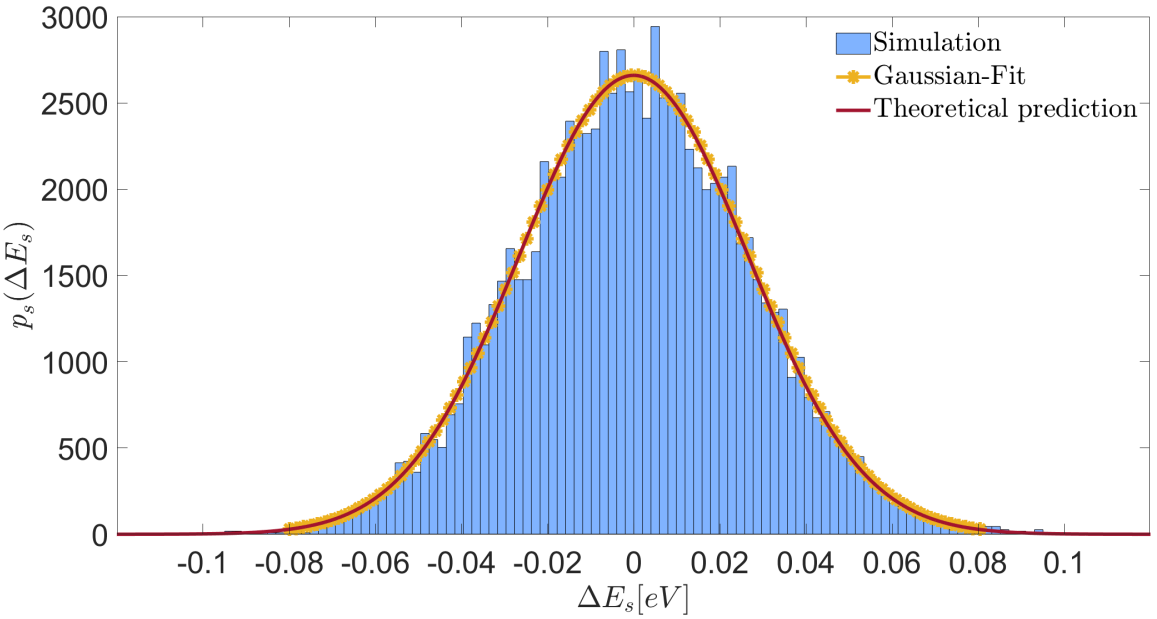

(a) Frequency distribution when $\theta_B = 75°$

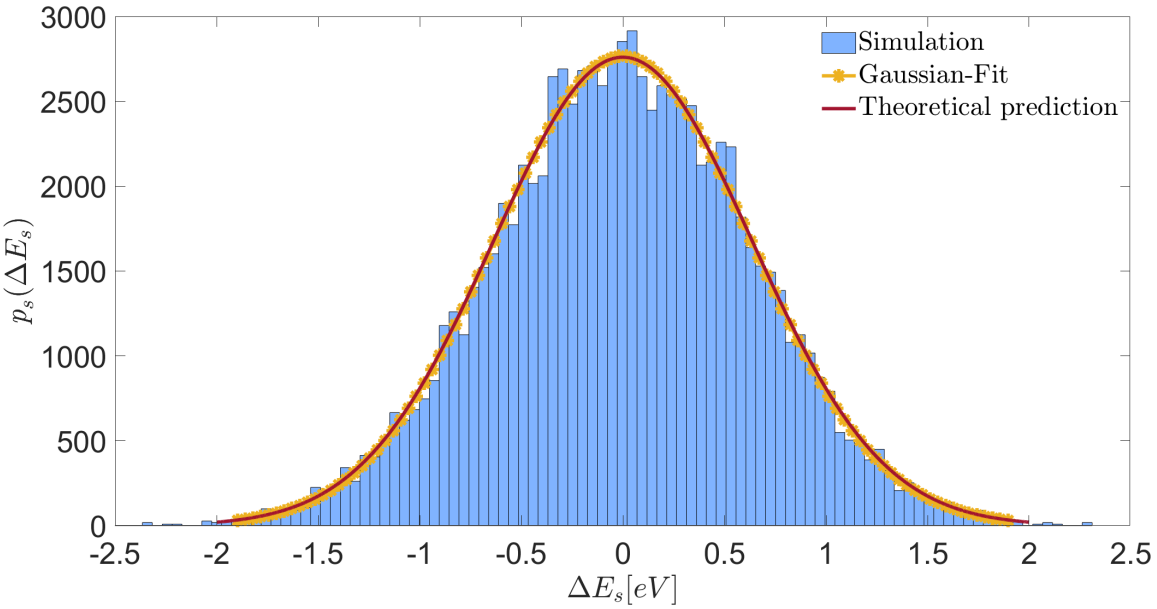

(b) Frequency distribution when $\theta_B = 30°$

Figure 5.8: Frequency distributions in the two extreme conditions ($\theta_B = 75°$ and $\theta_B = 30°$) simulated with a Gaussian source (FWHM 35×300 µm^2) and 90000 rays impinging in the centre of the crystal. Ge[220] reflections are here considered. In red the theoretical Gaussian. In yellow the Gaussian fits of the simulations.

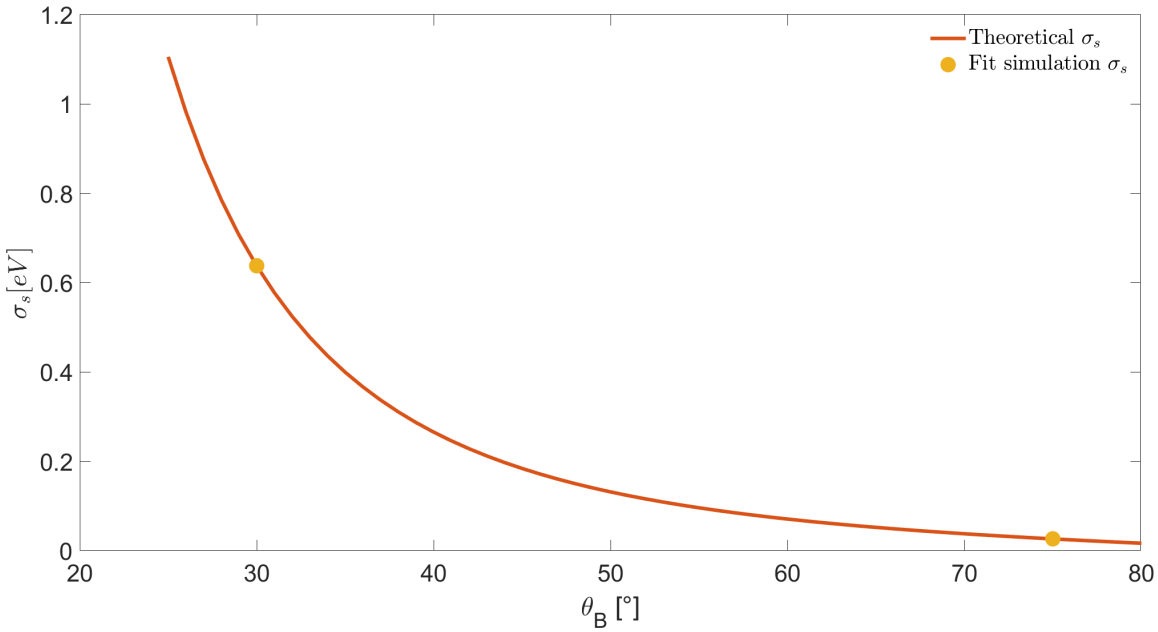

Figure 5.9: Theoretical standard deviation σ of the frequency distribution due to a Gaussian source with $\text{FWHM}_y = 35\,\mu\text{m}$ considering the Ge[220] reflections. Simulated results in the extreme cases are also reported as yellow dots.

In this first part of Chapter 5, simulations were extremely useful in order to validate analytical calculations made in Chapter 4. For this reason, up to now, simulations were carried out by decoupling the contributions deriving from the source and from the analyzer. Both sets of simulations show a perfect agreement with the respective probability distributions predicted by the theory (Equations 4.40 and 4.45) confirming our intellectual control on the geometric contributions to energy resolution of the spectrometer.
The next natural step is to simulate the overall geometric contribution to energy resolution (p_g) considering both an extended source and analyzer at the same time and comparing it with the theoretical result: as shown in Appendix C, in fact, the total angular deviation $\Delta\theta_g$ is given, as a first approximation, by:

$$\Delta\theta_g \simeq \Delta\theta_a + \Delta\theta_s$$

Since $\Delta\theta_a$ and $\Delta\theta_s$ are decoupled and independent, the overall theoretical probability distribution can be obtained by convolving the probability distributions of $\Delta\theta_a$ and $\Delta\theta_s$, that is

$$p_g(\Delta\theta) = \int p_a(\Delta\theta - \Delta\theta')p_s(\Delta\theta')d\Delta\theta'$$

5.3. Simulation of the total geometric contribution to energy resolution

To naturally conclude the long excursus regarding the geometric contribution of the spectrometer, this chapter reports the results of the simulations carried out considering both the effects of the source and of the analyzer at the same time i.e. the overall geometric resolution of the instrument. Particular attention should be paid to Figure 5.10: the left column refers to the simulations carried out considering all the correct parameters of the instrument, while the images on the right are the frequency distributions predicted by the theory. The theoretical curves are also superimposed to the simulated histograms in order to make the comparison easier: it is evident how the theory fits almost perfectly with the simulations although the first one do not include the effects due to the length of the analyzer. As small deviation can be observed in Figure 5.10a: the theory seems to provide a slight underestimation only on the right part of the overall distribution starting approximately from 0.16 eV. This effect is essentially due to the fact that the frequency distribution of the analyzer, represented in blue in the plot on the right (see Figure 5.10b), does not show the typical tail originating from the l-dependence (see Figure 5.4). This leads to an underestimation of the convolution, especially when the tail is weighted by the maximum of the Gaussian of the source (in green) i.e. when the relative shift between the two graphs is, not by chance, around 0.16 eV. The small effect due to the length of the crystal becomes even less significant at lower Bragg angles where, as seen, the tail should be more significant. The apparent contradiction is immediately solved noticing how, as the Bragg angle decreases, the source contribution becomes more and more dominant over the analyzer distribution (observe the panels on the right), effectively hiding any effect coming from the tail. To summarize we can say that even in the worst condition, the difference between the simulated frequency distribution and the analytical result obtained neglecting the l coordinate of the crystal is so small that an excellent estimate of the overall frequency distribution can be obtained simply by convolving, for each incidence angle, equation 5.1 with equation 5.4 *without the need to perform any simulation.*

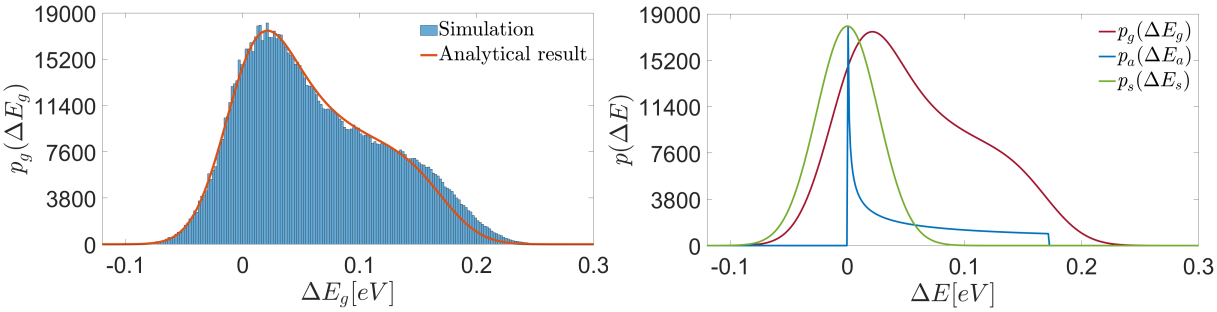

(a) Simulation at $\theta_B = 75°$

(b) Analytical distributions at $\theta_B = 75°$

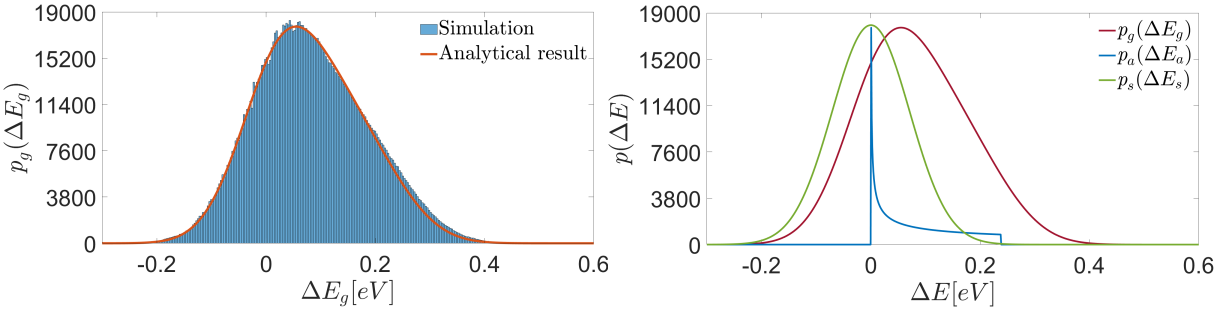

(c) Simulation at $\theta_B = 60°$

(d) Analytical distributions at $\theta_B = 60°$

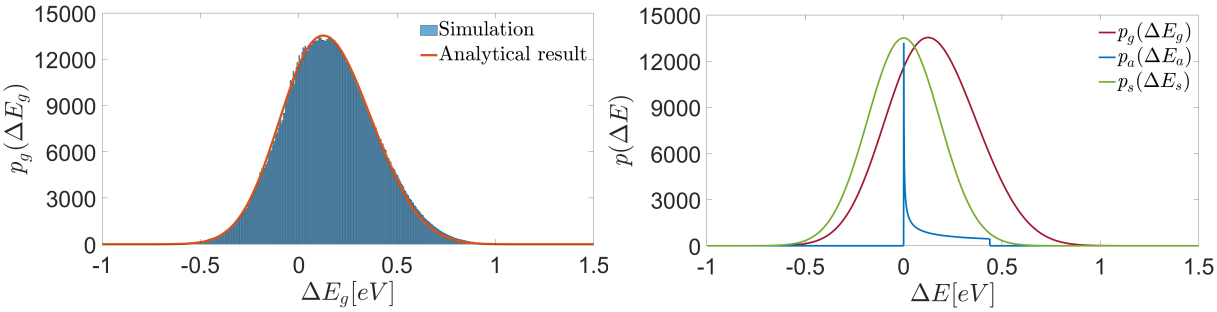

(e) Simulation at $\theta_B = 45°$

(f) Analytical distributions at $\theta_B = 45°$

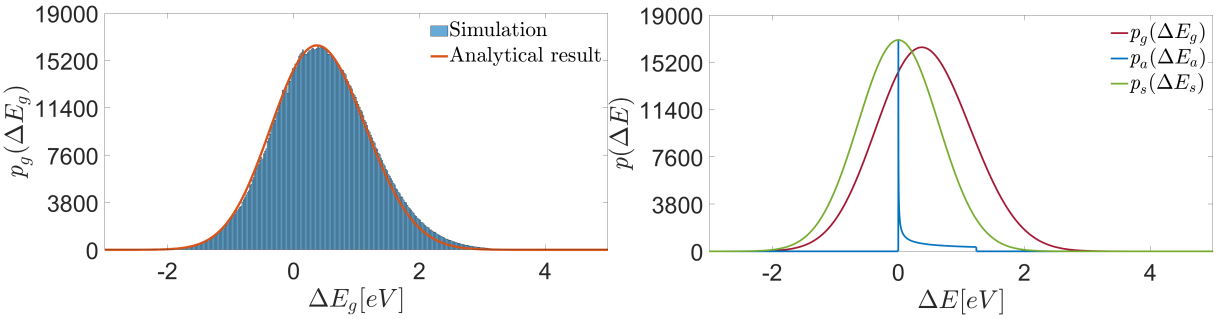

(g) Simulation at $\theta_B = 30°$

(h) Analytical distributions at $\theta_B = 30°$

Figure 5.10: On the left are reported the overall frequency distributions simulated at different θ_B considering a Gaussian source (FWHM 35×300 µm^2) with 2500 points arranged randomly and an analyzer of length $2L = 10$ cm and width $2Z = 1$ cm composed by 625 points. On the right the analytical frequency distributions p_s and p_a and their convolution p_g. The convolutions (red) are also superimposed to the simulated histograms.

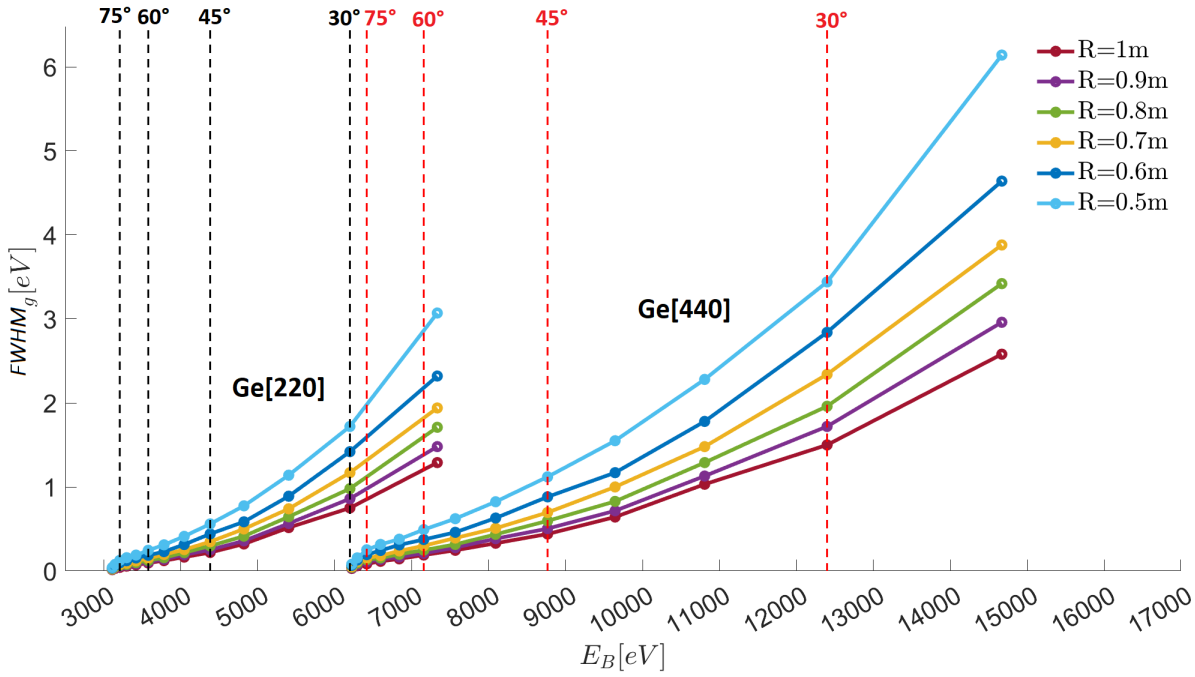

Figure 5.11: The FWHM of the total geometric contribution to energy resolution is here reported in function of the Bragg energy E_B. Both Ge[220] and Ge[440] reflections are considered. Different diameters of the Rowland circle are represented. With black dashed lines some Bragg angles of the Ge[220] reflections are reported. With red dashed lines some Bragg angles of the Ge[440] reflections are reported.

In Figure 5.11 the $FWHM_g$ of the overall geometric contribution to energy resolution as a function of the Bragg energy E_B are simulated for different spectrometer dimensions, considering both the Ge[220] and Ge[440] reflections. We could discuss the meaning of the $FWHM_g$ in an extremely asymmetrical graph like the one shown in Figure 5.10a: probably, for this particular shape it is not the most appropriate figure of merit; on the other hand, the energy resolution of the spectrometer is critical at low Bragg angles, where the distributions become really similar to a Gaussian.

The overall geometric contribution to energy resolution is reported in Figure 5.12 for a Ge[220] Johansson ($R = 50\,\text{cm}$) crystal of 10×1 cm^2 and considering a source with FWHM along the two axes respectively equal to 35 µm and 300 µm. The Ge[440] and Ge[660] reflections can be directly deduced from the multiple axes reported with different colors:

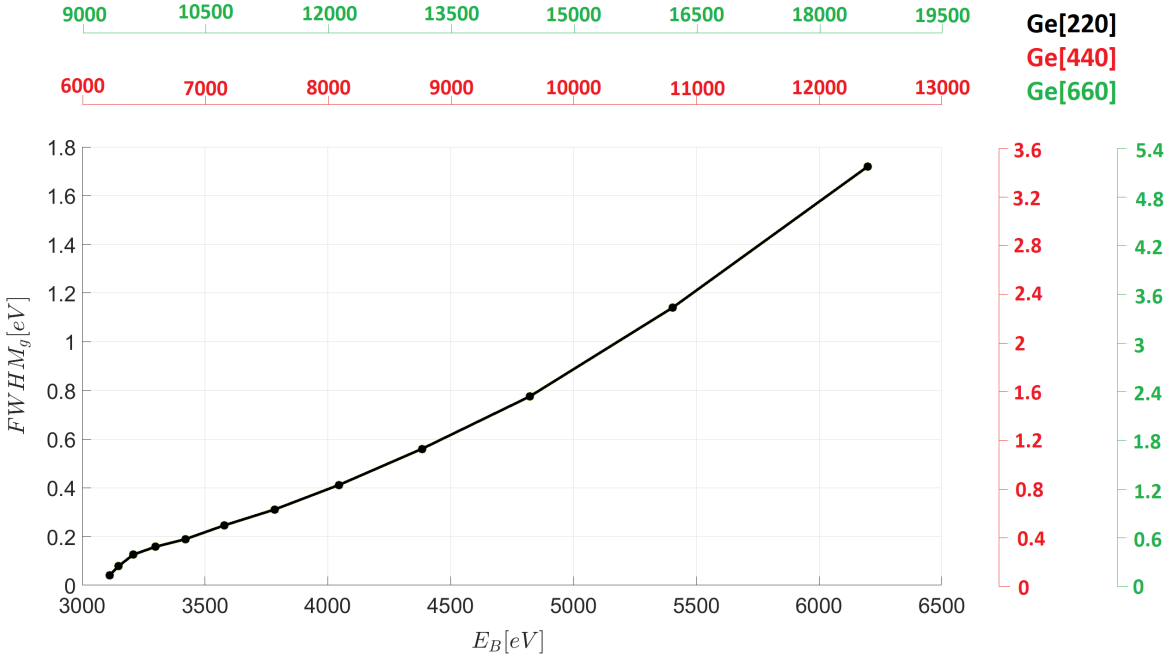

Figure 5.12: The FWHM of the total geometric contribution to energy resolution is here reported as a function of the Bragg energy E_B. The Ge[220], Ge[440] and Ge[660] reflection for a Johansson ($R = 50\,\text{cm}$) crystal of $10 \times 1\ \text{cm}^2$ surface and a Gaussian source of $35 \times 300\ \mu\text{m}^2$ ($FWHM^2$) are considered.

Thanks to the partial overlap between different reflections we can cover the entire energy spectrum from $E_B = 3\,\text{keV}$ up to $E_B = 14\,\text{keV}$ starting the scan at $\theta_B = 75^\circ$ considering the Ge[220] reflection. As can be seen from Figure 5.11 and Figure 5.12, reached an energy $E_B \simeq 6\,\text{keV}$ for the Ge[220] reflection with an incident angle $\theta_B \simeq 30^\circ$, it is possible to go back to the initial value $\theta_B = 75^\circ$ restarting the scan considering, this time, the Ge[440] reflection. Thanks to the partial overlap between different reflections is so possible to continuously cover a big energy interval. Following this approach it is possible to entirely cover the range $3 - 14$ keV keeping the total geometric resolution $FWHM_g$ below $2\,\text{eV}$. Nevertheless, as will be explained in Chapter 6, in order to consider the overall geometric resolution it will be necessary to take into account a further contribution to the energy resolution that, until now, I have never explicitly considered.

6 | Intrinsic contribution to energy resolution

Beside the geometric contribution described in the previous chapters, we need to consider the intrinsic energy resolution of the analyzer, whose origin can be traced in the dynamical theory of diffraction from bent crystals. Despite the relevance of this topic, this chapter does not aim to deal with it in depth for two reasons:

- the theory that will be presented is extremely complex and goes beyond the scope of this thesis work and probably my skills;
- the intrinsic contribution deriving from this theory can not be changed as its name suggest. It is an intrinsic property of the crystal that can not be adjusted, as the geometric contribution to energy resolution, by properly designing the instrument.

Nevertheless, including the intrinsic contribution is necessary. In section 6.1 the most important aspects of the theory will be mentioned while, in section 6.2, the results obtained through the simulations carried out with *tbcalc*, a software written to precisely describe the diffraction profile of a bent crystal, will be reported.

6.1. Dynamic theory of diffraction

6.1.1. From kinematic to dynamic theory of diffraction

The kinematic theory of diffraction is based on the assumption that, when the incident radiation penetrates inside the crystal, the magnitude of the X-ray wavefield does non change. In other words, in order to treat under this hypothesis the problem of diffraction we must be sure that the scattering can be considered to be weak. Starting from the kinematic theory it is possible to derive Bragg's law 3.6 and the unit cell structure factor (see section 3.1.2). However, a theory aiming at describing quantitatively the diffraction profile of a crystal should take into account the attenuation of the radiation field inside the crystal and the possibility of multiple scattering events. The theory that takes into

account all these aspects is known as *Dynamical Diffraction Theory* [9]. Before introducing the main results of the theory we can describe a simpler phenomenon (usually neglected in the derivation of Bragg's law). Even in the kinematical framework, indeed, a perfect crystal ideally composed by an infinite stack of layers presents a small shift from the peak positions predicted by Bragg's law 3.6.

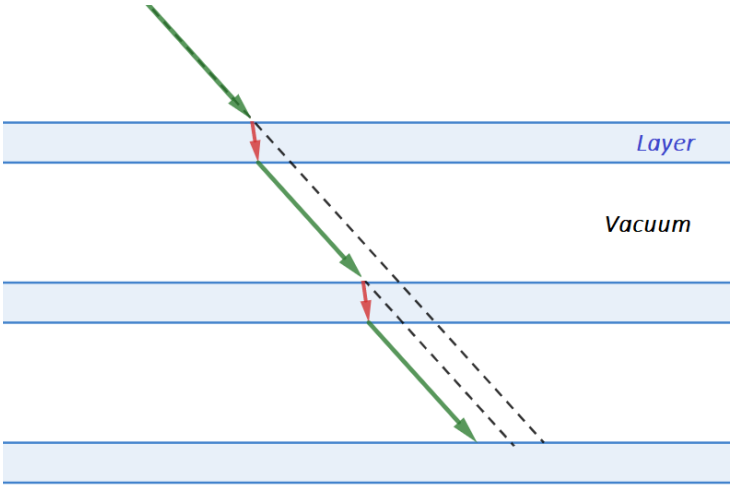

Figure 6.1: The difference between the refractive indices of the layers and of the spaces between them introduces a small phase shift not included in Bragg's law.

This effect is due to the difference between the refractive indices of the layers and of the space in between (see Figure 6.1). We can ask ourselves what happens around a Bragg reflection: to this purpose we can introduce the parameter ζ in order to map the reciprocal space:

$$\zeta = \frac{\Delta\lambda}{\lambda} = \frac{\Delta Q}{Q} \tag{6.1}$$

it means that Equation 3.9 can be rewritten including this new parameter ζ that allows us to probe the regions around a Bragg peak:

$$\boldsymbol{Q} = m\,\boldsymbol{G}(1+\zeta) \tag{6.2}$$

Summing all the reflections obtained by the infinite stack of crystallographic planes a reflectivity no longer centered on the Bragg peak is obtained: this shift is usually called ζ_0. Let us try to derive some characteristics of this parameter making qualitative reasonings: due to the fact that the refractive index, for X-rays, is less than unity, we can expect that the modulus of the wavevector inside the crystal layers is smaller than in the interstitial

regions [9]. For this reason, in order to have constructive interference we must have $|\boldsymbol{k}|$ outside larger than the value predicted by Bragg's law 3.6. Therefore we expect a reflectivity maximum displaced by a positive amount ($\zeta_0 > 0$) if compared with the value predicted by Bragg's law. As a first comment we can therefore say that Bragg's law must be "corrected" including this shift of the peaks. The reflectivity curve thus obtained is so peaked not at $\zeta = 0$ but at $\zeta = \zeta_0$. If we are sufficiently far from ζ_0 the kinematic theory (used up to now) can still be considered as a good approximation. As $|\zeta - \zeta_0| \to 0$ the kinematical approximation breaks down and the reflectivity must be described by dynamical theory. The aim of the dynamical theory of diffraction is to calculate the scattering from an infinite stack of atomic planes where each one reflects a fraction of the incident wave. The only parameter which I would like at least to mention is the *Darwin width*: if the Bragg's law implies that only a single energy is reflected for a given angle, an important result of dynamic theory is that the reflected beam has a finite bandwidth that is called Darwin width. Clearly, this enlargement causes a deterioration of the energy resolution that must be taken into account in order to well estimate the real behaviour of the spectrometer.

Dynamic theory for bent crystals

However, the theory just presented is not sufficient if we want to consider bent crystals. In this case, in fact, the local distance between crystallographic planes can no more be considered uniform due to the bending. In a pictorial view we can say that, because of the bending, there will not be a unique interatomic distance but a distribution of interatomic distances [10], which will cause a further broadening of the reflected energy. A simple explanation can be done saying that, in this conditions, Bragg's law is satisfied by a distribution of angles. Dynamic theory for bent crystals requires more complicated theories and different approximated approaches are usually followed [21]. In particular, software that are typically used to estimate this contribution are based on two of them:

- *Multilamellar method:*
  the strain inside the material is not considered and a bent crystal is modeled by several flat lamellae parallel to the crystal surface. Each lammella behaves as a flat crystal and reflects the radiation [10]. The superposition of the radiation reflected by each lammella gives the final result. This approach can be followed only if the crystal is sufficiently thick and with low curvature. This approach was introduced in [22] and implemented in the SHADOW package [23].

- *Takagi-Taupin theory:*
  Unfortunately, given the small curvature radius of our crystal, it is convenient to opt for a more accurate method, which also takes into account the internal stress of the material. We will therefore focus on the Takagi-Taupin approach, an optimum compromise of accuracy and relative simplicity. This method was developed independently by Satio Takagi [24] and Daniel Taupin [25]. Analytic solutions for the TT problem are known only for simple, unrealistic cases while, typically, solutions are found numerically [26]. We will follow the method developed by Ari-Pekka Honkanen in the Phyton program *tbcalc* (Toroidally Bent Crystal Analyzer Calculator) [27]. This is the program used in the following simulations in order to determine the intrinsic contribution to energy resolution.

6.2. The *tbcalc* simulations

Here the simulations carried out with *tbcalc* are reported. They show the line-shape of the reflectivity due to the intrinsic contribution of the bent crystal analyzer. This is the analogous, for the intrinsic contribution, of the geometric frequency distribution p_g calculated and simulated in Chapter 5. For this reason, we will call the reflectivity p_i.

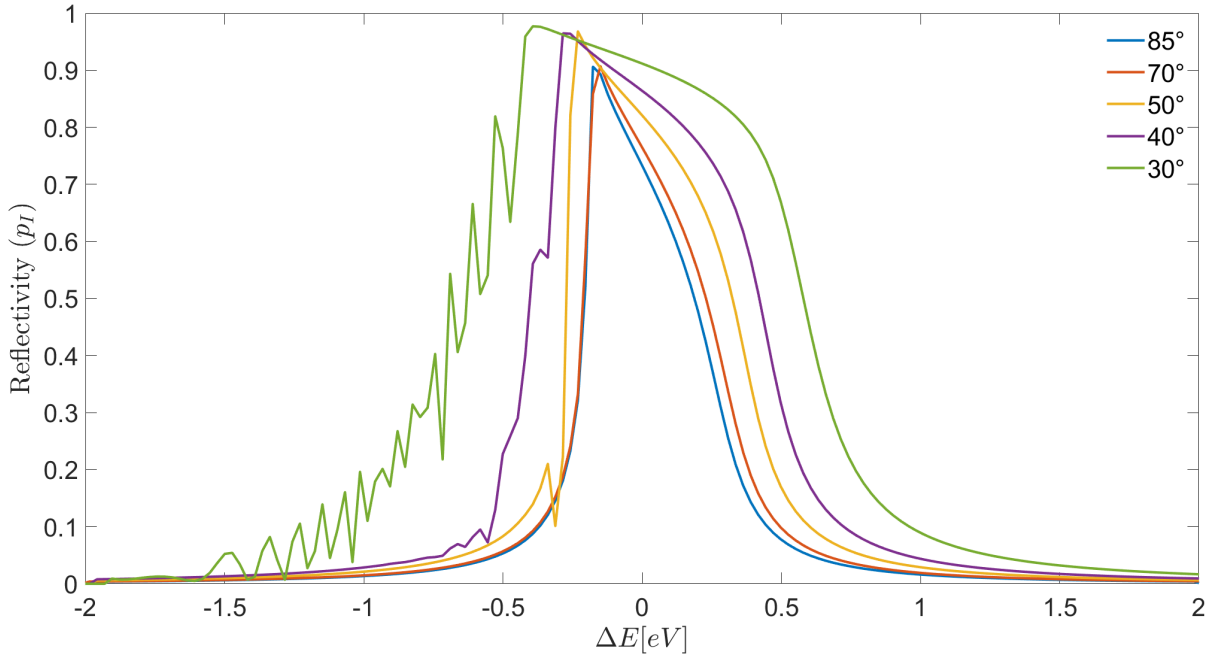

Figure 6.2: Intrinsic contribution to energy resolution for a cylindrically bent Ge[220] crystal. Curvature radius $R = 50\,\text{cm}$. Thickness $t = 0.35\,\text{mm}$. σ polarized light.

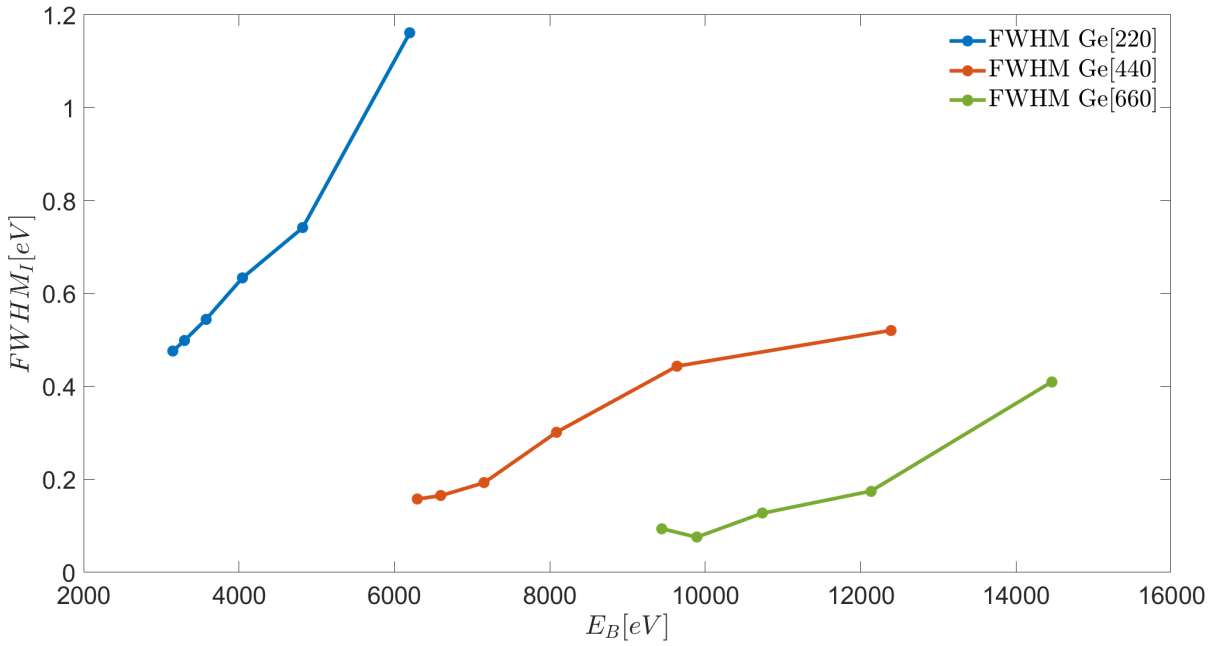

Figure 6.3: Intrinsic $FWHM_I$ evaluated by a Gaussian-fit. Ge[220], Ge[440] and Ge[660] reflections are considered. Curvature radius $R = 50\,\text{cm}$. Thickness $t = 0.35\,\text{mm}$. σ polarized light.

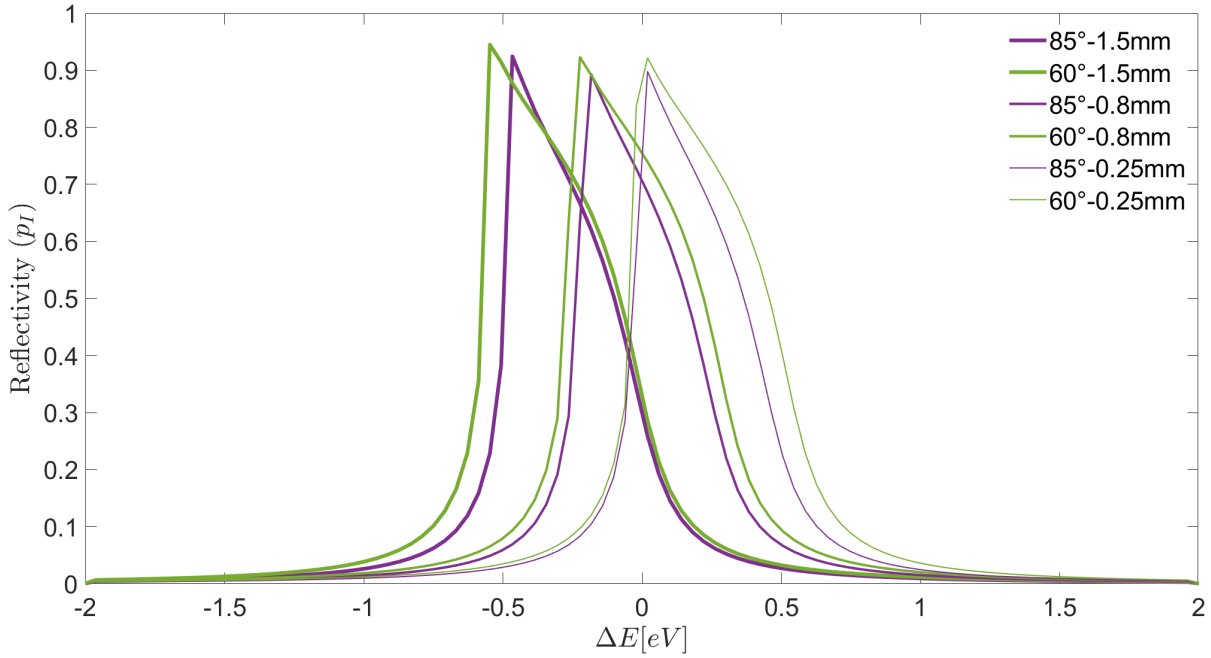

Figure 6.4: Intrinsic contribution to energy resolution for a cylindrically bent Ge[220] crystal. Curvature radius $R = 100$ cm. Variable crystal thicknesses t. σ polarized light.

Analogous simulations for Ge[440] and Ge[660] have been performed. Given that the shape of the curves can be acceptably approximated by a Gaussian (see Figure 6.2), in order to directly compare the geometric resolutions with the intrinsic ones, it was decided to carry out a Gaussian fit of *tbcalc* simulations extrapolating the $FWHM_I$ values that are reported in Figure 6.3. The intrinsic contribution to energy resolution is larger at small Bragg angles and, unlike what happens for the geometric contributions, it shrinks with increasing the order of the harmonics. The simulations were performed for a thickness $t = 350\,\mu m$, typical value for a bent crystal analyzer.
In Figure 6.4 we show the effect of crystal thickness: the diffraction profile shifts with t, but it does not change its width. This effects should be investigated further because, if confirmed, will be relevant for Johansson-type crystals which do not have a constant thickness.

7 | Final Remarks

7.1. Overall energy resolution

After calculating all contributions separately, we can reasonably estimate the overall energy resolution of the spectrometer. To construct the overall energy distribution we should convolve equation 4.47 with the curves shown in Figure 6.2:

$$p_{tot}(\Delta\theta) = \int p_g(\Delta\theta - \Delta\theta')p_i(\Delta\theta')d\Delta\theta' \tag{7.1}$$

However, an immediate result can be obtained if $p_g(\Delta E)$ and $p_i(\Delta E)$ can be approximated by gaussian functions:

$$FWHM_{tot} = \sqrt{FWHM_g^2 + FWHM_i^2} \tag{7.2}$$

The final results are plotted in Figure 7.1: as can be seen, for Ge[440] considering the reflections at high θ_B (up to 8 keV), the total resolution is better than for Ge[220]. It is due to the fact that, in this region the intrinsic contribution dominates. On the contrary, at grazing incidence is the geometric contribution the dominant component and, for this reason, Ge[220] shows a better energy resolution in the low Bragg regime.
The combination of the above effects allows us to make good use of the reflection Ge[440] up to $E_B = 10$ keV where the total $FWHM$ is around 1.7 eV. Starting from this energy, thanks to the overlap with the Ge[660] reflection, it is possible to continue the scan keeping the resolution below 2 eV up to E_B =13.5 keV. The weak point of the whole scan is paradoxically around E_B =6 keV where we must reach $\theta_B = 29°$ in order to reach the overlap with the Ge[440] reflection at $\theta_B = 75°$.

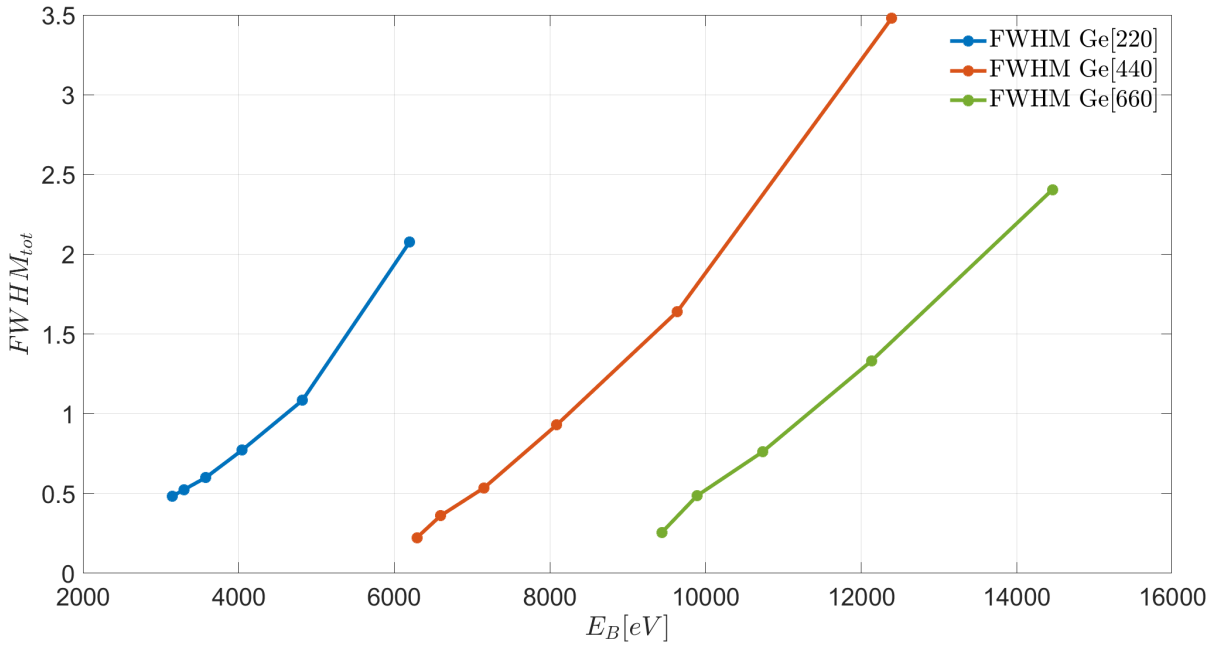

Figure 7.1: $FWHM_{tot}$ of the overall energy resolution of the spectrometer. The $FWHM_{tot}$ are estimated summing the squares of the geometric $FWHM_g$ and of the intrinsic $FWHM_I$.

7.2. Estimation of the scanning time

As reported by Seidler et all.[28] at least 10^5 photons per measurement point will be needed to cleanly resolve the XAS spectrum: considering a mean value of the specific spectral radiant intensity of the Incoatec source obtainable from spectra reported in section 2.2.1

$$I_W^{mean} \simeq 4 \cdot 10^5 \left[\frac{photons}{sr \cdot eV \cdot W \cdot s}\right]$$

and considering that, the maximum power achievable fixing the tube voltage at 20 kV is 13 W the following mean spectral radiant intensity is expected.

$$I^{mean} \simeq 5 \cdot 10^6 \left[\frac{photons}{sr \cdot eV \cdot s}\right]$$

Considering a solid angle identified by an analyzer of area $A = 10\,\mathrm{cm}^2$ at a distance $d \simeq 50\,\mathrm{cm}$ from the source

$$\Omega = \frac{A}{d^2} \simeq \frac{1}{250}$$

considering a FWHM of the passing bandwidth around 1 eV and an ideal absorbing factor of $1/e$ we obtain a number of photons per unit time on the detector equal to

$$7.5 \cdot 10^3 \left[\frac{photons}{s}\right]$$

so we must measure each experimental point for 14 s in order to collect 10^5 photons.

Considering 1000 points in order to cover the entire energy spectrum less than 4 hours are needed in order to complete the energy scan.

8 | Conclusions and future developments

We designed a user-friendly laboratory XAS spectrometer covering the $3-15$ keV energy range with an energy resolution below 3 eV aiming at limiting its costs and minimizing its dimensions. An in-depth study on the geometry of monochromators was carried out, combining an analytical approach with ray tracing simulations. Thanks to this complementary view it was possible to highlight the effects that geometric parameters have on the resolving properties of the instrument, enabling us to maximize the ratio between performance and costs. We selected a Johansson-type cylindrically bent analyzer with curvature radius $R = 50$ cm and dimensions 10×1 cm^2 exploiting also the reflections of the first and second harmonics of Ge[220]. The possibility of building a spectrometer capable of covering such a wide energy range with a single crystal is certainly a remarkable result and in line with the idea of designing an instrument that is easy to use and does not require frequent alignments which would have been necessary using more crystals. This result is the consequence of two important choices: first of all to have selected a Johansson-type crystal, thus allowing us to reach incidence angles unthinkable for a Johann crystal; secondly, to have chosen a family of crystallographic planes (Ge[220]) for which also the first and second harmonic reflections are allowed. The simulations show that at low Bragg angles the contribution deriving from the extension of the source dominates over that of the analyser. This information underlines how, despite the limitations imposed by the use of a single crystal, the weak point of the instrument is actually the source. As shown in the previous work carried out in the PoliMiX group [10], the choice of a Johann-type crystal would always lead to an enormous prevalence of Johann's aberrations over the effects generated by the extension of the source. At this point we can say with certainty that, in order to improve the resolution of the instrument, it would be necessary to mainly act on the focal dimensions of the source. We have therefore been able to move the bottleneck of the instrument from the analyzer to a parameter that cannot be directly modified by us. The design will soon be completed and will be followed by the purchase of the necessary pieces and the subsequent construction of the instrument.

Bibliography

[1] Diamond. Why choose x-ray absorption spectroscopy?

[2] Diego Gianolio. How to start an xas experiment. *X-Ray Absorption and X-Ray Emission Spectroscopy: Theory and Applications*, 1, 2016.

[3] Rene Bès, Taru Ahopelto, A-P Honkanen, S Huotari, G Leinders, Janne Pakarinen, and K Kvashnina. Laboratory-scale x-ray absorption spectroscopy approach for actinide research: Experiment at the uranium l3-edge. *Journal of Nuclear Materials*, 507:50–53, 2018.

[4] Giulia De Francesco. Wilhelm conrad röntgen, 2020.

[5] Incoatec. Incoatec microfocus x-ray source, 2011.

[6] Mauro Rovezzi, Alistair Harris, Blanka Detlefs, Timothy Bohdan, Artem Svyazhin, Alessandro Santambrogio, David Degler, Rafal Baran, Benjamin Reynier, Pedro Noguera Crespo, et al. Texs: in-vacuum tender x-ray emission spectrometer with 11 johansson crystal analyzers. *Journal of synchrotron radiation*, 27(3):813–826, 2020.

[7] Photodiode Array Detector. Photodiode array detector, 2011.

[8] Patric Zimmermann, Sergey Peredkov, Paula Macarena Abdala, Serena DeBeer, Moniek Tromp, Christoph Müller, and Jeroen A van Bokhoven. Modern x-ray spectroscopy: Xas and xes in the laboratory. *Coordination Chemistry Reviews*, 423:213466, 2020.

[9] Des McMorrow and Jens Als-Nielsen. *Elements of modern X-ray physics*. John Wiley & Sons, 2011.

[10] Matteo Corti. Preliminary design of a laboratory instrument for x-ray absorption spectroscopy. 2021.

[11] Dale E Sayers, Edward A Stern, and Farrel W Lytle. New technique for investigating noncrystalline structures: Fourier analysis of the extended x-ray—absorption fine structure. *Physical review letters*, 27(18):1204, 1971.

[12] Neil W Ashcroft and N David Mermin. *Solid state physics*. Cengage Learning, 2022.

[13] Ezio Puppin. Appunti delle lezioni fisica dei solidi. Politecnico di Milano, 2019.

[14] J Witz. Focusing monochromators. *Acta Crystallographica Section A: Crystal Physics, Diffraction, Theoretical and General Crystallography*, 25(1):30–42, 1969.

[15] R Caciuffo, S Melone, F Rustichelli, and A Boeuf. Monochromators for x-ray synchrotron radiation. *Physics Reports*, 152(1):1–71, 1987.

[16] Manuel Sanchez del Rio. Ray tracing simulations for crystal optics. In *Crystal and Multilayer Optics*, volume 3448, pages 230–245. SPIE, 1998.

[17] Hans Heinrich Johann. Die erzeugung lichtstarker röntgenspektren mit hilfe von konkavkristallen. *Zeitschrift für Physik*, 69(3):185–206, 1931.

[18] Tryggve Johansson. Selektive fokussierung der röntgenstrahlen. *The Science of Nature*, 20(41):758–759, 1932.

[19] M Moretti Sala, K Martel, C Henriquet, A Al Zein, L Simonelli, C Sahle, H Gonzalez, M-C Lagier, C Ponchut, S Huotari, et al. A high-energy-resolution resonant inelastic x-ray scattering spectrometer at id20 of the european synchrotron radiation facility. *Journal of synchrotron radiation*, 25(2):580–591, 2018.

[20] M Stepanenko. A spectral resolution of johann-type x-ray spectrometers. *Plasma devices and Operations*, 17(3):191–200, 2009.

[21] Jürgen Härtwig. Hierarchy of dynamical theories of x-ray diffraction for deformed and perfect crystals. *Journal of Physics D: Applied Physics*, 34(10A):A70, 2001.

[22] James Edward White. X-ray diffraction by elastically deformed crystals. *Journal of Applied Physics*, 21(9):855–859, 1950.

[23] Manuel Sanchez del Rio, Nicolas Perez-Bocanegra, Xianbo Shi, Veijo Honkimäki, and Lin Zhang. Simulation of x-ray diffraction profiles for bent anisotropic crystals. *Journal of Applied Crystallography*, 48(2):477–491, 2015.

[24] Satio Takagi. A dynamical theory of diffraction for a distorted crystal. *Journal of the Physical Society of Japan*, 26(5):1239–1253, 1969.

[25] Daniel Taupin. Théorie dynamique de la diffraction des rayons x par les cristaux déformés. *Bulletin de Minéralogie*, 87(4):469–511, 1964.

[26] RL Varner, WJ Thompson, TL McAbee, EJ Ludwig, et al. J. gronkowski. propagation of x-rays in distorted crystals under dynamical diffraction.

[27] A-P Honkanen and Simo Huotari. General method to calculate the elastic deformation and x-ray diffraction properties of bent crystal wafers. *IUCrJ*, 8(1):102–115, 2021.

[28] GT Seidler, DR Mortensen, AJ Remesnik, JI Pacold, NA Ball, N Barry, M Styczinski, and OR Hoidn. A laboratory-based hard x-ray monochromator for high-resolution x-ray emission spectroscopy and x-ray absorption near edge structure measurements. *Review of Scientific Instruments*, 85(11):113906, 2014.

[29] F Zagar. Alcune considerazioni sulla distribuzione della somma o differenza di due variabili aleatorie. *Memorie della Societa Astronomica Italiana*, 10:37, 1936.

A | The Atomic form factor

The purpose of this Appendix is to introduce fundamental aspects regarding the interaction of X-rays with matter [9]. Following an entirely classical approach, this will help us to deeply understand the working principle of a Bragg crystal used as a monochromator.

A.1. X-rays interacting with an electron

Classically, a charged particle hit by a plane wave reacts by oscillating in the direction of the electric polarization of the incident wave. The oscillating charge will emit a spherical wave with the same wavelength as the incident radiation. This is imposed by the classical treatment which makes the derivation of inelastic scattering impossible. Fortunately this phenomenon is typically negligible making the classical approximation often acceptable. The amplitude of the spherical wave will not be constant on the wave front: in fact, a general observer will appreciate only the projection of the electron acceleration perpendicular to the observation direction, that is equivalent to the real one only if the observer is placed in front (Ψ=90°) of the oscillating electron (see Figure A.1).
Let us therefore consider the electric field generated by a monochromatic plane wave in proximity of the charged particle:

$$\boldsymbol{E_{inc}}(t) = \boldsymbol{E_0} \exp(-i\omega t) \tag{A.1}$$

where ω is the angular frequency of the incoming wave. Remembering that, for the outgoing spherical wave the field is inversely proportional to the distance from the emitter ($|\boldsymbol{R}|$)[1] we can easily derive the following proportionality:

$$\boldsymbol{E_{rad}}(R,t) \propto \frac{-e\,\boldsymbol{a}(t')}{|\boldsymbol{R}|} \sin\Psi \tag{A.2}$$

[1] In fact, the intensity of a plane wave, which is proportional to the square modulus of the field, decreases quadratically with distance.

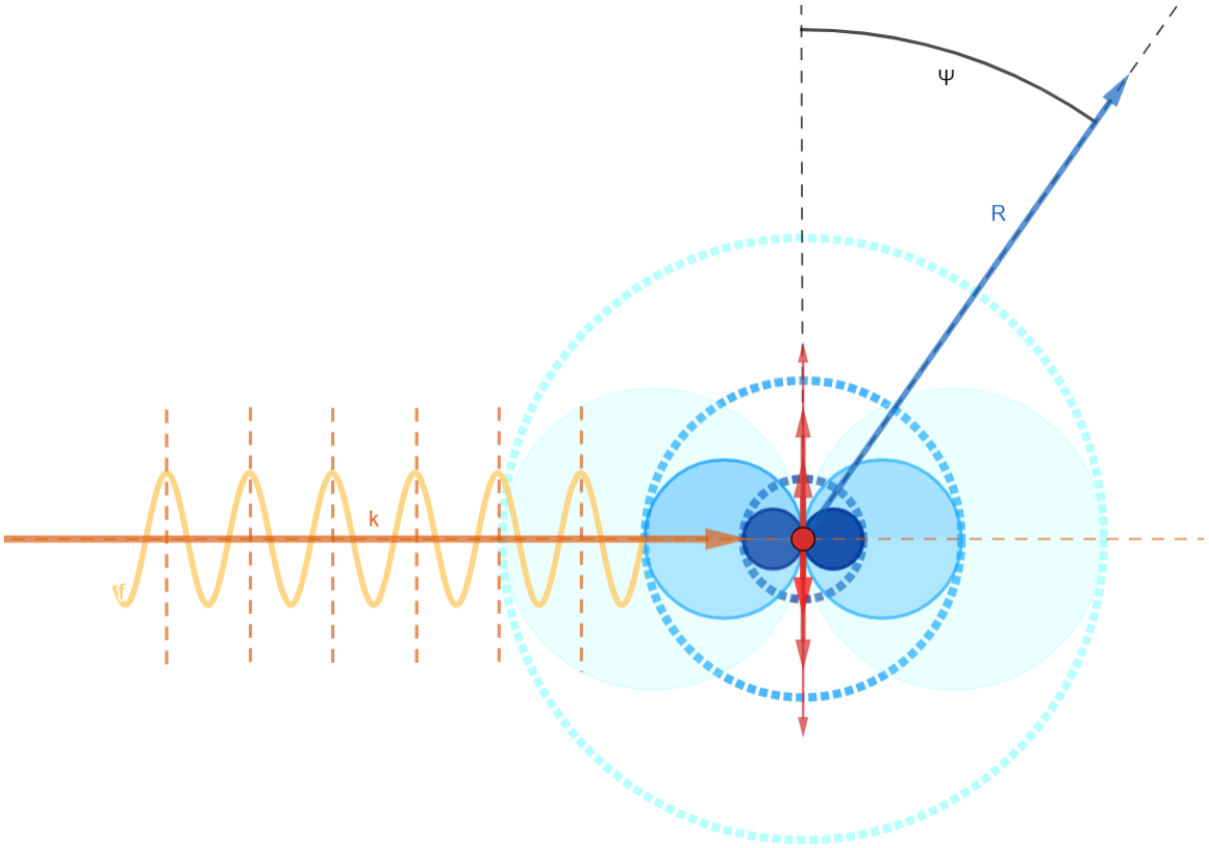

Figure A.1: An incoming plane wave (orange) scattered by a charged particle (red). The particle starts oscillating emitting a spherical wave. The front waves are represented in dashed lines. The amplitude of the spherical wave is modulated by a $\sin\Psi$ factor.

where $\boldsymbol{a}$ is the acceleration of the charged particle, Ψ is the angle that the observation direction makes with the oscillating direction and $t' = t - \frac{R}{c}$ since the observer sees with a certain delay the acceleration of the charged particle. It is due to the finite speed c of light. It is important to underline how, considering an atom, a free electron model can be adopted if the energy of the incident photon is much larger than the binding energy of the electrons. Considering a photon with typical energy of the order of 1 keV, this will certainly be true for valence electrons, less so for core ones. Assuming reasonable the free particle approximation, the acceleration acting on the charged particle (from now on we will refer more explicitly to an electron) and evaluated in t' is:

$$\boldsymbol{a}(t') = \frac{\boldsymbol{F}}{m} = \frac{-e\,\boldsymbol{E_0}\exp\left(-i\omega t'\right)}{m} = \frac{-e\,\boldsymbol{E_0}\exp\left(-i\omega t\right)\exp\left(i\frac{\omega R}{c}\right)}{m} = \frac{-e\,\boldsymbol{E_{in}}\exp\left(i\frac{\omega R}{c}\right)}{m} \tag{A.3}$$

Therefore, by expressing the ratio between the scattered electric field and the incident electric field, the following proportionality will be obtained:

$$\frac{E_{rad}(R,t)}{E_{in}} \propto \left(\frac{e^2}{m}\right) \frac{\exp(ikR)}{R} \sin\Psi \tag{A.4}$$

In order to transform the relation thus obtained into an equality it will be at least necessary to make the second member dimensionless: to do this, the term in round brackets must have the dimensions of a length. From a rigorous treatment we can obtain that the correct length can be obtained simply by equaling the Coulomb energy with the energy at rest of the electron itself. The typical length so obtained is called *Thomson scattering length* and classically represents the radius of the electron. By replacing this coefficient in relation A.4:

$$\frac{E_{rad}(R,t)}{E_{in}} = -\left(\frac{e^2}{4\pi\epsilon_0 mc^2}\right) \frac{\exp(ikR)}{R} \sin\Psi = -r_0 \frac{\exp(ikR)}{R} \sin\Psi \tag{A.5}$$

where a $(-)$ sign has been included in order to take into account the π phase shift between the scattered and incident waves.

A.2. X-rays interacting with an atom

An atom can easily be described by its electron density $\rho(\boldsymbol{r})$. We can imagine that each electron belonging to this distribution contributes by emitting a spherical wave as seen above. The phase shift between waves emitted by two electrons placed at a relative distance $\boldsymbol{r}$ is $\Delta\phi(\boldsymbol{r}) = \boldsymbol{Q}\cdot\boldsymbol{r}$ where we can define $\boldsymbol{Q}$ as the transferred wave-vector:

$$\boldsymbol{Q} = \boldsymbol{k} - \boldsymbol{k}' \tag{A.6}$$

For a given volume $d\boldsymbol{r}$ placed at a distance $\boldsymbol{r}$ from the origin, it is clear how the ratio E_{rad}/E_{in} will be proportional to the number of electrons contained in $d\boldsymbol{r}$ with a dephasing factor given by $\exp(i\boldsymbol{Q}\cdot\boldsymbol{r})$:

$$\frac{E_{rad}(R,t)}{E_{in}} \propto -r_0\, f^0(\boldsymbol{Q}) = -r_0 \int \rho(\boldsymbol{r}) \exp(i\boldsymbol{Q}\cdot\boldsymbol{r}) d\boldsymbol{r} \tag{A.7}$$

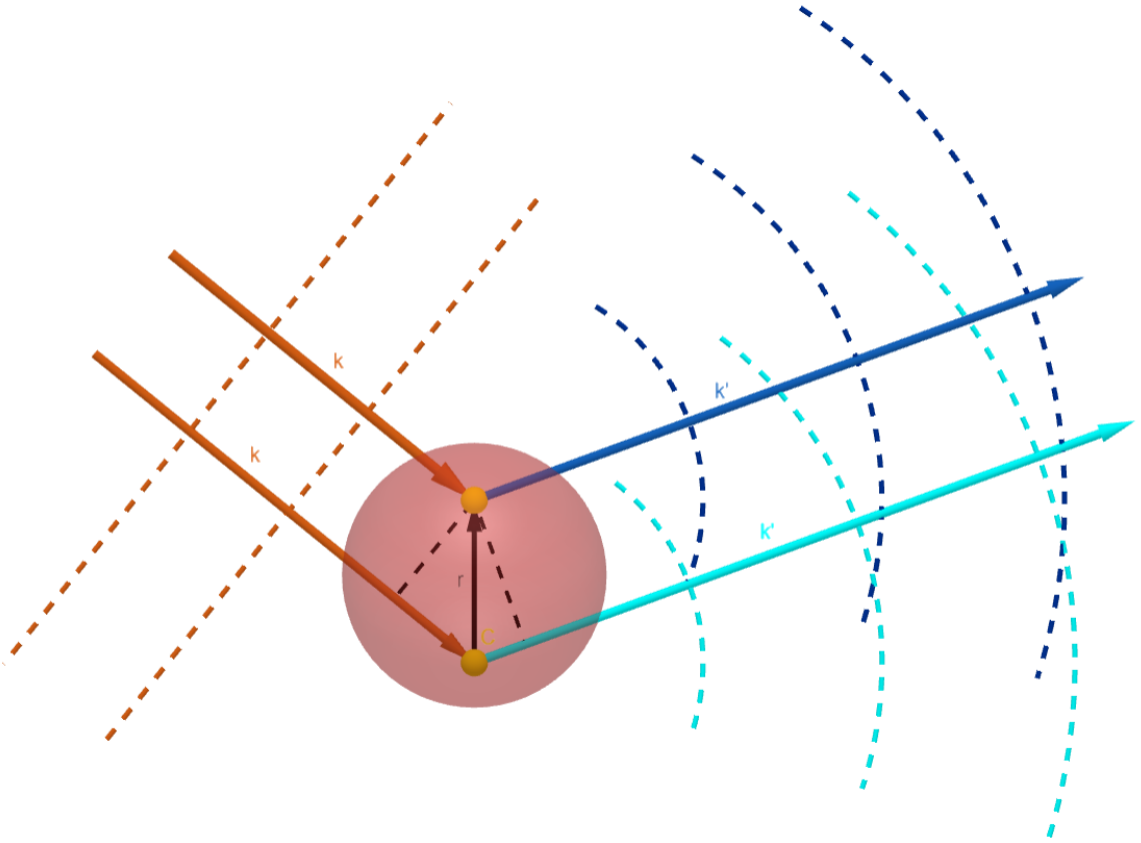

Figure A.2: An incoming plane wave (orange) scattered by two electrons (yellow) belonging to an electron distribution $\rho(\boldsymbol{r})$ (red). The electrons start emitting two spherical waves with phase shift $\Delta\phi(\boldsymbol{r})$. The front waves are represented in dashed lines. If the observer is far enough, the spherical fronts can be approximated by planes.

where $f^0(Q)$ is known as the *atomic form factor*[2]. If $\boldsymbol{Q} = 0$ i.e. if the electrons of all the different volume elements scatter in phase the reasonable result is obtained:

$$f^0(\boldsymbol{Q}) = \int \rho(\boldsymbol{r}) d\boldsymbol{r} = Z \tag{A.8}$$

As $\boldsymbol{Q}$ increases, the electrons contained in each small volume $d\boldsymbol{r}$ start to interfere more and more out of phase, decreasing the *atomic form factor*[3].

[2]Note how this parameter is nothing but the Fourier transform of the electron density.

[3]Corrective terms can be added taking into account that electrons within an atom are not free particles. These additional terms will become more important as the energy of the incident radiation decreases.

B | Sum of two independent random variables

In mathematics, and in particular in probability theory, a random variable (also called stochastic variable) is a variable that can take on different values depending on some random phenomenon. For example, the result of rolling a six-sided balanced die can be mathematically modeled as a random variable that can take one of six possible values with a 1/6 probability of occurring. A relative frequency function (probability density) can be associated with each random variable. Let x and y be two random *independent* variables and let X and Y be the associated frequency functions. By definition of probability it must hold:

$$\int_{-\infty}^{+\infty} X(x)dx = 1 \qquad \int_{-\infty}^{+\infty} Y(y)dy = 1. \tag{B.1}$$

If we define the random variable $z = x+y$, its relative frequency function Z can be written as the convolution of the two frequency function X and Y:

$$Z(z) = X \circledast Y = \int_{-\infty}^{+\infty} X(x)Y(z-x)dx \tag{B.2}$$

Let's briefly discuss an example to clarify what has been said. We define the random variables in the following way:

- x: value obtained from the first roll of a die;
- y: value obtained from the second roll of the die;
- $z = x + y$: value obtained by adding the results of the two launches.

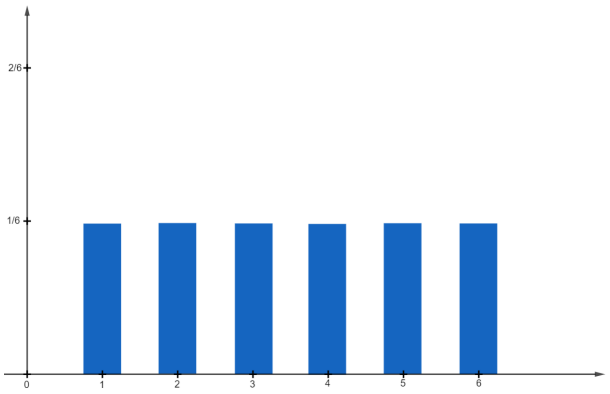

(a) Relative frequency function $X(x) = Y(y)$.

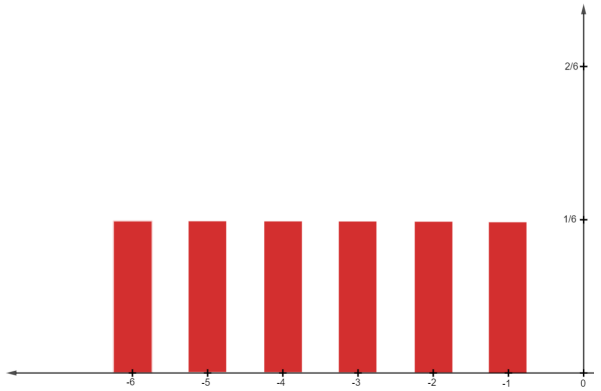

(b) Y(-x) represented in order to visualize the convolution.

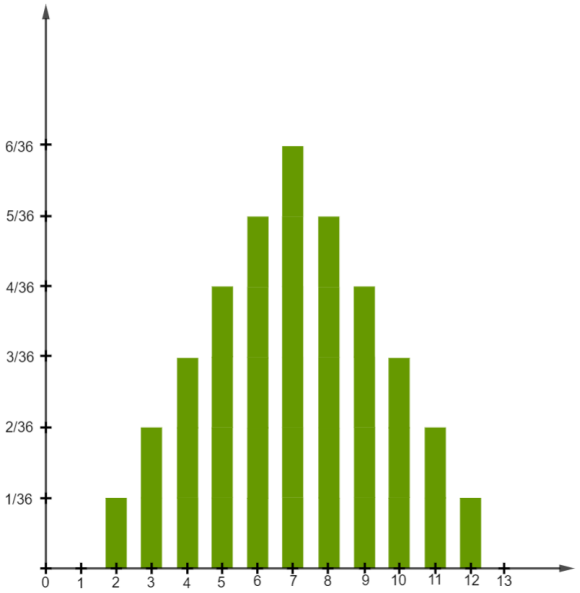

(c) Z(z) is the result of the convolution.

Figure B.1: Graphical representation of the Relative frequency function.

The relative frequency function related to x and y is trivial: each face of the die has in fact the same probability $\frac{1}{6}$ of coming out as shown in Figure B.1a. The result of the convolution is shown in Figure B.1c. It is easy to realize how this graph represents the frequency function relative to the random variable z.
It is of fundamental importance to underline once again how this procedure is correct only if *the random variables to be added are independent* [29].

C | Total geometric resolution

In this paragraph, unlike what has been done in Chapter 4, we will consider at the same time the contributions of the source and the analyzer. In doing so, we will take into account only the main[1] coordinates (s_y for the source and z for the crystal).

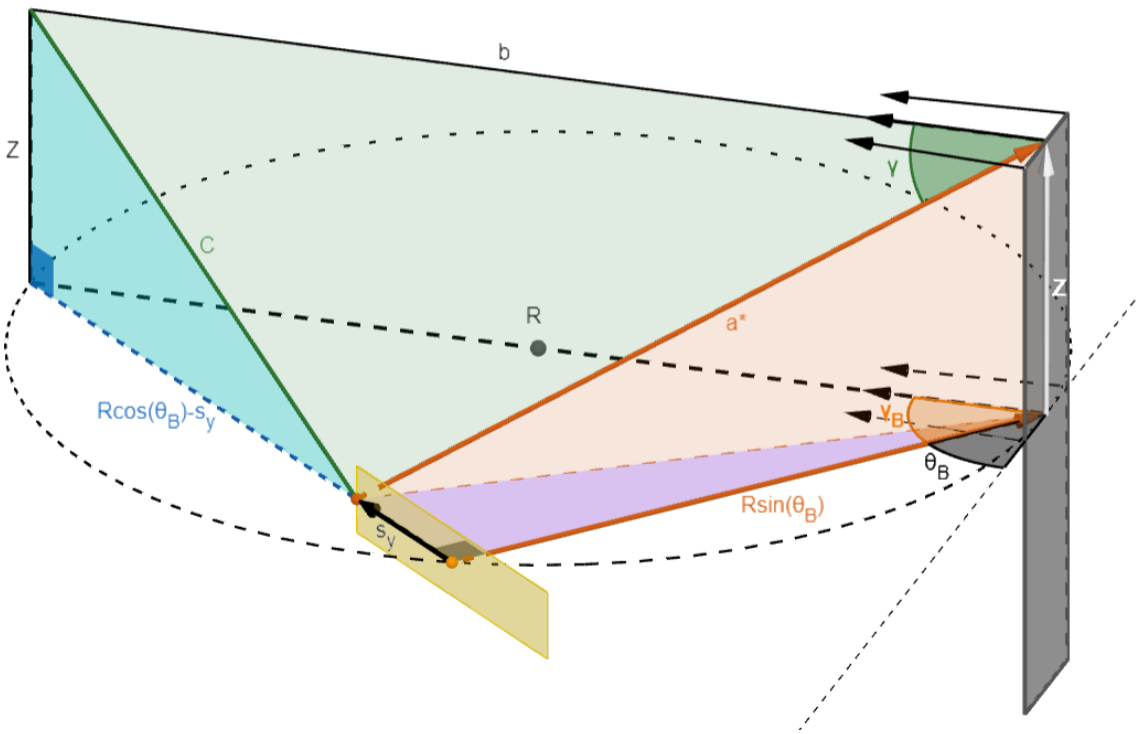

Figure C.1: 3D view of two rays (a and a^*). a is the nominal ray (starting from the center of the source and incident in the center of the crystal). a^* is a generic ray (starting from the coordinate s_y of the source and incident in the coordinate z of the crystal). Additional geometric elements are represented for the sole purpose of supporting the reader in the calculations.

[1]It was demonstrated in Chapter 4 how the coordinates l and s_z give a second order contribution.

Supported by Figure C.1 and using the Pythagorean theorem, the sides of the green triangle are obtained:

$$\begin{cases} a^* = \sqrt{R^2 \sin^2\theta_B + s_y^2 + z^2}, & \text{(C.1a)} \\ b = R, & \text{(C.1b)} \\ c = \sqrt{(R\cos\theta_B - s_y)^2 + z^2}, & \text{(C.1c)} \end{cases}$$

Using the cosine theorem on this triangle and exploiting the relation $\cos\gamma = \sin\theta$

$$\sin\theta = \frac{(a^*)^2 + b^2 - c^2}{2a^* b} \tag{C.2}$$

Substituting system C.1 in equation C.2:

$$\sin\theta = \frac{2R^2\sin^2\theta_B + 2Rs_y\cos\theta_B}{2R^2\sin\theta_B\sqrt{1 + \frac{s_y^2+z^2}{R^2\sin^2\theta_B}}} \tag{C.3}$$

expanding the square root:

$$\sin\theta\left(1 + \frac{s_y^2 + z^2}{2R^2\sin^2\theta_B}\right) = \sin\theta_B + \frac{s_y\cos\theta_B}{R\sin\theta_B} \tag{C.4}$$

and consequently

$$\sin\theta_B - \sin\theta \simeq \cos\theta\Delta\theta_g = \sin\theta\left(\frac{s_y^2 + z^2}{2R^2\sin^2\theta}\right) - \frac{s_y}{R\tan\theta} \tag{C.5}$$

it comes that:

$$\Delta\theta_g = \tan\theta_B\left(\frac{z^2}{2R^2\sin^2\theta}\right) + \tan\theta_B\left(\frac{s_y^2}{2R^2\sin^2\theta}\right) - \frac{s_y}{R\sin\theta_B} \simeq \Delta\theta_a + \Delta\theta_s \tag{C.6}$$

that is exactly the sum of equation 4.24 and equation 4.34. This apparently redundant result actually adds a lot to the knowledge of our system: in fact, considering the two contributions together, we could have expected the presence of new terms with mixed variables. This result, otherwise, unequivocally demonstrates how, with these approximations, we can really say that to find the total geometric contribution to energy resolution

$\Delta\theta_g$ we simply need to sum the two contributions ($\Delta\theta_a$ and $\Delta\theta_s$) taken separately. On the other hand we know that the two contributions are independent: in fact, knowing where a ray hits the analyzer (i.e, $\Delta\theta_a$) does not change our knowledge regarding the starting point of the same ray (i.e, $\Delta\theta_s$).
Resuming we are interested into the sum of two independent random variables and, consequently, it is legitimate to convolve the frequency distributions ($p_a(\Delta\theta_a)$ and $p_s(\Delta\theta_s)$) in order to find $p_g(\Delta\theta_g)$ (see Appendix B).
This observation could lose its validity when also the l coordinate of the crystal is taken into account. Despite this, l has a decidedly negligible impact on the resolution of the spectrometer, especially at high Bragg angles. This authorizes us to neglect this term and to sum (convolve) the two contributions (frequency distributions) as confirmed by simulations reported in Chapter 5.

List of Figures

Acknowledgements

A special thanks goes to my advisors, Prof. Marco Moretti and Prof. Giacomo Ghiringhelli, and to all the doctoral students of the PoliMiX group. I would also like to underline the important work made by Matteo Corti and Andrea Cordone who accompanied me in this project giving an important contribution.